

UNIVERSITÀ DEGLI STUDI DI MILANO
Facoltà di Scienze Matematiche, Fisiche e Naturali
Corso di Laurea in Fisica

**Computation of electronic properties
of metallic surfaces:
total energy and quasiparticle
excitations**

RELATORE: Prof. Giovanni Onida
CORRELATORE: Dott. Nicola Manini
CORRELATORE: Dott. Luca Guido Molinari

Tesi di Laurea di
Marco Cazzaniga
Matr. 616385
Codice PACS
73.20.-r 71.10.Ca

ANNO ACCADEMICO 2004-2005

Contents

Introduction	v
Riassunto	vii
1 Theoretical methods	1
1.1 The jellium model	1
1.2 Std. approximations and the HEG	2
1.3 DFT and LDA	4
1.4 The GW approximation	6
1.5 The quasiparticles	7
2 The metal surface	11
2.1 Concepts in surface physics	11
2.1.1 Surface thermodynamics and energy	11
2.1.2 Density of charge at the surface	12
2.1.3 The image potential	12
2.2 The virial theorem and the surface energy of the jellium	14
2.3 The jellium surface	15
2.3.1 The Thomas-Fermi approach	16
2.3.2 The density-functional approach	17
2.3.3 The jellium slab in DFT	18
2.3.4 Other quantum size effects	20
3 Technical aspects of the calculations	23
3.1 Method of computation	23
3.1.1 Mapping the Brillouin zone: the k-points	24
3.1.2 The smearing	25
3.1.3 The ions: the pseudopotential approximation	25
3.1.4 The jellium background	26
3.2 The supercell	27
3.3 Convergence study	27

3.3.1	Study of the smearing functions	28
3.3.2	Convergence of k-points and smearing temperature . . .	28
3.3.3	Convergence against the cut-off energy	29
4	The infinite bulk jellium	31
4.1	Analytic computation	31
4.2	Numerical simulations	32
4.3	Comparison of components of the total energy	34
5	Computation of the surface energy	37
5.1	Simulation with ABINIT	37
5.1.1	Computation and results	37
5.1.2	Fits of the curves	39
5.1.3	The cusps	43
5.1.4	Analysis of the components of the total energy	44
5.2	The eigenfunctions	50
5.3	Study of the surface dipole	51
5.3.1	Interpolation of the dipole	51
5.3.2	Resulting energies	54
5.4	The "model density" method	57
5.4.1	The method	57
5.4.2	Results	60
6	LDA and GW band structure	65
6.1	Procedure in a GW computation	65
6.2	The Kohn-Sham band structure of the slab	68
6.3	The surface LDOS and the resonance states	70
6.4	The quasiparticle corrections	70
6.4.1	Procedure of computation	70
6.4.2	GW dispersion	72
6.4.3	Convergence with the vacuum thickness	76
	Appendix	79
A	Coulombian functional	79
	Conclusions	83
	Bibliography	85
	Ringraziamenti	89

Introduction

This thesis work is part of a research project whose aim is the study of the interaction of a metal surface with adsorbed atoms or molecules. This work focuses on the physics of the electrons of the metal, within the jellium model, a standard simplification where the ions are smeared to a uniform positive charged background. This model captures the physical properties intrinsic to the electron gas, characterized by a single parameter: the Wigner-Seitz radius. Despite its simplicity, when electron-electron interaction is properly accounted for, the jellium model describes correctly the Fermi-surface properties of simple metals and collective effects including plasmons, both in the bulk and in the surface. These collective effects are the origin of effects such as the image potential and the long-range van der Waals interaction with an adsorbate.

The general framework to attack the many-body problem is that of the density functional theory (DFT). It is at the basis of the most widely used methods to perform ab-initio computations of many electron systems. Unfortunately the local density approximation (LDA), which allows a simple implementation of the DFT, reveals itself inadequate in describing the long-range collective interactions. So different approaches have been attempted to improve the description of the metallic surfaces.

For this project we chose a different many-body theory, the GW approximation, which should not present the limitations described for the DFT-LDA, since it can describe the plasmons and the correct behaviour of the surface image potential.

To perform the calculations for this project, we chose the ABINIT package (www.abinit.org) which implements both the DFT and the computations of GW corrections. This code has been suitably modified by our research team to include the jellium background in a slab geometry.

In this thesis we test the functionality and limitations of the modified code and improve our knowledge on the behaviour of this system within the chosen approximations. We start from a test study of the jellium bulk (for which some results are known analytically), and then concentrate our

attention on the slab, in both LDA and GW.

By an analysis of the dependence of the total electronic energy as a function of both the slab thickness and the electron density, we obtain an estimate of the surface energy comparable to previous estimations. We also study the quantum size effects associated to the small separation of the two surfaces of the nanometrically sized slab. We analyzed the feature in terms of a simple phenomenological models. The total energy calculations have been performed only in DFT.

We used the GW to compute the corrections to the Kohn-Sham eigenvalues. In particular we study the convergence of the corrections with respect to the slab thickness and the behaviour of the quasiparticle energies close to the Fermi energy.

Conventions and units

In this thesis we adopt the atomic units, where the constants $\hbar = e = m_e = 4\pi\epsilon_0 = 1$. In this system the length unit is Bohr radius $a_B = 0.529 \text{ \AA}$, and the energy unit is the Hartree that correspond to twice the energy of the lowest state of the hydrogen atom ($1 \text{ Ha} = 27.21 \text{ eV}$).

Riassunto

Questo lavoro di tesi si colloca nell'ambito dello studio dell'interazione tra superfici metalliche (descritte tramite il modello a gellio) e adsorbati. Il lavoro è consistito nell'effettuazione di una serie di calcoli numerici e analitici onde studiare le proprietà del gellio senza adsorbati e testare le modifiche fatte al codice di calcolo che si è scelto di utilizzare, e vedere il comportamento del modello.

Si sono studiate le proprietà delle superfici metalliche attraverso il modello a gellio. Tale modello consiste in una semplificazione del metallo avendo trascurato la struttura del reticolo a cui è stata sostituita una distribuzione di carica positiva uniforme. Le aspettative sono di ottenere una miglior comprensione degli effetti dovuti all'interazione elettrone-elettrone e una ragionevole descrizione dei metalli più semplici, ossia quelli con gli elettroni di conduzione meno localizzati. Si è posta attenzione principalmente all'energia totale del sistema, alle sue componenti (contributi di bulk e di superficie) e alle eccitazioni di quasiparticella, nella geometria di bulk e in quella della lamina.

Il lavoro ha comportato l'uso dapprima della teoria del funzionale di densità nell'approssimazione di densità locale (DFT-LDA) per lo studio dello stato fondamentale del sistema. In seguito i risultati DFT-LDA sono stati utilizzati come punto di partenza per lo studio delle eccitazioni elementari nell'ambito dell'approssimazione GW in un approccio perturbativo al primo ordine. È stata utilizzata per la parte computazionale una versione del codice ABINIT [1] modificata appositamente per includere la densità di carica positiva del background.

Nei primo capitolo si sono studiate alcune proprietà generali del gas elettronico omogeneo soffermando l'attenzione anche sulle approssimazioni utilizzate in seguito per studiare tale sistema. Si è introdotto il sistema oggetto di studio, i risultati per il gellio omogeneo con alcune approssimazioni standard: elettroni indipendenti, Thomas-Fermi, Hartree-Fock e energia di correlazione. L'uso di approssimazioni si rende necessario dato che l'equazione di Schrödinger per un tale sistema non è risolvibile in modo diretto per via

dell'interazione tra gli elettroni. Si sono introdotti i due metodi che verranno usati in seguito per le simulazioni: la teoria del funzionale di densità con la quale si riesce a mappare il sistema in uno fittizio di particelle non interagenti, per cui si ottiene il seguente set di equazioni da risolvere:

$$\left[-\frac{\nabla^2}{2} + V_{ext}(\mathbf{x}) + V_H(\mathbf{x}) + V_{XC}(\mathbf{x}) \right] \phi_i = \epsilon_i \phi_i. \quad (1)$$

L'altra approssimazione utilizzata è l'approssimazione GW, basata sulla teoria a molti corpi, la quale consiste nel trascurare la funzione di vertice nel set delle equazioni di Hedin, portando al seguente sistema di equazioni per i vari correlatori:

$$G(1, 2) = G_0(1, 2) + \int G_0(1, 3) \Sigma(3, 4) G(4, 2) d^3d4$$

$$W(1, 2) = v(1, 2) + \int v(1, 3) \Pi(3, 4) W(4, 2) d^3d4$$

$$\Sigma(1, 2) = iG(1, 2)W(1, 2)$$

$$\Pi(1, 2) = -iG(1, 2)G(2, 1). \quad (2)$$

In conclusione si è analizzato il concetto di quasiparticella, presentato come polo della funzione di Green, o come soluzione di una particolare equazione ove nel termine di potenziale compare anche la self-energia:

$$\left[-\frac{1}{2}\nabla^2 + U_{Ext} + U_H \right] f_a(\mathbf{x}, \alpha) + \int d^3x' \Sigma(\mathbf{x}, \mathbf{x}', \omega_a) f_a(\mathbf{x}', \alpha) = \omega_a f_a(\mathbf{x}, \alpha). \quad (3)$$

Il passo successivo è consistito nello studio di alcune proprietà del gellio con superficie. Si è posta attenzione su una applicazione del teorema del viriale [38], che permette di legare le singole componenti dell'energia a quella totale. In seguito si sono analizzati i risultati trovati in letteratura riguardanti la superficie del gellio sia per la geometria semi-infinita che per la lamina, soffermandosi, in particolare, sulla energia di superficie e sulla densità di particelle. Si sono analizzati i risultati forniti dalle teorie di Thomas-Fermi, considerando anche le correzioni di gradiente al funzionale cinetico e gli effetti dovuti allo scambio e alla correlazione, DFT-LDA per un caso semi-infinito e per una lamina in DFT-LDA. Gli autostati del sistema non interagente studiato dalla DFT-LDA per il gellio con superficie (essendoci invarianza per le traslazioni nelle direzioni ortogonali alle stesse) possono essere scritti come il prodotto di due contributi di particella libera

(ossia onde piane) per le direzioni parallele alle superfici per un contributo più complesso nella terza direzione; di conseguenza gli autovettori saranno esprimibili come la somma di tre contributi di cui due addendi sono del tipo $\frac{k_{x,y}^2}{2}$. In corrispondenza della superficie la densità presenta un andamento esponenziale nel passaggio tra il valore nullo nel vuoto e il valore di bulk, al quale non converge immediatamente, ma a seguito di una serie di oscillazioni di Friedel smorzate da un denominatore che presenta un andamento quadratico nella distanza dalla superficie, cosicché la densità viene ad assumere un andamento di bulk solo parecchio all'interno della stessa. Nel caso della lamina (cfr. [35]) gli autovalori per la direzione ortogonale alle superfici (che, a differenza del caso semi-infinito, sono un set discreto) risultano essere decrescenti con lo spessore della lamina e presentano delle oscillazioni con delle cuspidi nei punti ove gli autovalori intersecano l'energia di Fermi. La densità

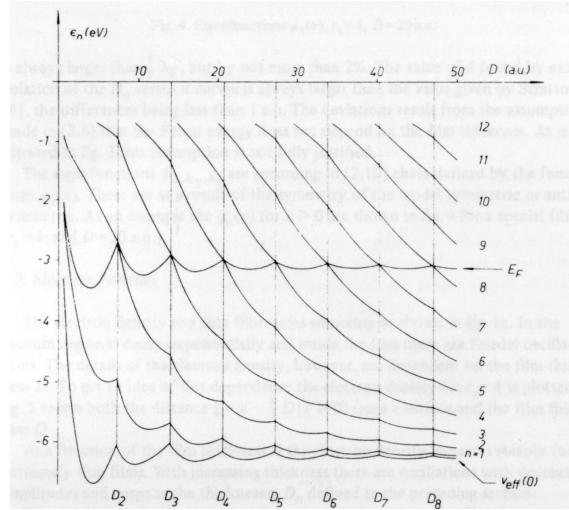


Figura 1: Andamento degli autovalori per in una lamina di gellio in funzione dello spessore della stessa.

di particelle che ne consegue risulta presentare delle oscillazioni nel dipolo di superficie e nel potenziale elettrostatico, oscillazioni legate al fatto che, a seguito di un minimo nel dipolo, un altro stato in direzione trasversa inizia a contribuire alla densità di carica producendo un maggior spill-out, effetto che diviene meno rilevante col maggior riempimento del suddetto stato. Infine si sono introdotte le peculiarità dovute alle dimensioni estremamente ridotte (cioè poche unità atomiche) della lamina, ossia gli effetti di scala quantistica (QSE); in particolare ci si è soffermati sul comportamento della funzione lavoro, che presenta delle oscillazioni indotte da quelle presenti nel

potenziale elettrostatico, dal momento che in seguito si otterranno analoghi comportamenti per l'energia totale e le sue componenti.

Prima di procedere con le simulazioni necessarie per questa tesi si è effettuata un'analisi delle approssimazioni necessarie per poter effettuare un computo numerico. Si parte dalle semplificazioni che il teorema di Bloch e la base di autofunzioni scelta per descrivere il sistema (ossia le onde piane) permettono, con la necessità di introdurre un'energia di taglio per poter avere una base costituita da un numero finito di elementi (il solo teorema di Bloch permette unicamente di passare da un vettore d'onda continuo ad uno discreto tramite le condizioni al contorno periodiche), in modo tale da riscrivere le autofunzioni di Kohn-Sham attraverso un set finito di coefficienti di Fourier. Quindi si è descritta la griglia discreta di punti \mathbf{k} necessaria per poter eseguire le integrazioni nella zona di Brillouin (nel nostro caso si è ricorso alla griglia di Monkhorst-Pack) e di conseguenza si è studiato il problema dello smearing utilizzato per regolarizzare le occupazioni che, a temperatura nulla presenterebbero una discontinuità all'energia di Fermi, introdotto per facilitare la convergenza rispetto al set finito di punti \mathbf{k} . Per ultimo si è analizzato il modo con cui viene descritta la carica positiva, introducendo il concetto di pseudopotenziali e il modo in cui si è implementata la densità uniforme del background tramite la codifica del potenziale risultante dall'equazione di Poisson per la distribuzione di carica del background uniforme.

Successivamente si è condotto uno studio di convergenza dell'energia totale rispetto ai parametri precedentemente descritti energia di taglio, numero di punti \mathbf{k} nella prima zona di Brillouin, funzione di smearing (per la quale si è scelta quella del cold smearing di Marzari) e temperatura di smearing, al fine di verificare che i risultati di energia totale non siano sostanzialmente influenzati dalla scelta di tali parametri. Ciò si rende necessario dal momento che si sono introdotte delle discretizzazioni per poter effettuare i computi numericamente, e occorre verificare che le suddette approssimazioni risultino adeguate per fornire valori di energie sufficientemente accurati.

Inizialmente le simulazioni si sono concentrate sul gellio uniforme di varia densità, dove i risultati computazionali si possono confrontare con quelli ottenuti analiticamente con la stessa teoria. Infatti per un caso omogeneo, non essendo la densità dipendente dalla posizione, le equazioni divengono risolubili analiticamente e l'energia per particella in DFT-LDA risulta essere data da:

$$\frac{E}{N} = \frac{3}{5}\epsilon_F + \epsilon_{XC} \quad (4)$$

ove ϵ_{XC} è noto una volta stabilita la parametrizzazione per lo scambio e la correlazione (per questa tesi si è scelta la parametrizzazione di Teter [15] per cui ϵ_{XC} è dato da una funzione razionale nel parametro r_s). Si riportano

i risultati per l'energia totale a confronto coi valori teorici (fig. 2). Da un'analisi delle singole componenti dell'energia risulta che, in questo caso semplice, soltanto il termine cinetico che è affetto dall'errore numerico indotto dalla discretizzazione dei punti \mathbf{k} presenta delle significative discordanze col termine analitico.

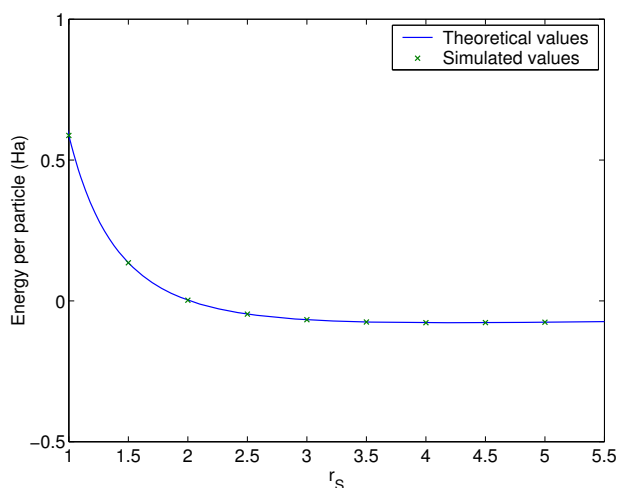


Figura 2: Confronto tra le energie di bulk calcolate analiticamente e quelle simulate.

Si è quindi passati allo studio della superficie del gellio, allo scopo di determinare l'energia di superficie γ , ricorrendo alla geometria a fetta o della lamina ripetuta periodicamente (cfr. fig. 3). Innanzitutto si è determinato

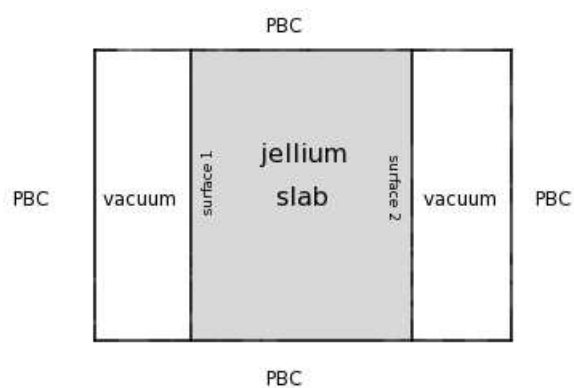


Figura 3: Rappresentazione grafica della geometria della lamina.

lo spessore di vuoto tra due lamine da reputarsi sufficiente affinché l'interazione tra di esse possa essere trascurata, verificando la convergenza dell'energia totale rispetto allo spessore di vuoto. Si è ricavato che uno spessore di separazione tra due lamine pari a $30 a_B$ sia sufficiente.

In seguito, per ogni valore del parametro r_s preso in esame, sono simulati diversi spessori D di lamina al fine di valutare gli effetti dovuti all'interazione tra le diverse superfici all'interno della stessa lamina e di calcolare l'energia di superficie. Si è ottenuto un andamento dell'energia per unità di area contenente un termine di bulk, uno di superficie ed uno di interazione tra le due superfici:

$$\frac{E}{A} = \epsilon_p \rho D + 2\gamma + E_{surf-surf}. \quad (5)$$

I valori per l'energia di superficie (o tensione superficiale) γ sono risultati in buon accordo con quelli calcolati da Lang e Kohn [24] (cfr. fig. 4). Si è anche determinato che le ampiezze e le fasi delle oscillazioni hanno un andamento decrescente con l'aumentare di r_s . Si è, inoltre, trovato per $E_{surf-surf}$ che esso

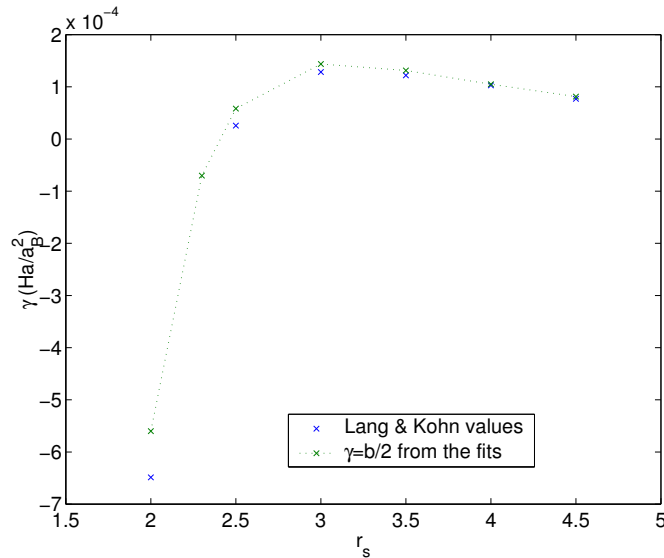


Figura 4: Energia di superficie in funzione della densità elettronica rappresentata dal parametro r_s .

viene correttamente fittato da una funzione oscillante con vettore d'onda pari a $2k_F$ smorzata da un fattore che decresce come D^{-2} . Pertanto la funzione utilizzata per il fit è:

$$\frac{E_{total}}{A} = \epsilon_p \rho D + b + c \frac{\cos(2k_F D + \theta)}{D^2} \quad (6)$$

Tale fit deve comunque essere inteso come un puro fit fenomenologico dal momento che la reale curva per le suddette oscillazioni dell'energia presenterebbero delle cuspidi che noi non troviamo nelle nostre simulazioni poiché la presenza dello smearing include un addolcimento delle stesse. Ciò è stato verificato con una simulazione ad una temperatura di smearing più bassa che ha permesso di constatare una tendenza a formare una cuspidi nel limite di temperatura nulla. Si riporta, a titolo di esempio, il grafico dei valori computati con la curva ottenuta dal fit per $r_s = 3.5$; i valori sono rappresentati a meno del termine di bulk che è stato sottratto per chiarezza rappresentativa. Un analogo comportamento è stato riscontrato nelle singole componenti del-

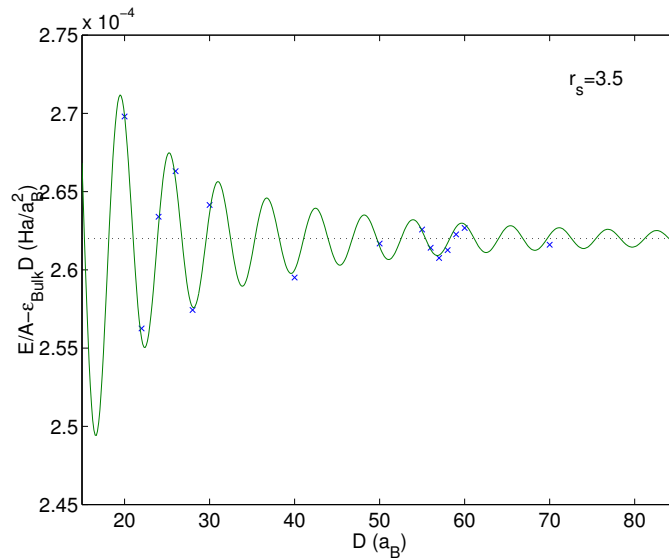


Figura 5: Confronto tra i valori di energie calcolati con ABINIT e la curva del miglior fit per $r_s = 3.5$. Ad entrambe le serie di dati sono stati sottratti i termini di bulk.

l'energia, anch'esse considerate per unità di area; sia il termine cinetico che quello coulombiano e di scambio e correlazione presentano delle oscillazioni analoghe a quelle dell'energia totale, che sono state fittate con la medesima funzione usata precedentemente, eq. (6), facendo sì che le oscillazioni complessive (a cui occorre aggiungere una correzione dovuta alla presenza dello smearing per ottenere l'energia totale) risultino essere una complessa sovrapposizione di varie funzioni oscillanti con diverse ampiezze e fasi (comp. fig. 6). Tale andamento è spiegato in base alle oscillazioni del dipolo di superficie in quanto variazioni della densità, che, di conseguenza, inducono delle oscillazioni nelle componenti dell'energia.

Per verificare se esse sono la causa principale di quanto osservato si è fatto

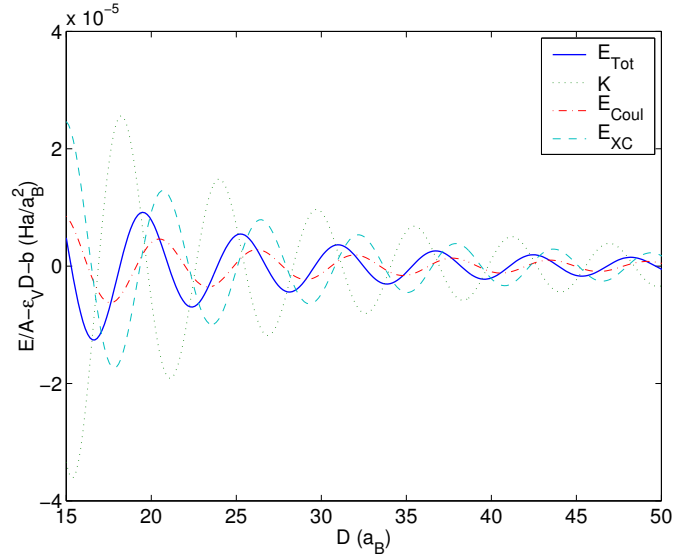


Figura 6: Confronto tra le curve ottenute dai fits per le varie componenti dell'energia e l'energia totale, a tutte le curve sono state sottratte le rispettive componenti di bulk (indicate con ϵ_V) e i contributi di superficie.

ricorso ad un semplice modello che considera solo la presenza del dipolo di superficie trascurando le oscillazioni di Friedel al suo interno. Dal momento che la densità presenta un andamento esponenziale, si è presa una tale funzione e si sono fittate le densità fornite dall'ABINIT per determinare i parametri mancanti. La densità scelta è:

$$n(z) = \begin{cases} \frac{\rho}{2} e^{\beta z} & z \leq 0 \\ \rho - \frac{\rho}{2} e^{-\beta z} & 0 < z \leq \frac{D}{2} \\ \rho - \frac{\rho}{2} e^{\beta(z-D)} & \frac{D}{2} < z \leq D \\ \frac{\rho}{2} e^{-\beta(z-D)} & z > D \end{cases} \quad (7)$$

Da tali densità modellizzate si sono calcolate le componenti dell'energia totale per unità di area. La scelta del funzionale di scambio e correlazione è stata la stessa utilizzata per le simulazioni numeriche. Per il termine cinetico si è fatto ricorso al funzionale di Thomas-Fermi con le correzioni di gradiente, in quanto quello della DFT è dipendente dalla densità tramite le funzioni d'onda del sistema non interagente che nel modello non sono note. Il funzionale di interazione Coulombiana è stato semplificato attraverso la risoluzione dalla dipendenza dalle variabili planari, calcolata analiticamente, deducendo che esso può essere scritto come:

$$E_{Coul} = -\pi \int_{-\infty}^{\infty} dz \int_{-\infty}^{\infty} dz' n(z)n(z')|z - z'| - \pi\rho^2 \frac{D^3}{3} +$$

$$+2\pi\rho \left[\int_D^\infty dz' n(z') (2z'D - D^2) \int_0^D dz' n(z') \frac{z'^2}{2} \right] \quad (8)$$

Già il parametro β della funzione interpolante la densità presenta delle oscillazioni (anch'esse fittate in base a una funzione con andamento del tipo $b + c \frac{\cos(2k_F D + \theta)}{D^2}$), segno che la lunghezza, lungo cui avviene la decrescita della densità tra il valore di bulk e quello nullo, risulta dipendente dallo spessore della lamina. In aggiunta si è ottenuto, dal confronto tra due valori di r_s , che le ampiezze delle oscillazioni di tale parametro sono compatibili con la decrescita dell'ampiezza delle oscillazioni nell'energia totale. Questo semplice modello produce una descrizione ragionevole per le ampiezze e le fasi delle oscillazioni delle singole componenti dell'energia totale, mentre, come ci si aspettava, data l'estrema semplificazione, non fornisce risultati accurati per i termini di superficie. A titolo di esempio si riporta il grafico ottenuto per il termine di scambio e correlazione (cfr. fig. 7), ove anche qui i valori sono rappresentati a meno del termine di bulk. Meno soddisfacente risulta essere

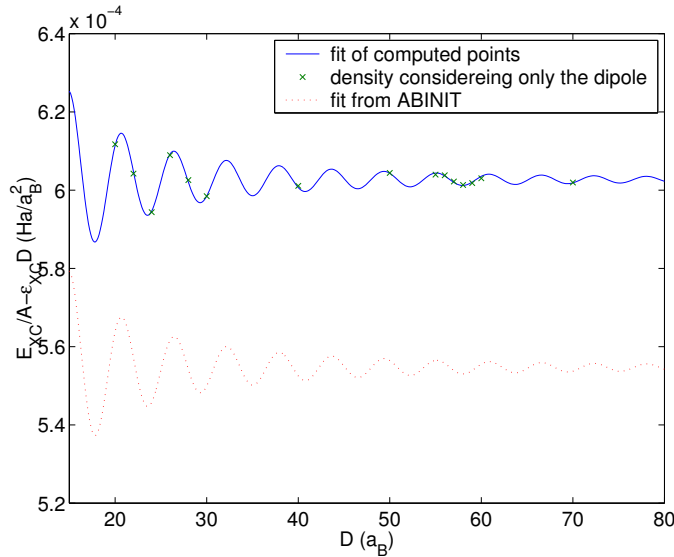


Figura 7: Confronto tra le energie di scambio e correlazione calcolate con ABINIT e il modello con solo il dipolo di superficie. In figura vi sono i punti calcolati con quest'ultimo modello, il relativo fit e il fit ottenuto dai valori di ABINIT.

la somma dei tre contributi in quanto oltre a un termine di superficie, per cui non ci si attende un buon accordo, anche le ampiezze e le fasi delle oscillazioni risultano in peggior accordo con quelle ottenute dalla DFT rispetto a

quelle nelle singole componenti, poiché l'energia totale risulta essere data da una complessa cancellazione dei singoli termini.

Inoltre si è verificato che all'interno della lamina effetti di interferenza delle oscillazioni di Friedel provenienti dalle due superfici contribuiscono alle oscillazioni dell'energia totale per non più del 10% dell'ampiezza. Ciò è stato possibile grazie ad un altro semplice modello: si è descritta la densità come derivante da una somma di quattro contributi dati uno dal bulk, due dalle singole superfici considerate come la correzione rispetto al bulk per un caso semi-infinito e una restante correzione:

$$n(z) = \frac{3}{4\pi r_s^3} \theta(z) \theta(D - z) + \chi(z) + \chi(D - z) + \Delta\rho(z), \quad (9)$$

ove $\chi(z)$ è il contributo alla densità dato da una singola superficie. Questo è stato ottenuto tramite il calcolo di una lamina particolarmente spessa ($210 a_B$) tale da poter ritenere che i primi $45 a_B$ non siano influenzati dalla presenza dell'altra superficie. Per ottenere la funzione $\chi(z)$ alla densità così calcolata si è sottratto, per coordinate interne alla lamina, il valore della densità di bulk $\rho = \frac{3}{4\pi r_s^3}$. L'ultimo addendo dell'equazione (9) è stato trascurato, ritenendo che tale sia piccolo rispetto agli altri contributi, costruendo così una densità modello con cui verificare se gli effetti dovuti alla non linearità dei funzionali possano influire sulle oscillazioni delle componenti dell'energia. Si è dovuto tenere in considerazione la necessità di smorzare le densità provenienti dalle due superfici per non lasciarle oscillare oltre l'altra superficie; ciò è stato fatto moltiplicando la densità della singola superficie per una funzione simile a quella di Fermi. Con una densità siffatta, data dall'eq. (9), si sono calcolati i valori delle componenti dell'energia per unità di area, con gli stessi funzionali usati per il modello descritto precedentemente, in funzione dei parametri di smorzamento. Ne è risultato, come già accennato, una descrizione ragionevole per i termini di superficie (pur coi limiti di una scelta differente dei funzionali), mentre si sono ricavate delle oscillazioni di ampiezza molto minore, e un disaccordo per quanto riguarda le fasi.

Il passo successivo è stato lo studio delle eccitazioni di quasiparticella nella geometria di supercella. Tali calcoli sono stati compiuti tramite il computo delle correzioni GW in modo perturbativo a partire dagli stati di Kohn-Sham. L'equazione di quasiparticella è infatti formalmente simile alle equazioni di Kohn-Sham e perciò diviene possibile effettuare il calcolo della correzione agli autostati della DFT-LDA tramite la teoria perturbativa al primo ordine in $\Sigma - V_{XC}$. Ne segue che occorre calcolare:

$$E_i - \epsilon_i = \frac{\langle \Sigma(\epsilon_i) \rangle - \langle V_{XC} \rangle}{1 - \left\langle \frac{\partial \Sigma(\omega)}{\partial \omega} \Big|_{\omega=\epsilon_i} \right\rangle} = Z_i (\langle \Sigma(\epsilon_i) \rangle - \langle V_{XC} \rangle), \quad (10)$$

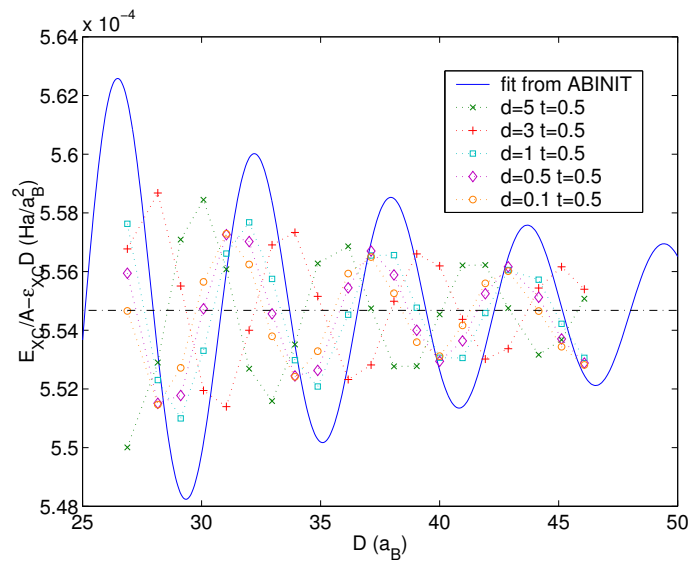


Figura 8: Confronto tra le energie di scambio e correlazione calcolate con ABINIT e il modello con la densità precedentemente descritta. In figura vi sono i punti calcolati con quest'ultimo modello in funzione dei parametri d posizione dello smorzamento dal bordo opposto della lamina e t la sua ampiezza con il fit ottenuto dai valori di ABINIT.

dove i valori di aspettazione sono da calcolarsi sugli autostati di Kohn-Sham. Inoltre per questi calcoli si è fatto ricorso alla approssimazione di polo plasmonico (PPA), la quale permette di semplificare la dipendenza della matrice dielettrica dalla frequenza riscrivendola come segue:

$$\tilde{\epsilon}_{\mathbf{G},\mathbf{G}'}^{-1}(\mathbf{q},\omega) = \delta_{\mathbf{G},\mathbf{G}'} + \frac{\Omega_{\mathbf{G},\mathbf{G}'}^2(\mathbf{q})}{\omega^2 - \tilde{\omega}_{\mathbf{G},\mathbf{G}'}^2(\mathbf{q})} \quad (11)$$

Prima di procedere si sono analizzati e interpretati i risultati ottenuti tramite la DFT-LDA (cfr. fig. 9) facendo riferimento ad un'interpretazione impropria degli autovalori di Kohn-Sham a partire dalla somiglianza tra le equazioni della DFT e quelle di quasiparticella. Si nota come la dispersione per vettori

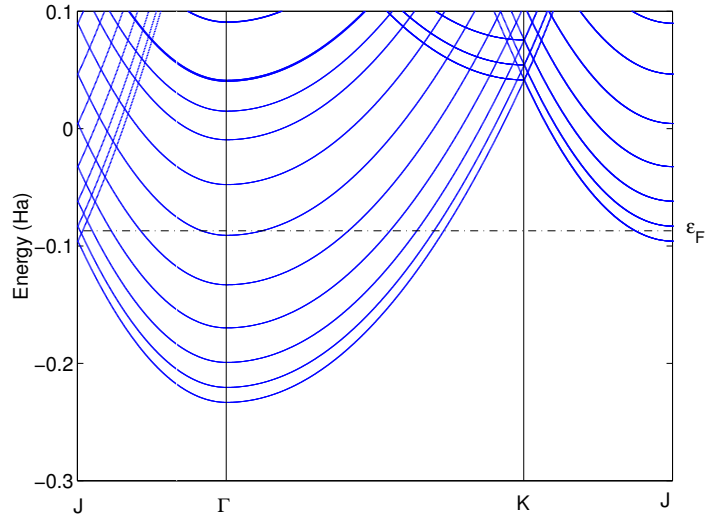


Figura 9: Curve di dispersione in DFT-LDA per una lamina con $r_s = 3.5$ e spessore $30 a_B$. Le curve sono da intendersi in funzione del vettore d'onda parallelo alla superficie, nella zona di Brillouin determinata dalla cella utilizzata per la simulazione.

d'onda paralleli alla superficie risultano essenzialmente paraboliche, mentre si osservano una successione di parabole date dalla discretizzazione delle energie nella terza direzione; si osservano anche gli attesi ripiegamenti delle curve a bordo zona.

Si è anche posta attenzione su una caratteristica delle superfici metalliche che la DFT-LDA non è in grado di descrivere correttamente, legata alla errata descrizione del potenziale a grande distanza dalla superficie. Poiché la DFT-LDA prevede un andamento esponenziale in corrispondenza della stessa, perde tutte le peculiarità dovute al potenziale immagine che avrebbe

un andamento dato da una potenza. Tale potenziale includerebbe in se degli stati localizzati in superficie analoghi a quelli dell'atomo di idrogeno, che in assenza di un gap in quelle regione di energie si mescola con gli stati di bulk dando luogo a delle risonanze, che la DFT-LDA non riesce a descrivere, ma che vengono recuperate attraverso l'uso dell'approssimazione GW.

Sono quindi state calcolate le correzioni agli autovalori di Kohn-Sham tramite la approssimazione GW studiandone la convergenza rispetto allo spessore di vuoto. Sono stati simulati spessori da $20 a_B$ a $50 a_B$ con intervalli di $10 a_B$. Si riportano i valori delle eccitazioni di quasiparticella per lo spessore di $30 a_B$ (fig. 10); gli altri hanno un andamento qualitativamente simile. Le correzioni sono risultate tutte positive con l'eccezione di pochi punti per

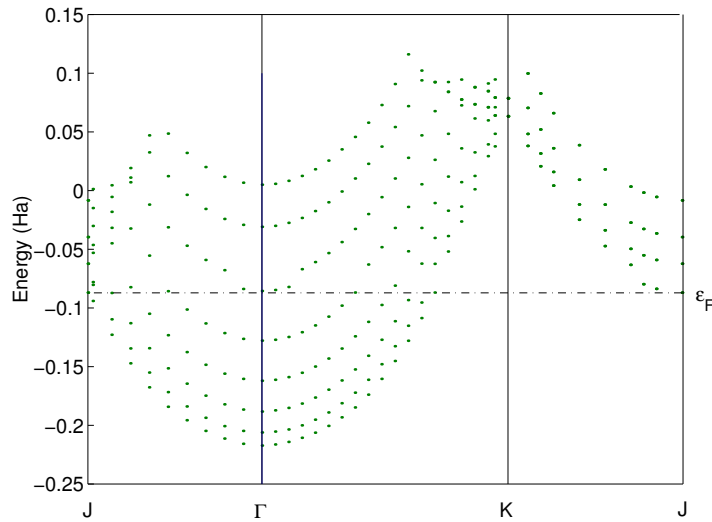


Figura 10: Correzioni GW per le energie di quasiparticella per una lamina di $30 a_B$ con $30 a_B$ di vuoto, $r_s = 3.5$ e parametro reticolare in direzione ortogonale alle superfici pari a $5.99 a_B$. L'energia di Fermi non è stata ricalcolata ed è quindi da considerarsi solo una stima.

gli stati ad energia più alta. Si nota in tali curve un andamento pressochè parabolico rinormalizzato dalle correzioni GW, mentre le differenze maggiori si osservano in prossimità dell'energia di Fermi, dove si nota un salto nei valori delle energie di quasiparticella. Riguardo alle singole componenti delle correzioni si ha che i termini di scambio della self-energia è negativo e presenta il già citato salto per $k = k_F$, analogamente, come atteso, è negativa anche la sua derivata rispetto alla frequenza. Il contributo di correlazione non presenta segno definito, ma anch'esso presenta il salto nel passaggio da stati pieni a stati vuoti. La correzione totale viene ad essere positiva grazie al contributo del valor medio del potenziale di scambio e correlazione.

Rispetto all'energia di vuoto si osserva, in un intorno di Γ quanto riportato in fig. 11, ove si sono rappresentati i valori delle eccitazioni GW alle quali si sono sottratti gli autovalori di Kohn-Sham. Si può constatare che

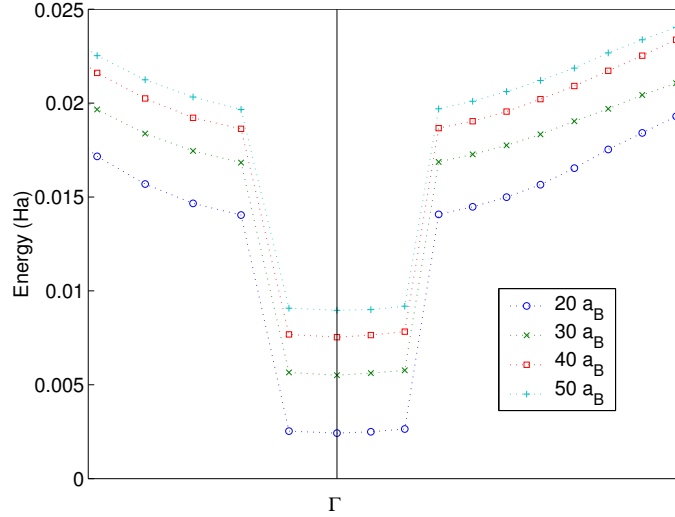


Figura 11: Convergenza delle correzioni GW rispetto allo spessore di vuoto, $r_s = 3.5$ e spessore della lamina di $30 a_B$. Il grafico rappresenta la sesta banda che è parzialmente occupata (il gradino nelle curve corrisponde al punto ove si passa da stati pieni a stati vuoti).

le correzioni presentano anch'esse, per tutti gli spessori, il salto nel passaggio da stati pieni a stati vuoti. Il loro andamento in funzione dello spessore è spiegabile a partire dall'aumento di vuoto che causa una decrescita nella costante dielettrica portando ad un incremento degli elementi di matrice delle correzioni.

Chapter 1

Theoretical methods

This work addresses the physics of metal surfaces. Many properties of surfaces depend on the detailed lattice structure of the solid. Other properties are "universal", in the sense that they only depend on the electron density. This thesis address precisely this physics in the jellium model. In this chapter we will present different approximations which have been used to describe a many-body system and their application to the homogeneous electron gas.

1.1 The jellium model

The model we are going to use for describing a metal, the jellium, consists in a gas of electrons in a background of uniform positive charge. Using this approximation to describe an infinite system, the electron density is a constant, often described through the dimensionless parameter r_s (the Wigner-Seitz radius). It is related to background density (which in the homogeneous case is equal to the electron one) $\rho = \frac{N}{V}$ through the relation:

$$\frac{1}{\rho} = \frac{4\pi(r_s a_B)^3}{3} \quad (1.1)$$

where a_B is the Bohr radius that we take equal to one since we work in atomic units. For metals, considering only the conduction electron, r_s ranges between 2 and 4 in most cases, even if it becomes as large as 6 for the alkalis. We report its value for some metals [3]:

element	Li	Na	K	Cu	Al
r_s	3.25	3.93	4.86	2.67	2.07

The jellium model is a simplification of a real metal since, for example, the presence of the lattice is replaced by a uniform background and the core electrons are neglected. Even if it is not possible to describe all metal properties

with this simple model, it is useful since it gives at least some qualitative informations about the effects due to the electron-electron interactions. Indeed one expects that this model gives a rather good agreement with the physical properties of the metals whose conduction electrons are weakly bounded, i. e. the alkali and many metals with only s and p conduction electrons, since these are the less localized.

The non relativistic Hamiltonian of the jellium system of N electrons is:

$$H = \sum_{i=1}^N \frac{\mathbf{p}_i^2}{2} + \sum_{i<j} \frac{1}{|\mathbf{x}_i - \mathbf{x}_j|} - \sum_{i=1}^N \int d^3x \frac{n_+(\mathbf{x})}{|\mathbf{x} - \mathbf{x}_j|} + \frac{1}{2} \int d^3x d^3y \frac{n_+(\mathbf{x})n_+(\mathbf{y})}{|\mathbf{x} - \mathbf{y}|} \quad (1.2)$$

where \mathbf{x} is the electron position, \mathbf{p} its conjugate momentum, and $\rho(\mathbf{x})$ is the background density. The first term is the kinetic energy, the second term the repulsion between the electrons, the third one the attraction between electrons and the positive background, and the last term is the interaction of the positive background with itself.

1.2 Standard approximations and their application to the infinite electron gas

If the jellium background is uniformly distributed through the whole space, the Hamiltonian simplifies to:

$$H = \sum_{i=1}^N \frac{\mathbf{p}_i^2}{2} + \sum_{i<j} \frac{1}{|\mathbf{x}_i - \mathbf{x}_j|} - \sum_{i=1}^N \rho \int d^3x \frac{1}{|\mathbf{x} - \mathbf{x}_j|} + \frac{1}{2} \rho^2 \int d^3x d^3y \frac{1}{|\mathbf{x} - \mathbf{y}|}. \quad (1.3)$$

Each of these terms diverges in the thermodynamic limit $V \rightarrow \infty$. The kinetic energy per unit volume is finite. Instead each of the Coulombic terms is infinite even if it is taken per unit volume. However the sum of these three Coulombic terms yields a finite contribution per unit volume. The interacting Schrödinger equation cannot be solved exactly and several approximations have been developed to investigate the effects of interaction.

If the electron electron repulsion is neglected, the many-electron wavefunction consists in a Slater determinant of plane waves, of kinetic energy per particle $\frac{3}{5}\epsilon_F$, where ϵ_F is the maximum kinetic energy of the single particle states ($\epsilon_F = \frac{1}{2}(3\pi^2\rho)^{2/3}$).

A simple method to study this system is the Thomas-Fermi approximation. With this approach the energy of the system is written as a functional of the density. In particular the choice done for the kinetic term is to use the

expression of the energy for an homogeneous electron gas and to make it as a local functional of the density:

$$K[n(\mathbf{x})] = \frac{3}{10}(3\pi^2)^{2/3} \int [n(\mathbf{x})]^{5/3} d^3x. \quad (1.4)$$

To this is added the electrostatic interaction through the electrostatic potential obtained by the Poisson equation with the charge distribution of the system. For a uniform infinite electron gas, the three Coulombic term cancel exactly, yielding a total null contribution to the total energy. Therefore the total energy of the uniform system in the Thomas-Fermi approximation is:

$$\frac{E^{(TF)}}{N} = \frac{3}{5}\epsilon_F = \frac{3}{10} \left(\frac{9\pi}{4} \right)^{2/3} \frac{1}{r_s^2}. \quad (1.5)$$

A better approach to this many-body problem is the Hartree-Fock approximation. Like in the Thomas-Fermi approximation one finds that the sum of the Hartree energy plus the energies due to the interactions between background-background and background-electrons cancel exactly in the uniform gas. Therefore only the kinetic and exchange terms contribute to the total energy [3], [12]. An analytic expression is available for the exchange term, so that the energy per particle is a function of the parameter r_s :

$$\frac{E^{(HF)}}{N} = \left[\frac{3}{10} \left(\frac{9\pi}{4} \right)^{2/3} \frac{1}{r_s^2} - \left(\frac{9\pi}{4} \right)^{1/3} \frac{3}{4\pi} \frac{1}{r_s} \right]. \quad (1.6)$$

The Hartree-Fock approximation is equivalent to a first order perturbation theory over a free electron system. Further terms, globally called correlation energy, are neglected. Since the Hartree-Fock approximation may be seen as a variational theory over the states that may be written as Slater determinant of single particles wavefunctions, and because the true ground state may not be one of these, the neglected correlation energy is necessarily negative. A possible approach to compute the correlation energy is based on a series expansion over the parameter r_s ; this method gives a good result in the limit of dense electron gas (small r_s). The first terms of this series are computed in the RPA (random phase approximation) for which the contribution to the polarization is due to the most divergent diagrams at each perturbation order. In this case one gets that the correlation energy expressed in atomic units is:

$$\frac{E_C(r_s)}{N} = \frac{1}{2}[0.0622 \log(r_s) - 0.0938]. \quad (1.7)$$

By summing other series of less divergent diagrams, the correlation energy has been computed to order r_s [10] getting the following expression:

$$\frac{E_C(r_s)}{N} = \frac{1}{2}[0.0622 \log(r_s) - 0.0938 + 0.0814r_s \log(r_s) - 0.02r_s]. \quad (1.8)$$

Another approximation to study this system is the DFT introduced in the following section and whose results will be analyzed in sec. 4.1.

1.3 DFT and LDA

The Density Functional Theory (DFT) [9] is based on the Hohenberg and Kohn theorem that sets the existence of a biunivocal correspondence between the density of the system and the external potential that generates it [19]. A consequence of this theorem is the formulation of a variational principle. According to this, given $v_{ext}(\mathbf{x})$, and considering the functional

$$E^{(HK)}[n(\mathbf{x}); v_{ext}(\mathbf{x})] = \langle \psi_G[n(\mathbf{x})] | T + V_{ee} + V_{ext} | \psi_G[n(\mathbf{x})] \rangle, \quad (1.9)$$

$E^{(HK)}$ assumes the minimum value when $\psi_G[n(\mathbf{x})]$ is the ground state which is necessarily also a functional of its density. Moreover it is possible to rewrite the functional of the energy in the form:

$$E^{(HK)}[n(\mathbf{x}); v_{ext}(\mathbf{x})] = T[n(\mathbf{x})] + V_{ee} + \int v_{ext}(\mathbf{x})n(\mathbf{x})d^3x, \quad (1.10)$$

where T is the kinetic term, V_{ee} the electron-electron interaction, and the last term is the contribution of the external potential. The peculiarity of this functional is that the first two terms are universal, i. e. not depending of the choice of the system, even if they are not known.

This theorem makes possible to introduce an auxiliary system of non interacting electrons [23] with the same density of the real system so that the wave function of this system is the Slater determinant of the one particle wave functions and the density is the sum of their square moduli. For the Hohenberg and Kohn theorem this is possible because there exists an external potential for the non interacting case that produces the same density. The energy functional may be rewritten as:

$$E^{(HK)}[n(\mathbf{x}); v_{ext}(\mathbf{x})] = T_0[n(\mathbf{x})] + E_H + E_{XC}[n(\mathbf{x})] + \int v_{ext}(\mathbf{x})n(\mathbf{x})d^3x, \quad (1.11)$$

where E_{XC} contains the differences between the kinetic term of non interacting particles and the real one, and between the Hartree energy and the

actual electron-electron interaction. By applying the variational procedure to this functional one deduces the following Kohn-Sham set of equations

$$\left[-\frac{\nabla^2}{2} + V_{ext}(\mathbf{x}) + V_H(\mathbf{x}) + V_{XC}(\mathbf{x}) \right] \phi_i = \epsilon_i \phi_i, \quad (1.12)$$

where $V_H(\mathbf{x}) = \int \frac{n(\mathbf{x}')}{|\mathbf{x}-\mathbf{x}'|} d^3x'$, $V_{XC}(\mathbf{x}) = \frac{\partial E_{XC}}{\partial n(\mathbf{x})}$, and ϕ_i are the wave functions for the non interacting system and V_{XC} is the functional derivative of E_{XC} with respect to $n(\mathbf{x})$.

Once this set of equations is solved, it is possible to compute the total energy:

$$E_0 = \sum_i \epsilon_i - \frac{1}{2} \sum_{i,j} \left\langle \phi_i \phi_j \left| \frac{1}{|\mathbf{x}_i - \mathbf{x}_j|} \right| \phi_i \phi_j \right\rangle + E_{XC}[n(\mathbf{x})] - \int V_{XC}(\mathbf{x}) n(\mathbf{x}) d^3x. \quad (1.13)$$

The still unsolved problem is the knowledge of the functional E_{XC} . To use this theory, which at this point is exact, one needs to make an approximation in order to get an expression for this functional. The approximation used for the present computation is the local density approximation (LDA). In the LDA, like one does in Thomas Fermi for the kinetic term, the E_{XC} chosen is taken locally equal the one of an homogeneous electron gas with the same density:

$$E_{XC}^{(LDA)}[n(\mathbf{x})] = \int \epsilon_{XC}[n(\mathbf{x})] n(\mathbf{x}) d^3x. \quad (1.14)$$

Here, $\epsilon_{XC}[n(\mathbf{x})]$ is the many-body exchange and correlation per particle of a uniform electron gas. This approximation is particularly justified if in the system the density varies slowly.

To determine ϵ_{XC} it is necessary to solve accurately the full interacting uniform electron gas problem, and this is far from trivial: in practice the starting point for its evaluation usually are the simulations made by Ceperley and Adler with Monte Carlo methods [7]. From these computations different parameterizations of ϵ_{XC} have been proposed like the one given by Perdew and Zunger [31]. For the present work we choose instead the Teter Padé parameterization [15]. In this case the following expression for ϵ_{XC} for an unpolarized electron gas is assumed:

$$\epsilon_{XC}(r_s) = -\frac{0.458165293 + 2.217058677r_s + 0.740555173r_s^2 + 0.019682279r_s^3}{r_s + 4.504130959r_s^2 + 1.110667364r_s^3 + 0.023592917r_s^4}. \quad (1.15)$$

1.4 The GW approximation

A different kind of approximation, which may be used to improve Thomas-Fermi or DFT results, is the GW one [17], [18]. The starting point for this approximation is the many-body theory, in particular the Dyson equations for the Green function and the effective interaction:

$$G(1, 2) = G_0(1, 2) + \int G_0(1, 3)\Sigma(3, 4)G(4, 2)d3d4 \quad (1.16)$$

$$W(1, 2) = v(1, 2) + \int v(1, 3)\Pi(3, 4)W(4, 2)d3d4. \quad (1.17)$$

Here the notation 1 stands for the set of variables $(\mathbf{x}_1, t_1, \alpha_1)$ representing the position, time and spin of particle 1, while the integration stand for an integration in the space and time variables and for a spin summation. $G_0(1, 2)$ is the Green function for free fermions and $v(1, 2)$ is the Coulombian interaction $\frac{1}{|\mathbf{x}_1 - \mathbf{x}_2|}\delta(t_1 - t_2)$. These equations are completed by other equations describing the self energy (Σ) and the polarization (Π) which depend from the Green function, the effective interaction and another correlator called the vertex function (Γ), because in the Feynman diagrammatic representation of these equations it corresponds to a vertex that has in entrance and in exit a fermion line and an interaction one. These extra equations are:

$$\Sigma(1, 2) = i \int G(1, 3)W(4, 1)\Gamma(3, 2; 4)d3d4 \quad (1.18)$$

$$\Pi(1, 2) = -i \int G(1, 3)G(4, 1)\Gamma(3, 4; 2)d3d4. \quad (1.19)$$

To get a closed system of equations a fifth equation has been deduced for the vertex function, namely:

$$\Gamma(1, 2; 3) = \delta(1, 2)\delta(1, 3) + \int \frac{\delta\Sigma(1, 2)}{\delta G(4, 5)}G(4, 6)G(7, 5)\Gamma(6, 7; 3)d4d5d6d7 \quad (1.20)$$

The set of five equation (1.16, 1.17, 1.18, 1.19, 1.20) were first written by Hedin [17] and are exact.

The GW approximation consists in neglecting the corrections to the vertex function, so that the fifth equation becomes:

$$\Gamma(1, 2; 3) = \Gamma_0(1, 2; 3) = \delta(1, 2)\delta(1, 3) \quad (1.21)$$

From this assumption the system of Hedin equations reduces to a system of four integral equations called the GW approximation (from a short notation of the equation for the self energy):

$$\begin{aligned}
G(1, 2) &= G_0(1, 2) + \int G_0(1, 3)\Sigma(3, 4)G(4, 2)d3d4 \\
W(1, 2) &= v(1, 2) + \int v(1, 3)\Pi(3, 4)W(4, 2)d3d4 \\
\Sigma(1, 2) &= iG(1, 2)W(1, 2) \\
\Pi(1, 2) &= -iG(1, 2)G(2, 1)
\end{aligned} \tag{1.22}$$

Thanks to this approximation is possible to correct some of the errors induced by a DFT computation, like the underestimation of the gap of the semiconductors [14]. In this work the authors computed the quasiparticle energies for different semiconductors and found a rigid vertical displacement of the valence bands with respect to the conduction once. This increases the gap to values comparable with the experimental results. Even metallic systems have been studied [25]: quasiparticles properties are found in better agreement with the experimental results than the DFT-LDA bands.

1.5 The quasiparticles

In a solid it is possible to describe the strongly interacting electrons through the usage of weakly interacting quasiparticles [18]. Because of the Coulombic repulsion between electrons, each of them results surrounded by a positively charged polarization cloud. The electron with its positive screening cloud takes the name of quasiparticle. Since these are not eigenvalues of the Hamiltonian of the system, they will have a finite lifetime.

In order to give a mathematical description of the quasiparticles we start from the Lehmann representation of the Green function:

$$\begin{aligned}
G_{\alpha,\beta}(\mathbf{x}, \mathbf{x}', \omega) &= \sum_{E_n^{N+1}} \frac{\langle E_0^N | \Psi_\alpha(\mathbf{x}) | E_n^{N+1} \rangle \langle E_n^{N+1} | \Psi_\beta^+(\mathbf{x}') | E_0^N \rangle}{\omega - (\epsilon_n^{N+1} + \mu) + i\eta} + \\
&+ \sum_{E_n^{N-1}} \frac{\langle E_0^N | \Psi_\beta^+(\mathbf{x}') | E_n^{N-1} \rangle \langle E_n^{N-1} | \Psi_\alpha(\mathbf{x}) | E_0^N \rangle}{\omega + (\epsilon_n^{N-1} - \mu) - i\eta}.
\end{aligned} \tag{1.23}$$

In this notation E_0^N is the ground state of N particles and E_n^{N+1} and E_n^{N-1} are generic state of the system with $N + 1$ and $N - 1$ particles.

A consequence of this writing of the Green function is the possibility, for a system with translational invariance, to transcribe the Green function through the introduction of the spectral function:

$$G(\mathbf{k}, \omega) = \int_{-\infty}^{\infty} d\omega' \frac{A(\mathbf{k}, \omega')}{\omega - \omega' - \mu + i\eta \text{sign}(\omega')} \quad (1.24)$$

The spectral function is related to the imaginary part of the Green function through the relation:

$$A(\mathbf{k}, \omega) = \frac{1}{\pi} |\Im G(\mathbf{k}, \omega)| \quad (1.25)$$

This function is, by definition, real, positive and has to fulfill the sum rule for which its integral from $-\infty$ to ∞ must be 1. For free fermions it results to be $A_0(\mathbf{k}, \omega) = \delta\left(\omega - \frac{\mathbf{k}^2}{2} + \mu\right)$.

In order to consider a case similar to the free fermions, but slightly more general, we take a peaked spectral function, like a Lorentzian, instead of the Dirac delta, so that it becomes:

$$A(\mathbf{k}, \omega) = \frac{1}{\pi\tau} \frac{1}{(\omega - \epsilon_{\mathbf{k}} + \mu)^2 + \frac{1}{\tau^2}} \quad (1.26)$$

where $\epsilon_{\mathbf{k}}$ is the dispersion relation. With this spectral function we get a Green function similar to the free fermion one, so that it may be interpreted as the one of something like a particle which has an half life equal to τ . These are the quasiparticles.

The following step is to consider the Green function of a generic interacting system, case in which we find again the quasiparticles in correspondence of its poles. Since it is the solution of the Dyson equation (1.16), it can be written as:

$$G(\mathbf{k}, \omega) = \frac{1}{\omega - \frac{\mathbf{k}^2}{2} - \Sigma(\mathbf{k}, \omega)}. \quad (1.27)$$

The Green function presents poles in the complex ω -plane with positive imaginary part for $\omega < \mu$ and negative in the other case. This happens when the denominator is zero (in a point that will be called $\epsilon_{\mathbf{k}} + i\gamma(\mathbf{k})$) so that we deduce the following conditions for the real and the small imaginary part.

$$\begin{aligned} \mu + \epsilon_{\mathbf{k}} - \frac{\mathbf{k}^2}{2} - \Re \Sigma(\mathbf{k}, \mu + \epsilon_{\mathbf{k}}) &= 0 \\ \gamma(\mathbf{k}) &= \frac{\Im \Sigma(\mathbf{k}, \mu + \epsilon_{\mathbf{k}})}{1 - \frac{\partial}{\partial \omega} \Re \Sigma(\mathbf{k}, \omega) |_{\omega=(\mu+\epsilon_{\mathbf{k}})}} \end{aligned} \quad (1.28)$$

If we expand this function near the pole, with the condition that the imaginary part is small, so that the peaked structure is the most important part, it can be written as a peaked function plus a regular term ($G_1(\mathbf{k}, \omega)$):

$$G(\mathbf{k}, \omega) = \frac{Z(\mathbf{k})}{\omega - (\mu + \epsilon_{\mathbf{k}} + i\gamma(\mathbf{k}))} + G_1(\mathbf{k}, \omega) \quad (1.29)$$

One can notice that the Green function has an aspect similar to the previous case, since we deduce a spectral function that is:

$$A(\mathbf{k}, \omega) = \frac{1}{\pi} \left| \frac{Z_1\gamma(\mathbf{k}) + Z_2(\omega - \epsilon_{\mathbf{k}} + \mu)}{(\omega - \epsilon_{\mathbf{k}} + \mu)^2 + \gamma(\mathbf{k})^2} + \Im G_1(\mathbf{k}, \omega) \right| \quad (1.30)$$

where Z_1 and Z_2 are two constant necessary to respect the sum rule. This spectral function is a peaked function, that is similar to a Lorentzian. This is interpreted as a quasiparticle with dispersion relation $\epsilon_{\mathbf{k}}$ and half life $\frac{1}{\gamma}$. Since $\Im\Sigma(\mathbf{k}, \omega)$ changes its sign in correspondence of $\omega = \mu$, the condition of small imaginary part has meaning in that region, so we deduce that the quasiparticle have meaning in correspondence of the Fermi energy where they have a long half life.

There is another way to define the quasiparticles that results the most convenient one to perform a numerical computation. We refer once again to the Lehman expansion of the Green function (1.5): Here further, we will denote $f_a(\mathbf{x}, \alpha)$ the matrix element $\langle E_0^N | \Psi_{\alpha}^+(\mathbf{x}) | E_n^{N-1} \rangle$ and ω_a the energy $\epsilon_n^{N+1} + \mu$ in the case that $\omega_a \geq \mu$; in the remaining case we will address in the same way respectively $\langle E_0^N | \Psi_{\alpha}(\mathbf{x}) | E_n^{N+1} \rangle$ and $\mu - \epsilon_n^{N-1}$. Note that the set of $f_a(\mathbf{x}, \alpha)$ is complete but not orthonormalized The Green function in this notation becomes:

$$G_{\alpha,\beta}(\mathbf{x}, \mathbf{x}', \omega) = \sum_a \frac{f_a(\mathbf{x}, \alpha) f_a^*(\mathbf{x}', \beta)}{\omega - \omega_a + i\eta \text{sign}(\omega_a - \mu)} \quad (1.31)$$

If this expression is substituted in the Dyson equation (1.16) and analyzed in correspondence of a pole we get the following Schrödinger-like equation for the quasiparticles.

$$\left[-\frac{1}{2}\nabla^2 + U_{Ext} + U_H \right] f_a(\mathbf{x}, \alpha) + \int d^3x' \Sigma(\mathbf{x}, \mathbf{x}', \omega_a) f_a(\mathbf{x}', \alpha) = \omega_a f_a(\mathbf{x}, \alpha) \quad (1.32)$$

where the self-energy plays the role of a non-local potential. This is not a problem like the usual Hamiltonian one since the eigenvalues may be complex and their complex part is connected with the half life of the quasiparticle.

Chapter 2

The metal surface

Till now we have presented the properties of an infinite homogeneous system. Moreover, many properties of real physical systems are strongly dependent on spatial inhomogeneity. In particular we are interested in surfaces. In the present chapter we describe some physical properties of metallic surfaces referring to the simplest model used to describe a metal: the jellium.

2.1 Concepts in surface physics

2.1.1 Surface thermodynamics and energy

Considering a system with a plane interface between two phases, choosing an arbitrary position for the surface, a generic extensive variable may be written as [8]:

$$Y = y_1 V_1 + y_2 V_2 + y' A \quad (2.1)$$

where $y_{1,2}$ are the density of Y for the two components of the system, $V_{1,2}$ their volumes, while y' is a correction due to the presence of the surface of area A . If the position of the surface changes, equation 2.1 becomes:

$$Y = y_1(V_1 + A\Delta z) + y_2(V_2 + A\Delta z) + y'' A, \quad (2.2)$$

where Δz is the shift of the surface and y'' the correction for the new surface.

For defining the position of the surface, at this point, one refers to the number of particle and chooses the value of the coordinate of the surface as the one for which the correction introduced vanishes. Using this definition for a semi-infinite jellium the position of the surface defined in this way coincides with the boundary of the positive charge due to the neutrality of the system.

If Y is taken Ω , i. e. the Kramer grand potential, we obtain:

$$\Omega = p(V_1 + V_2) + \gamma A \quad (2.3)$$

because at equilibrium the pressure is the same for both phases. In this equation the parameter γ represents the surface energy (or surface tension). Because of the choice of the position of the surface, γ equals the surface excess free energy per unit area. In particular, for a system where γ is negative it is energetically convenient create surfaces, while in the opposite case, at the presence of a surface there corresponds an increase of the free energy.

2.1.2 Density of charge at the surface

We model the metal surface with the simplest possible profile: the positive background jumps discontinuously from 0 to the constant value $\rho = \frac{3}{4\pi(r_s)^3}$ inside the jellium. The electron charge responds to this inhomogeneity in a nontrivial fashion ref. [8], [24]: some negative charge spills out of the jellium border, leaving an excess positive charge on the inner side of the surface. This gives origin to the a surface dipole. Moreover inside the jellium the charge density is not constant, as in the homogeneous case, but it oscillates around the mean density of the infinite system. This oscillation, of Friedel type, is damped inside the surface. Its asymptotical behaviour is:

$$n(z) \xrightarrow{z \rightarrow -\infty} \rho \left[1 + \frac{\alpha \cos(2k_F z - \theta)}{z^2} + O\left(\frac{1}{z^3}\right) \right] \quad (2.4)$$

where ρ is the density for the homogeneous case, while the phase shift θ and the amplitude α depend on r_s in a nontrivial fashion [24]. Fig. 2.1 shows a typical density profile at the jellium surface.

2.1.3 The image potential

If we consider the effective potential in which the electrons move in correspondence of the surface, we see that the electrostatic part passes from the value inside the jellium to the vacuum value exponentially. The same happens if to it exchange effects are added. Instead, if we include the correlation effects the resulting potential behaves as a power law for distance from the surface larger than about $10 a_B$. This is explained with the fact that in the correlation effects there are the effect of long range interactions and the effects due to the image charge.

This behaviour may be understood with a simple model. We consider the jellium a perfect conductor, so that we can use the method of the image charge to describe the response to an external negative charge. The response of the system is to induce a surface density of charge such that the electric field inside the jellium results zero. This surface distribution produces

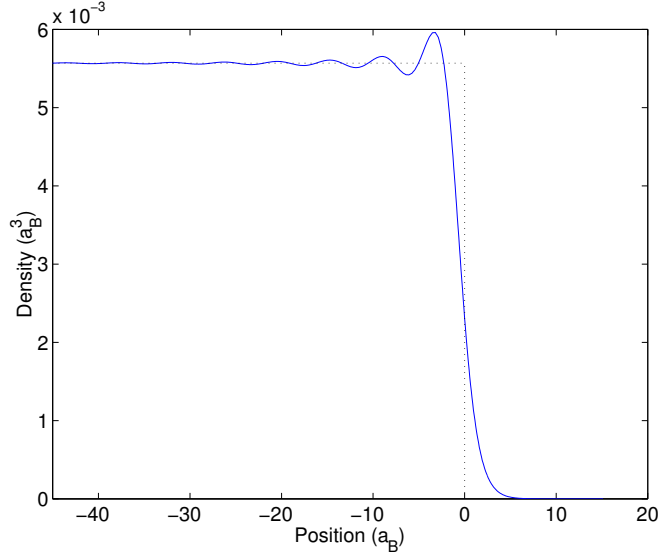


Figure 2.1: Solid curve: example of density $n(z)$ at the surface of an electron gas with $r_s = 3.5$ (the density is $5.568 \cdot 10^{-3} a_B^{-3}$). Computed in DFT-LDA for a slab of $210 a_B$ so that in the boundary region the effects of the interaction with the other surface may be neglected. Dotted the jellium slab profile.

the same field of a single positive charge placed inside the metal at a distance equal to the one at which the test charge finds itself. So the potential generated in correspondence of the surface presents a behaviour like $-\frac{1}{4z}$.

In the real case this trend describes well the potential generated by a surface at a distance larger than about $10 a_B$ with the correction that the precise position of the image plane is not precisely determined so that one must fit the real potential for this distances in order to determine it. The resulting potential is:

$$V = -\frac{1}{4(z - z_0)} \quad (2.5)$$

This kind of potential introduces a series of localized states called image states in proximity of the surface. Since the potential presents a behaviour similar to the one of the hydrogen atom, we deduce in analogy that there will be in correspondence of a surface a series of states with energies with a law of $-\frac{1}{16n^2}$. Obviously, one can measure the presence of this states only if in that region of energy there are not other states, like where their energy falls in a gap. For the metal, or for the jellium, there is not a gap so one will observe instead of this states the presence of a bulk state which increase its spectral weight in correspondence of a surface: these are the surface resonance.

2.2 The virial theorem and the surface energy of the jellium

In this section we want to present a relation between the components of the surface energy deduced by Vannimenus and Budd [38]. This property is based on the virial theorem. The starting point is the usual Hamiltonian for this system (eq: 1.3). Then one computes the expectation value of the total energy on a scaled state:

$$\psi(\lambda) = \lambda^{\frac{3N}{2}} \psi(\lambda \mathbf{x}_1, \lambda \mathbf{x}_2, \dots, \lambda \mathbf{x}_N) \quad (2.6)$$

where ψ is the ground state wave function. The resulting expectation value will have a minimum for $\lambda = 1$ since in that case we recover the ground state energy. The energy evaluated on this state will be:

$$E(\lambda) = \lambda^2 \langle \psi | T | \psi \rangle + \lambda \langle \psi | U_{ee} | \psi \rangle + \lambda \langle \psi | U_{eb}[n_+(\lambda)] | \psi \rangle + \lambda \langle \psi | U_{bb}[n_+(\lambda)] | \psi \rangle \quad (2.7)$$

where $n_+(\lambda)$ stand for $\lambda^{-3} n_+(\lambda^{-1} \mathbf{x})$, $n_+(\mathbf{x})$ being the density of the distribution of the positive charge. Since $E(\lambda)$ has a minimum for $\lambda = 1$ its derivate evaluated in that point must vanish. Computing the derivate one gets:

$$\begin{aligned} \frac{\partial E(\lambda)}{\partial \lambda} = & 2\lambda \langle \psi | T | \psi \rangle + \langle \psi | U_{ee} | \psi \rangle + \langle \psi | U_{eb}[n_+(\lambda)] | \psi \rangle + \lambda \frac{\partial}{\partial \lambda} \langle \psi | U_{eb}[n_+(\lambda)] | \psi \rangle + \\ & + \langle \psi | U_{bb}[n_+(\lambda)] | \psi \rangle + \lambda \frac{\partial}{\partial \lambda} \langle \psi | U_{bb}[n_+(\lambda)] | \psi \rangle \end{aligned} \quad (2.8)$$

For $\lambda = 1$, using the fact that neither $\langle \psi | T | \psi \rangle$ nor $\langle \psi | U_{ee} | \psi \rangle$ depend on λ and equaling it to zero one gets:

$$2 \langle \psi | T | \psi \rangle + \langle \psi | V | \psi \rangle = - \frac{\partial}{\partial \lambda} E[n_+(\lambda)]|_{\lambda=1} \quad (2.9)$$

This statement is the virial theorem.

Since the total energy may be written as a bulk contribute plus a surface term ($E = N\epsilon_P + A\gamma$), by computing its derivate with respect to λ the virial theorem implies:

$$2 \langle \psi | T | \psi \rangle + \langle \psi | V | \psi \rangle = 3N\rho \frac{d\epsilon_P}{d\rho} + A \left(3\rho \frac{d\gamma}{d\rho} - 2\gamma \right) \quad (2.10)$$

where ρ is the bulk density. Since the kinetic and the interaction part of the total energy can be individually expanded as sum of a bulk plus a surface contribute one deduces the following relations for the components:

$$k = - \frac{dr_s \epsilon_P}{dr_s} \quad (2.11)$$

$$u = \frac{1}{r_s} \frac{dr_s^2 \epsilon_P}{dr_s} \quad (2.12)$$

$$\gamma_k = -\frac{1}{r_s^2} \frac{dr_s^3 \gamma}{dr_s} \quad (2.13)$$

$$\gamma_v = \frac{1}{r_s^3} \frac{dr_s^4 \gamma}{dr_s} \quad (2.14)$$

where k and u are the bulk kinetic and interaction terms and γ_k γ_v are the surface ones.

Note that the exact results deduced here can not be applied to the standard DFT description of the total energy into a kinetic and potential term, since in this approximation the kinetic term is not the exact one, but is the one of non interacting particles; moreover some of its corrections are included inside the exchange and correlation term so that even the interaction term cannot be described in this way. In particular it is possible to extend this theoretical approach within the DFT-LDA theory so that for the kinetic surface energy expressed in this formalism (γ_s) it is possible to demonstrate the following relation:

$$\gamma_s = -\frac{1}{r_s^2} \frac{dr_s^3 \gamma}{dr_s} + \int_{-\infty}^{\infty} dz \left[n(z) \left(\frac{dr_s \epsilon_C}{dr_s} \Big|_{n(z)} - \frac{dr_s^3 \epsilon_C}{dr_s} \Big|_{\rho} \right) \right] \quad (2.15)$$

where ϵ_C is the bulk correlation energy.

2.3 The jellium surface

In this section we discuss previous work about some models used to describe the jellium surface. Most of these works treat this problem using the geometry of a semi-infinite jellium: the positive uniform charge is present in the region of space with negative z coordinate while in the remaining space there is the vacuum. Another possibility is, as in this thesis, to use a slab geometry (see sec. 3.2). This is done by a periodical repetition of a fixed jellium thickness separated by regions of vacuum. This choice has the advantage that permit the use of the simplifications due to Bloch theorem, but the disadvantage is the need to consider the interactions between the surfaces. The small dimensions of the slabs introduce particular property we will show an example of in the end of this section. For the computations different approximations are used; in particular we will present the results from the Thomas-Fermi one and on the DFT, while there are other possibilities like

the Hartree-Fock approximation [5], [32] or the Monte Carlo methods [2]. The LDA is an approximation that presents some failures description of the jellium surface, since in that region the Kohn-Sham wavefunctions become evanescent, while this approximation is thought for a bulk system where the density varies slowly. So there has been proposed parametric models in order to give more accurate description [22], [27], or approximation different from the LDA [40] in order to improve the accuracy.

2.3.1 The Thomas-Fermi approach

We first discuss the jellium surfaces using Thomas-Fermi theory. The functional of this model [8] considers only the kinetic energy (1.4) plus the electrostatic terms so that one has to study the following functional, with the jellium background density $n_+ = n(\mathbf{x})$ constant equal to ρ in the region of negative z and null elsewhere:

$$E[n(\mathbf{x})] = \frac{3}{10}(3\pi^2)^{2/3} \int [n(\mathbf{x})]^{5/3} d^3x + \frac{1}{2} \int d^3x d^3x' \frac{n(\mathbf{x})n(\mathbf{x}')}{|\mathbf{x} - \mathbf{x}'|} + \frac{1}{2} \rho^2 \int_{z < 0, z' < 0} d^3x d^3x' \frac{1}{|\mathbf{x} - \mathbf{x}'|} - \rho \int_{z < 0} d^3x d^3x' \frac{n(\mathbf{x}')}{|\mathbf{x} - \mathbf{x}'|}. \quad (2.16)$$

By computing the variation one gets the following equation for the density of the system:

$$V_{es}(\mathbf{x}) + \frac{1}{2}[3\pi^2 n(\mathbf{x})]^{2/3} = \mu, \quad (2.17)$$

where $V_{es}(\mathbf{x})$ is the electrostatic potential solves the Poisson equation:

$$\nabla^2 V_{es}(\mathbf{x}) = -4\pi[n(\mathbf{x}) - \rho\theta(-z)]. \quad (2.18)$$

Substituting $V_{es}(\mathbf{x})$ from eq. (2.17) into eq. (2.18) and using the invariance under the translations in the planar directions one deduces the following equation:

$$\frac{1}{2}[3\pi^2]^{2/3} \frac{d^2}{dz^2} [n(z)]^{2/3} = 4\pi[n(z) - \rho\theta(-z)]. \quad (2.19)$$

Solving this equation with the boundary conditions that $n(z) \rightarrow 0$ for $z \rightarrow +\infty$ and $n(z) \rightarrow \rho = \frac{3}{4\pi(r_s)^3}$ for $z \rightarrow -\infty$ one deduces the density for this system in the Thomas-Fermi approximation. It does not present any oscillation and decays as z^{-6} for $z \rightarrow +\infty$, while converge exponentially to its asymptotic value for $z \rightarrow -\infty$. The resulting surface energy is always negative so that, according to this theory, the jellium should be unstable through the formation of surfaces.

Form this considerations it emerges that this model is not sufficiently accurate to describe the surfaces of the jellium; in order to improve its accuracy one may introduce the von Weizsäcker correction to the kinetic term, plus the effects of the exchange and correlation energy [37]. The energy functional becomes

$$E[n(\mathbf{x})] = \int \left[\frac{3}{10}(3\pi^2 n(\mathbf{x}))^{\frac{2}{3}} + \frac{1}{72} \left(\frac{1}{n(\mathbf{x})} \nabla_{\mathbf{x}} n(\mathbf{x}) \right)^2 \right] n(\mathbf{x}) d^3x + E_{XC}[n(\mathbf{x})] + \frac{1}{2} \int V_{es}(\mathbf{x}) [n(\mathbf{x}) - \rho \theta(-z)] d^3x. \quad (2.20)$$

Several novelties are introduced by this model. The behaviour for large z trends to zero exponentially. Density oscillations appears inside the jellium, but these are not of Friedel type, as their wavevector is not $2k_F$, besides they are damped exponentially rather than with a power law.

2.3.2 The density-functional approach

In their work Lang and Kohn [24] studied the surface of the jellium through the DFT by analyzing a semi-infinite jellium. From solving the set of Kohn-Sham equations (1.12) in this geometry one gets eigenfunctions of the type:

$$\phi_{k,k_x,k_y} = \phi_k(z) e^{i(k_x x + k_y y)}, \quad (2.21)$$

where $\phi_k(z) \sim \sin[kz + \theta(k)]$ for $z \rightarrow -\infty$. The corresponding continuum eigenvalues referred to the chemical potential are:

$$\epsilon_{k,k_x,k_y} = \frac{1}{2}(k^2 + k_x^2 + k_y^2 - k_F^2). \quad (2.22)$$

The total electron density decays exponentially for $z \rightarrow +\infty$, while its other asymptotic behaviour is characterized by the Friedel oscillations

$$n(z) \xrightarrow{z \rightarrow -\infty} \rho \left[1 + \frac{3 \cos 2(k_F z - \theta(k_F))}{(2k_F z)^2} + O\left(\frac{1}{z^3}\right) \right]. \quad (2.23)$$

The effective potential, where the electrons move, inside the jellium, presents only small oscillations since the electrostatic and the exchange and correlation contribution are such that part of the oscillations cancels each other. At large positions z an exponential behaviour (instead of the $-\frac{1}{4x}$ expected for the image potential) is found.

In the same paper Lang and Kohn analyze the surface energy into its components as the bulk jellium; γ is rewritten as:

$$\gamma = \gamma_K + \gamma_{XC} + \gamma_{Coul} \quad (2.24)$$

where the first is a kinetic contribution, the second an exchange and correlation one and the last an electrostatic contribution. The kinetic term was found negative for each value of r_s because the charge is more spread out in presence of a surface. In addition $\gamma_{XC} > \gamma_{Coul}$: for this reason the computation with the Thomas-Fermi or Hartree approximation are inadequate to describe this system.

2.3.3 The jellium slab in DFT

The DFT was applied to study the jellium surface also in the slab geometry [35]. In this case the system under study is constituted by a region $z_1 < z < z_2$ of positive charge, with vacuum in the remaining space. Once again as, like the previous case, the eigenfunctions of the auxiliary system may be written as a product of plane waves for the directions with translational invariance times a function solution for the equation in the remaining direction:

$$\phi_{n,k_x,k_y} = \phi_n(z)e^{i(k_x x + k_y y)}. \quad (2.25)$$

In this case we do not have more informations about the behaviour of $\phi_n(z)$, except for the fact that because of the symmetry of the problem, these functions must be symmetric or antisymmetric for the transformation $z \rightarrow -(z - \frac{z_2 - z_1}{2}) + \frac{z_2 - z_1}{2}$. In the same way the eigenvalues will be the sum of two parts: $\frac{k_x^2 + k_y^2}{2}$ plus the contribution due to the solution in the direction orthogonal to the surface. In the z direction there appears a discrete set of eigenvalues. As illustrated in fig. 2.2 each of this eigenvalues shows a decreasing behaviour as a function of the slab thickness D with a damped oscillation of wavelength almost equal to $\frac{\pi}{k_F}$, where k_F is the bulk Fermi momentum. The thicknesses D_n , at which the cusps for this oscillations finds, correspond to the point where the the eigenvalues intersect the Fermi energy.

Coming to the total electron density (see fig. 2.3), in a first approximation, the behaviour near a surface is essentially the same as of the semi-infinite geometry: there is a exponential decrease outside the slab region, while inside there are the Friedel oscillations. However small differences in the electron density dependent on slab thickness. In an interval of thicknesses between two maxima of the eigenvalues oscillations one observes that the charge density at a fixed position outside the slab oscillates as a function of the thickness. Two minima of charge are located in correspondence of the extremes of the interval. This implies a variation in the surface dipole since the increase of charge outside the slab must be compensated by a decrease in its interior.

This behaviour is explained as follow. At thickness D_n another wavefunction starts to contribute to the electron density. Since it has a larger number

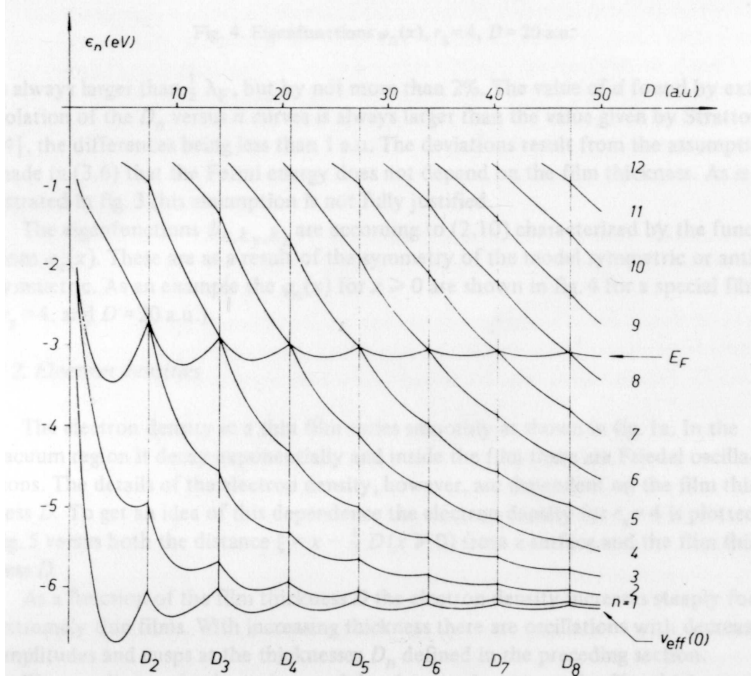


Figure 2.2: Kohn-Sham eigenvalues as function of the slab thickness $r_s = 4$ (from ref. [35]).

of nodes and a more slowly decreasing tail, it induces a larger probability that the last electron is located outside the slab: so that the surface dipole increases as the thickness D exceeds D_n . As the thickness increases the eigenvalues decrease and that the density of charge outside the slab decreases with increasing localization of the wavefunctions.

Due to self-consistency the effective potential in which the electrons move, at a fixed slab thickness, oscillates near the surface due to the Friedel oscillations in the charge density. As for the density, these oscillations depend on the slab thickness, since are mainly due to the ones in the surface dipole. The other contribute to the potential is due to the exchange and correlation term which is the greatest in the effective potential. In practice the variations of the surface dipole cause an oscillating shift in the bottom of the effective potential. In correspondence of the slab edge, the behaviour of the potential as function of the slab thickness may be described as a shift of its step with respect to the jellium surface. So, starting from D_n , the step is first shifted outside the surface then, after a maximum, it moves inward.

This explains the variations in the eigenvectors. If one considers a simplified model based on a flat potential [8] with infinite barriers then the eigenvalues should decrease as a function of D . The difference with respect

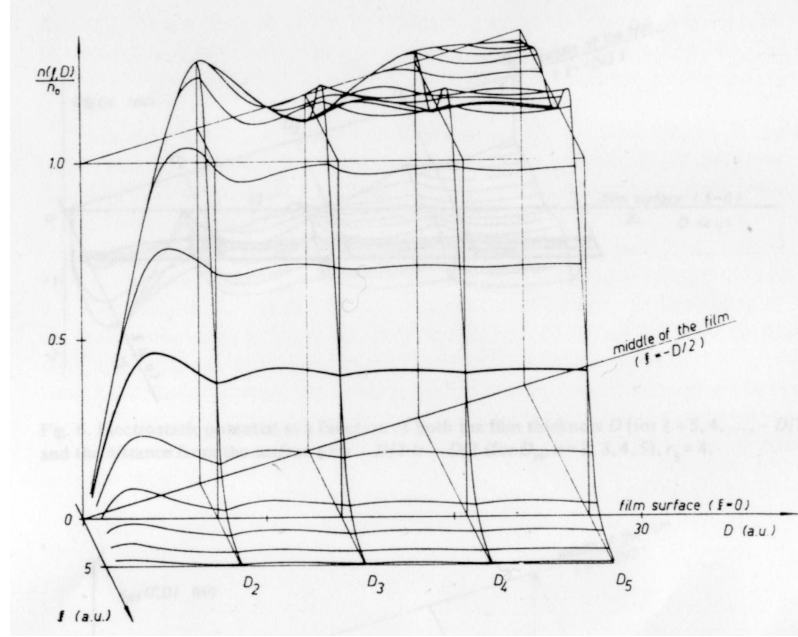


Figure 2.3: Density of charge as function of the position and the slab thickness $r_s = 4$ (from ref. [35]).

to this model is an oscillating function are due to the shift of the bottom and of the step in the effective potential whose effect is to make the eigenvalues to decrease more rapidly. So for thickness near D_n they decrease more quickly than expected in the infinite barrier model, and then, with the changing behaviour of the potential, they decrease more slowly (or even increase).

2.3.4 Other the quantum size effects: the work function

The oscillations in the total energy and in its components, that we study in this thesis, are examples of the so called quantum size effects (QSE). These effects are due to the fact that cases the thickness of the slab is very small (i. e. only few Bohr radii), and become irrelevant on a macroscopically large sample.

A related example of these effects in a jellium slab is found in the behaviour of the work function [35], [28], [39]. It has been determined by calculations (see fig. 2.2) for very small slabs that it presents a singular oscillatory behaviour around a constant value. Since the Fermi energy may be written as the sum of the energy of the effective potential in the middle of the slab plus the energy of the last occupied state misured with respect

to the bottom of the potential, we can distinguish two contribution to the work function (which is the opposite of the Fermi energy). These oscillations are induced principally by the effective potential ($v_{eff}(0)$) (see sec. 2.3.3). Also the other term oscillates, but with a smaller amplitude compared to the other term.

This kind of effect has been also observed in real metals. For example, Boettger in his work [6] studied the (111) surface of aluminium. He observed the presence of oscillations in the work function. Of course the real metal suffers for the additional difficulty that the presence of a discrete lattice makes possible to study only a discrete number of thicknesses related to the different number of atomic layers.

Chapter 3

Technical aspects of the calculations

3.1 Method of computation

The DFT-LDA maps the many electron interaction problem to a single electron calculation. The first problem one must face in order to solve the Kohn-Sham equations numerically is due to the fact that it is impossible to invert this equations because the potential, too, depends from the density and so from the eigenfunctions. So to perform this computations a standard self-consistent procedure is adopted: the computations starts from an arbitrary initial density used to determinate an initial potential. At this point the potential determined in this way is used to solve the equations that now are independent. The solutions give a new density, given by the sum of the square moduli of the wave functions. This new density is then used to calculate a new potential used once again for the solution of the equations. This procedure is iterated till the condition for which the difference of the total energies of two successive steps are sufficiently small (self-consistency) is reached.

Another simplification of the problem is due to the presence of a periodicity in the system under study. In a periodic lattice, the Bloch theorem [3] permits to rewrite the electrons wave functions as a product of a plane wave with \mathbf{k} inside the first Brillouin zone times a function with the periodicity of the lattice. Thus, using a plane-wave set of functions, labelled by reciprocal lattice vectors \mathbf{G} , to expand the periodic part the electron wave function becomes:

$$\psi_{j,\mathbf{k}}(\mathbf{x}) = \sum_{\mathbf{G}} c_{j,\mathbf{k}+\mathbf{G}} e^{i(\mathbf{k}+\mathbf{G})\cdot\mathbf{x}}. \quad (3.1)$$

In this basis it is possible to rewrite the Kohn and Sham self-consistent equations using this expression for the wave functions. Integrating over \mathbf{x} , the equations become an algebraic system for the Fourier coefficients, $c_{j,\mathbf{k}+\mathbf{G}}$:

$$\begin{aligned} \sum_{\mathbf{G}'} \left[\frac{1}{2} |\mathbf{k} + \mathbf{G}|^2 + V_{ext}(\mathbf{G} + \mathbf{G}') + V_H(\mathbf{G} + \mathbf{G}') + V_{XC}(\mathbf{G} + \mathbf{G}') \right] c_{j,\mathbf{k}+\mathbf{G}} = \\ = \epsilon_j c_{j,\mathbf{k}+\mathbf{G}} \end{aligned} \quad (3.2)$$

In this way the problem is reduced from the solution of a differential equation to the one of a system of algebraic equations for each of the infinite number of \mathbf{k} -points.

Even if for each \mathbf{k} -point only a numerable set of plane waves (due to the Born-von Karman boundary condition) is involved, their number still remain infinite, thus impossible to implement in a code. However smooth functions are represented by rapidly damping Fourier coefficients, which makes the plane waves of small kinetic energy more important than the others. So it is a reasonable approximation to truncate the basis set at a maximum value of the kinetic energy (or equivalently momentum) of the plane waves. With this approximation one needs to check that the value of the cut-off energy introduces only small errors in the computed results (see sec. 3.3).

3.1.1 Mapping the Brillouin zone: the \mathbf{k} -points

In principle the electronic wave functions should be computed at an infinite number of \mathbf{k} -points in the Brillouin zone to carry out integration in that region. In practice this integration is realized by the use of a finite grid of points suitably chosen [11]. This method works because the \mathbf{k} dependence of all considered functions are continuous.

For the present computations the choice of this set is done using the Monkhorst-Pack grid [29].

$$\mathbf{k}_i = u_{i_1} \mathbf{b}_1 + u_{i_2} \mathbf{b}_2 + u_{i_3} \mathbf{b}_3, \quad (3.3)$$

where \mathbf{b}_n ($n = 1, 2, 3$) are the reciprocal lattice vectors and the coefficients:

$$u_{i_n} = \frac{2p_n - l_0 - 1}{2l_0}, \quad (3.4)$$

where l_0 is a positive integer and p_n assumes all integer values between 1 and l_0 . Note that this set of \mathbf{k} -points contains $\mathbf{k} = 0$, the so called Γ point, only for odd values of l_0 .

In the ABINIT code it is possible to add an extra shift to this grid.

3.1.2 The smearing

The assumption of continuity in the approximate \mathbf{k} -space integrations is violated by the functions related to the $T = 0$ Fermi occupancies of a metallic band. The regularization of the finite \mathbf{k} sums is obtained by introducing a new smooth function for the occupancy in analogy to what happens at a finite temperature. So the function which controls the occupancies $f(\epsilon)$ is defined through the relation:

$$f(\epsilon) = \int_{-\infty}^{\epsilon} g(t) dt \quad (3.5)$$

if $g(t) = \delta(t)$ one obtains the usual zero-temperature distribution, while with a broad distribution one gets a continuous occupation, similar to finite temperature. This kind of approximation introduces a systematic error in the computation of the ground-state energy. Recently it was proposed to correct it by adding an entropy contribution to the total energy.

A possible smearing function is the Gaussian:

$$g(t, T) = \frac{1}{\sqrt{\pi}} e^{-\left(\frac{t}{T}\right)^2} \quad (3.6)$$

where T is an energy parameter effectively representing a temperature. The default choice of the ABINIT code is another smearing function [26], the so called Marzari cold smearing, namely:

$$g(t, T) = \frac{1}{\sqrt{\pi}} e^{-\left(\frac{t}{T}\right)^2} \left\{ 1.5 + \frac{t}{T} \left[-1.5 a + \frac{t}{T} \left(-1 + a \frac{t}{T} \right) \right] \right\} \quad (3.7)$$

where $a = -0.5634$. The advantage of this choice is a better convergence of the total energy even for relatively high smearing temperature. Note that according to this choice the occupation numbers (including the spin degeneracy) may be slightly greater than 2.

3.1.3 The ions: the pseudopotential approximation

For describing the ionic positive charge and the inner core electrons it is a standard approach to introduce the so called pseudopotential. This starts from the observation that the electrons of the lowest energy levels of the atoms are localized near their nuclei and the properties in which one is interested depend mainly on the valence electrons. So the potential of the real nuclei are substituted by new pseudopotentials that act only on the valence wavefunctions. The advantage are the reduced complexity of the system and the necessity of much fewer plane waves because there is no need of describing the rapid oscillations of the wavefunctions inside the core region.

A pseudopotential must describe the valence electrons outside the core region. For this reason the eigenvalues of the valence states of the pseudoatom are required to be the same as the real ones, at least in the case of an isolated atom. In addition it is required that the wavefunctions of the valence electrons of the pseudo and the real atom coincide outside a "core radius" r_c , while inside r_c the pseudo wavefunction will not oscillate. At least for each valence state the integral of the square moduli of the pseudo and real wavefunction must be the same for each $r > r_c$: the pseudopotential which fulfill this condition are called norm-conserving pseudopotential. This property guarantees that a every r outside r_c there is the same charge as in the real atom.

3.1.4 The jellium background

To describe our model metal within the jellium approximation there is no need of pseudopotential. Thanks to the correspondence between the external potential and the density of the ground state, it is possible to introduce the jellium by providing an external potential which is generated by the proper positive background.

Consider a slab confined between z_1 and z_2 the potential induced by the background is known from the solution of the Poisson equation:

$$\nabla^2 v_{ext}(\mathbf{x}) = -4\pi\rho\theta(z - z_1)\theta(z_2 - z). \quad (3.8)$$

This equation can be solved in reciprocal space using the invariance under the x - y plane translations. One obtains:

$$v_{ext}(\mathbf{G}) = \frac{4\pi n_+(G_z)}{G_z^2} \delta_{G_x,0} \delta_{G_y,0}. \quad (3.9)$$

This relate the Fourier transform of the potential to the one of the background density of charge. As usual, for $\mathbf{G} = 0$ the potential component diverge, but thanks to the neutrality of the system this contribution cancels other diverging terms.

The Fourier transform of the density is:

$$\begin{aligned} n_+(G_z) &= \frac{1}{L_z} \int_0^{L_z} n_+(z) e^{-iG_z z} dz = \frac{\rho}{L_z} \int_{z_1}^{z_2} e^{-iG_z z} dz = \\ &= \frac{3}{4\pi r_s^3 L_z G_z} [\sin(G_z z_2) - \sin(G_z z_1) + i(\cos(G_z z_2) - \cos(G_z z_1))]. \end{aligned} \quad (3.10)$$

This is the way the external potential was implemented in the ABINIT code by S. Caravati.

3.2 The supercell

The plane wave basis, described in sec. 3.1, applies only to a periodic system. For a non periodic system, to use this basis one needs to introduce a fictitious periodicity. By the use of sufficiently large cell (the supercell) one reproduces the properties of a non periodical system reported in space in a fictitious lattice. This method starts from the assumption that if the lattice imperfections are far enough the interactions will be negligible. This assumption must be verified with a suitable convergence test.

In our case the surface is the origin of the lack of periodicity in its orthogonal direction . As just describe it is possible to introduce a supercell in that direction made by a certain slab of the material under study alternated with regions of vacuum, as illustratede in fig. 3.1. We need to check that the effects due to the interactions neither between two different slabs nor between the two surfaces of the same slab.

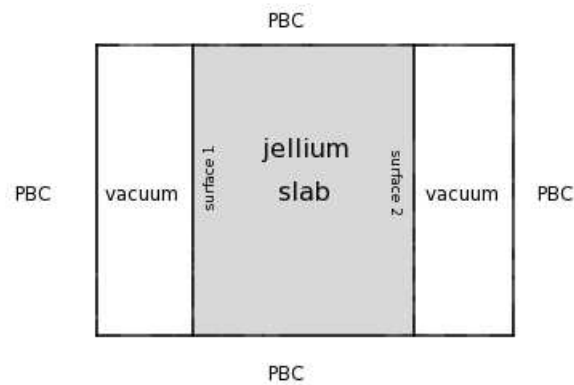


Figure 3.1: graphical representation of the slab geometry.

3.3 Convergence study

We report here the studies of convergence done for the jellium system. When possible we refer to the much simpler bulk case, while analogous tests has been done for the slab.

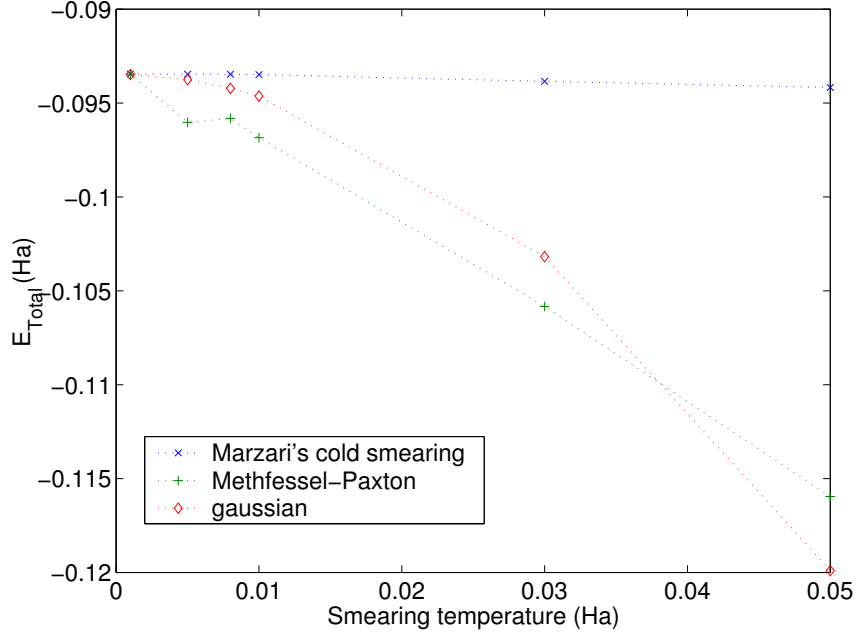


Figure 3.2: Comparison of different smearing functions. The computations has been done for $r_s = 2.07$, a cell of $7.65*7.65*7.65a_B$, a grid of $16*16*16$ \mathbf{k} -points, i. e. a density of $7393 a_B^3$ \mathbf{k} -points.

3.3.1 Study of the smearing functions

To choose the smearing function we have done several computations with the different smearing functions (Gaussian, Methfessel and Paxton with Hermite polynomial of degree 2, and Marzari cold smearing) with different "temperatures". The results are summarized in fig. 3.2. With the Marzari cold smearing the total energy converges faster with temperature. For this reason, awe have adopted this smearing method.

3.3.2 Convergence of \mathbf{k} -points and smearing temperature

The choice of the smearing temperature is strictly related to the choice of the mesh of \mathbf{k} -points. Since the smearing has been introduced to improve the accuracy of the mesh of \mathbf{k} -point we need to study the convergence of these two parameters together. We expect that the results will be converged for a larger number of \mathbf{k} -point and small smearing temperature. The total energy results are shown in fig. 3.3. The good compromise between the accuracy of results and the needed of not making too heavy computations is obtained

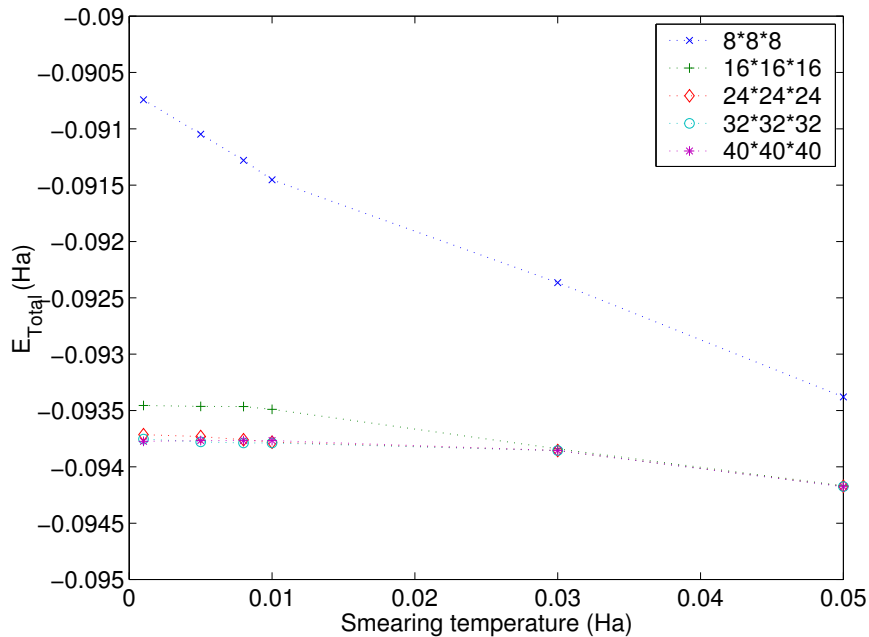


Figure 3.3: Convergence of the total energy as a function of number of \mathbf{k} -points and smearing temperature. $r_s=2.07$ cubic cell of volume $447.7 a_B^3$.

with a grid of $16*16*16$ \mathbf{k} -points, for this specific cell volume, and a smearing temperature of 0.01 Ha.

3.3.3 Convergence against the cut-off energy

For the bulk jellium this parameter does not influence the results of the total energy as long as it has been chosen greater than the Fermi energy of the system. For the bulk the solutions of the Kohn and Sham equations are exactly plane waves and, so, the base used describe perfectly the solutions once every wave vector is contained in the set of base functions, or, in other words, the maximum kinetic energy of the electrons is smaller than the maximum energy of the plane waves included in the basis.

For the slab geometry instead, the charge density and the potential vary, thus wavefunctions result combination of all basis states, and the cut-off parameter influences the total energy. So there is the need of a study of convergence. We perform this test for a slab of thickness $D = 30 a_B$ and $r_s = 3.5$. We obtain very small differences in the total energies with a cut-off of 12 Ha which will be used here further unless otherwise specified.

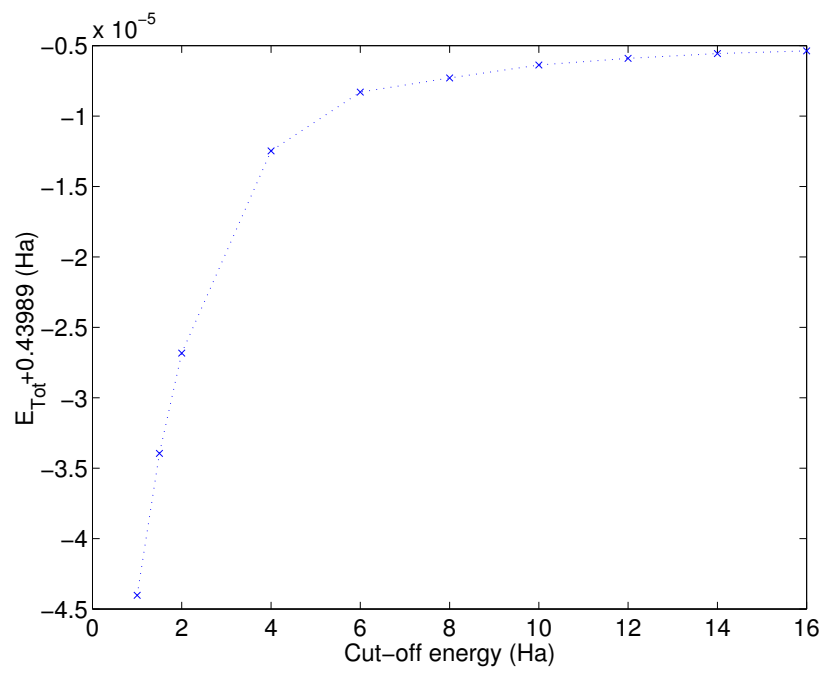


Figure 3.4: Convergence on cut-off energy for a slab of $D = 30 a_B$ and $r_s = 3.5$.

Chapter 4

The infinite bulk jellium

4.1 Analytic computation

To obtain the energy in the uniform bulk metal we start from the Hohenberg and Kohn functional for the total energy (eq. 1.11) to which the term due to the background-background ($E_{\rho\rho}$) interaction is added. For this special geometry, as mentioned in sec. 1.2, the sum of the Hartree energy plus the ones due to the background vanish. There remain therefore:

$$E^{(HK)}[n] = T_0[n] + \int \epsilon_{XC} n dr \quad (4.1)$$

where the exchange and correlation energy is written in LDA for this special case, for which neither ϵ_{XC} nor n depend on the position.

From this functional, the consequent set of Kohn and Sham equations is:

$$\left[-\frac{\nabla^2}{2} + \epsilon_{XC} \right] \psi_i = \epsilon_i \psi_i \quad (4.2)$$

The solutions of this set of equation are plane waves, but the eigenvalues are translated by ϵ_{XC} with respect to the case of free particles.

The resulting energy per particle is:

$$\frac{E}{N} = \frac{T_0[n]}{N} + \epsilon_{XC} \quad (4.3)$$

The ϵ_{XC} term is given by the chosen parameterization and the kinetic deduced in the same way of the free gas case results $\frac{3}{5}\epsilon_F = \frac{3}{10}(3\pi^2\rho)^{\frac{2}{3}}$. In the end the energy per particle for an infinite jellium in DFT is:

$$\frac{E}{N} = \frac{3}{5}\epsilon_F + \epsilon_{XC}(n) = \frac{3}{10} \left(\frac{9\pi}{4} \right)^{\frac{2}{3}} \frac{1}{r_s^2} + \epsilon_{XC}(r_s) \quad (4.4)$$

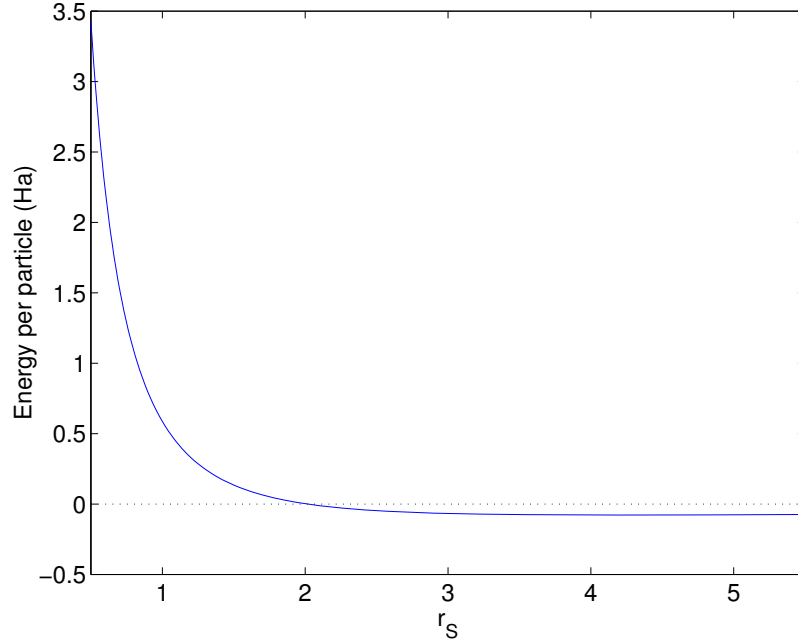


Figure 4.1: Energy per particle for a jellium in DFT.

Likewise, the energy per unit volume is:

$$\frac{E}{V} = \frac{3}{5}\rho\epsilon_F + \rho\epsilon_{XC} = \frac{1}{10\pi^{\frac{4}{3}}}\left(\frac{9}{4}\right)^{\frac{5}{3}}\frac{1}{r_s^5} + \frac{3}{4\pi^2 r_s^3}\epsilon_{XC}(r_s) \quad (4.5)$$

Using the Teter-Padé parameterization for the exchange and correlation energy [15] the energy per particle as a function of r_s has the shape reported in fig 4.1. In particular its sign changes at $r_s = 2.01405$, decrease to a minimum at $r_s = 4.18821$ and then increases to zero as $-\frac{1}{r_s}$ for $r_s \rightarrow \infty$.

4.2 Numerical simulations

We compare the analytical expression with a numerical computation of the total energy for a infinite jellium made using a modification of a standard DFT-LDA package (ABINIT [1]). We used a cubic cell containing $N = 12$ electrons so that the lattice parameter $a = \left(\frac{4\pi N}{3}\right)^{\frac{1}{3}} r_s$ is fixed once r_s is chosen. For the cutoff energy a value of 12 Ha has been chosen, well over the value of ϵ_F so that the computation is converged without any doubt (as this is an homogeneous system, the solutions are plane waves and they are completely described using a set of plane waves with maximum wave vector

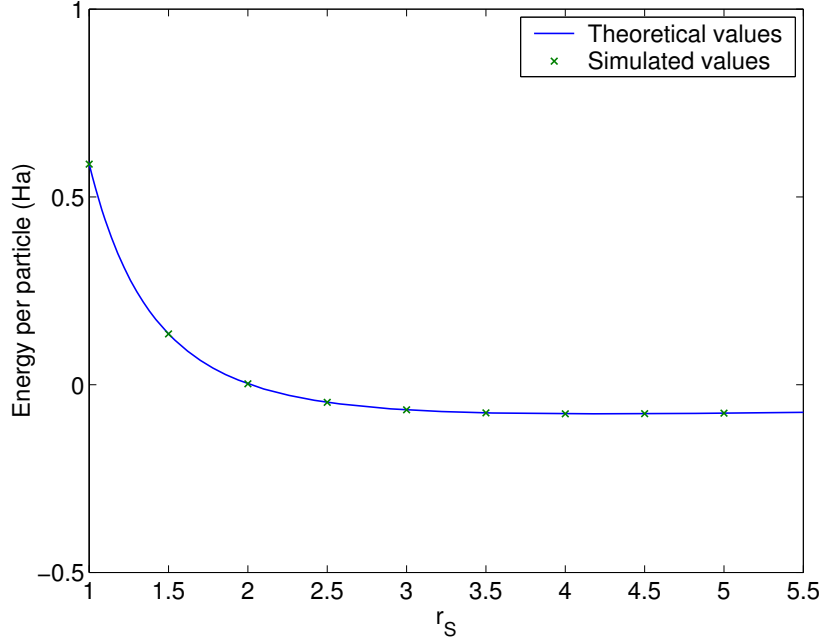


Figure 4.2: Comparison between the simulated values with the analytical ones.

k_F). The smearing temperature chosen is of 0.01 Ha with the Marzari cold smearing. As the \mathbf{k} -points test of convergence tell us (sec. 3.3.2), we use a grid of $16*16*16$ \mathbf{k} -points for $r_s = 2$: for all larger r_s the same grid has been used, while for the smaller larger grid have been used in order to keep the same \mathbf{k} -point density in the Brillouin zones.

The total energy obtained by numerical calculation is compared with the analytical one in the following table. All the energy are expressed in Ha.

r_s	E simulated	E/N simulated	E/N theoretical	Difference (%)
1	7.049246	0.587437	0.587436	0.00013
1.5	1.622745	0.135229	0.135242	0.0096
2	0.031495	0.002625	0.002599	0.983
2.5	-0.560795	-0.046733	-0.046743	0.0217
3	-0.802398	-0.066866	-0.066868	0.0024
3.5	-0.898781	-0.074898	-0.074897	0.0024
4	-0.928768	-0.077397	-0.077394	0.0049
4.5	-0.926642	-0.077220	-0.077214	0.0079
5	-0.908657	-0.075721	-0.075712	0.0119

As expected the differences are very small, so that the simulated results are in a good agreement with the analytical values.

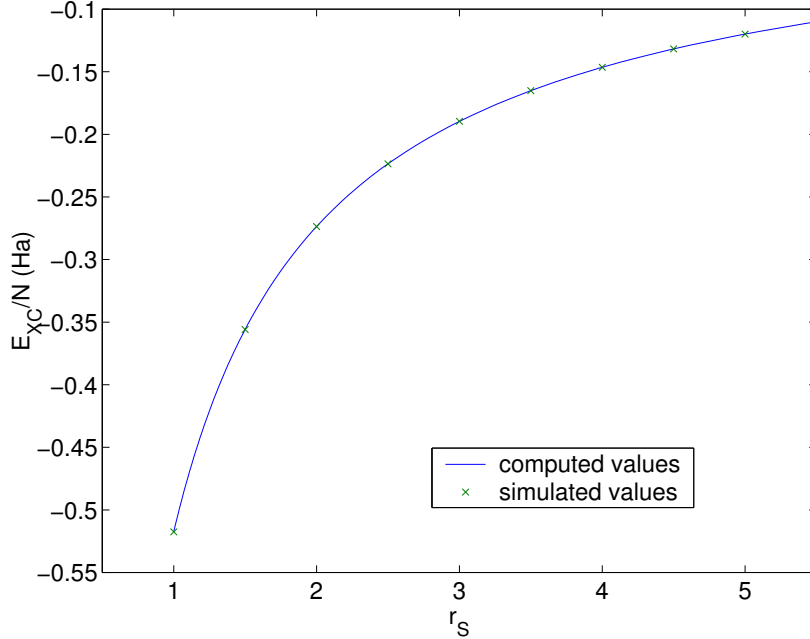


Figure 4.3: Comparison of the exchange and correlation terms.

4.3 Comparison of components of the total energy

In this section the analysis of the previous results is presented by studying one by one the components of the total energy divided by the number of particles in the unit cell.

We start from the exchange and correlation term, which is expected to be exact in the bulk case since the LDA functional is determined by making local the functional for the bulk. As may be observed in fig. 4.3 the numerical values are in perfect accord with the theoretical expression.

The same applies to the sum of the Hartree contribution plus the ones due to the interactions between the electron with the background and the background with itself, which vanishes due to charge neutrality.

The kinetic contribution to the energy is expected to equal $\frac{3}{5}\epsilon_F = \frac{3}{10} \left(\frac{9\pi}{4}\right)^{\frac{2}{3}} \frac{1}{r_s^2}$. As it is possible to notice in fig. 4.4 there are only small differences even if these are the greatest contributions to the differences in the total energy. Indeed the kinetic term contain all the errors due to a non perfect convergence of the numerical results associated to a finite number of \mathbf{k} -points and Fermi surface smearing.

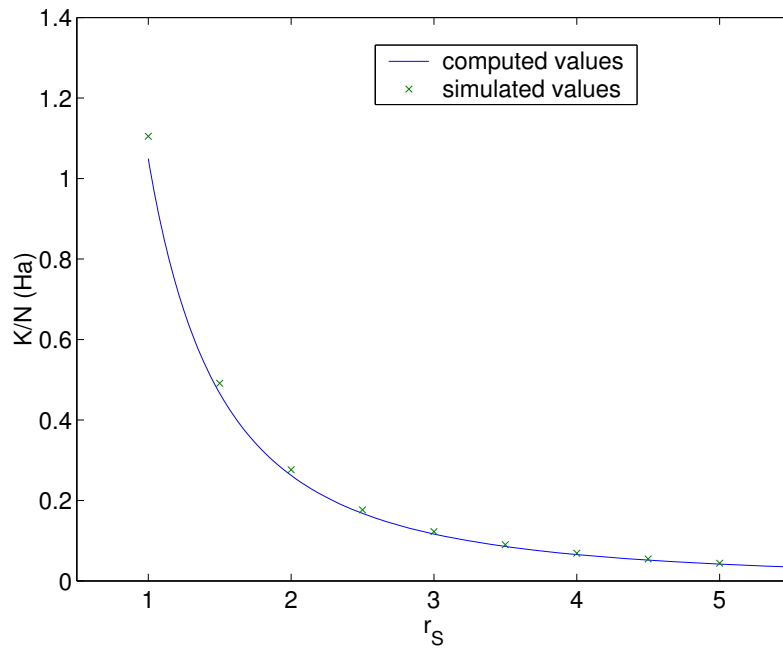


Figure 4.4: Comparison of the kinetics terms.

Chapter 5

Computation of the surface energy

5.1 Simulation with ABINIT

5.1.1 Computation and results

To evaluate the surface energy γ we have executed a number of computations in the slab geometry, where the total energy is expected to be:

$$E_{total} = \epsilon_p \rho V + 2\gamma A + E_{surf-surf} \quad (5.1)$$

where $V = AD$ and A are respectively the volume and the area of the jellium in the cell used for the computations, ϵ_p is the energy per particle for the uniform gas and the factor 2 before the surface energy is due to the presence of two surfaces of the slab. Neglecting small surface-surface interactions the energy per unit surface area grows linearly with the thickness D of the slab.

To extract γ , we have carried out calculations with different thicknesses D , but unit cells with the same size in the planar directions, whenever possible. The thickness was modified together with the number of electron per cell in order to keep the density fixed. We changed the lateral dimensions of the unit cell only if, because the charge in a cell needs to be integer, the thickness required to respect this condition, or if the ratio between the side of the cell was excessive to be treated with the ABINIT code. This choice has been done in order to preserve, for the different computations, a similar accuracy in mapping the Brillouin zone with the \mathbf{k} -points.

For these computations we reputed at convergence the total energy using a mesh of $40 \times 40 \times 1$ \mathbf{k} -points with two shifts in the plane. The cut-off energy is taken 12 Ha, while for the smearing a temperature of 0.01 Ha has been

used with the Marzari cold smearing. These parameter are sufficient for a slab with $r_s = 2.5$ and a cell of planar dimensions of $3.618 \times 3.618 a_B$. In particular in the direction perpendicular to the surfaces only one \mathbf{k} -point has been chosen, because the dimension of the cell in this direction is much larger than the ones in the plane, and no dispersion is expected in the z direction thanks to the large vacuum layer. For the other dimensions the choice of the grid has been done having care of preserving density of \mathbf{k} -points in the Brillouin zone equal or higher than the one for which has been done a convergence test. For this reason the number of \mathbf{k} -points has been changed according to the dimension of the cell.

The first computations done were aimed at testing the effect of the spurious interactions between the periodic replicas of the slabs. We have done three calculations for a slab of $r_s = 2.5$ and a thickness $D = 30 a_B$ with three different thicknesses of vacuum between two successive slabs. The following results have been obtained:

thickness of vacuum (a_B)	E_{total} (Ha)
20	-0.2788376037
30	-0.2788379492
40	-0.2788379459

The digits reported are significant only till 10^{-8} which is the tolerance of exit from the self-consistence loop. From these values we conclude that already for a vacuum thickness of $30 a_B$ the total energy is essentially unaffected by the interaction between two different slabs. Thus for further computations we choose this thickness of vacuum. The interactions should be even smaller for smaller densities (larger r_s).

To determine the surface energy γ and the interaction between the two surfaces within the same slab we have run computations for different thicknesses D of the slab. These computations have also been done for different densities in order to study how γ changes with r_s . The computed energy was divided by the area A , and expanded according to eq. (5.1). Beside the linear bulk term and the constant surface term 2γ , the residual $E_{surf-surf}$ was found to exhibit damped oscillations (of period $2k_F$) as function of D (see sec. 5.1.2 and fig. 5.1-5.3, 5.7). These oscillations will be analyzed in detail in the next section. We chose thicknesses of the slabs for different r_s in order to sample correctly oscillations of different periodicity.

5.1.2 Fits of the curves

The total energy obtained from the DFT-LDA calculations can be interpolated with the following function:

$$\frac{E_{total}}{A} = \epsilon_p \rho D + b + c \frac{\cos(2k_F D + \theta)}{D^2} \quad (5.2)$$

For the different values of r_s we have obtained the following fitted parameters:

r_s	$b = 2\gamma$ $10^{-4} Ha/a_B^2$	c $10^{-3} Ha$	θ rad
2	-1.12099	10.4314	5.1447
2.3	-1.39933	8.17716	4.7302
2.5	1.15455	7.11283	4.4564
3	2.86472	5.01215	4.0203
3.5	2.62002	3.50425	3.6552
4	2.09271	3.03284	3.4224
4.5	1.61714	2.18936	3.1261

In figures 5.1 we represent the fitting functions (5.2) compared DFT-LDA energies; the horizontal dotted line correspond to twice the surface energy ($b = 2\gamma$)

The assumptions on the wavelength and the damping power of the oscillations has been tested with some fits computed allowing to vary these quantities as fitting parameters: they produced for these parameters values comparable with the assumed one. Only the damping power sometimes appears to deviate, in particular for $r_s = 2$ and 4.

The computed surface energy is found in good agreement with the values computed by Lang and Kohn [24] as illustrated in fig. 5.4. The discrepancies are mainly due to different choices of the exchange and correlation parameterization.

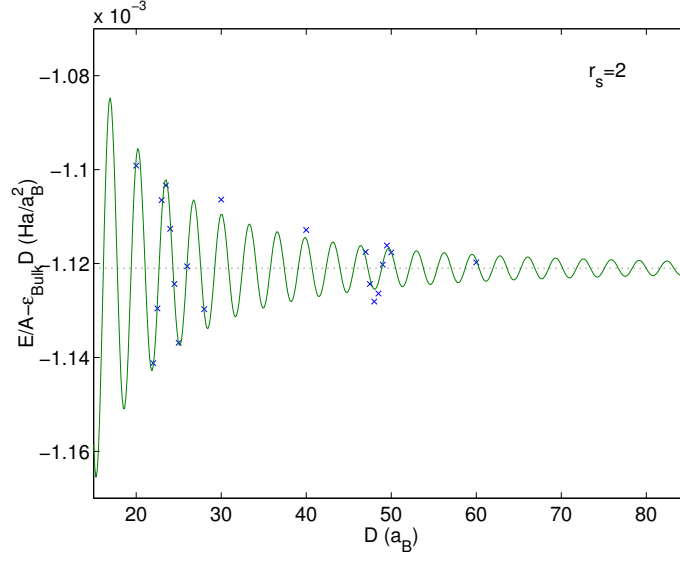


Figure 5.1: Comparison of the total energy per unit surface obtained by the DFT-LDA method with the best fit of these energies according to eq. (5.2). To all these energies the bulk contribution $\epsilon_p \rho D$ has been removed, so that the intercept at $D = 0$ (indicated by a dotted line) represents 2γ , and the oscillating term coincides with $\frac{E_{surf} - surf}{A}$ of eq. (5.1).

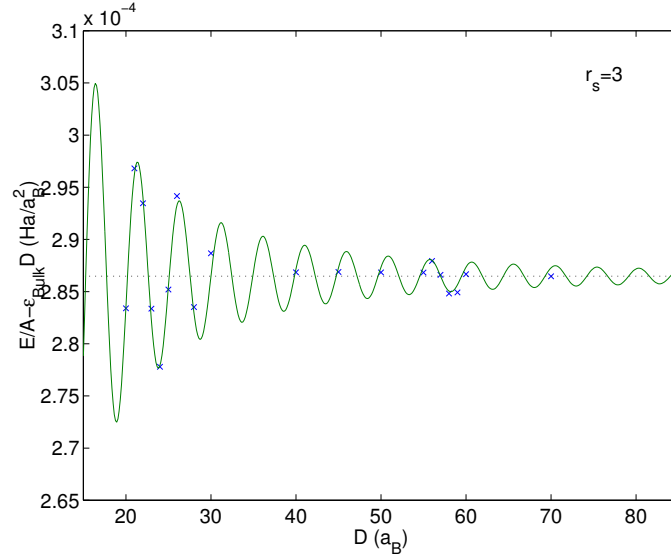
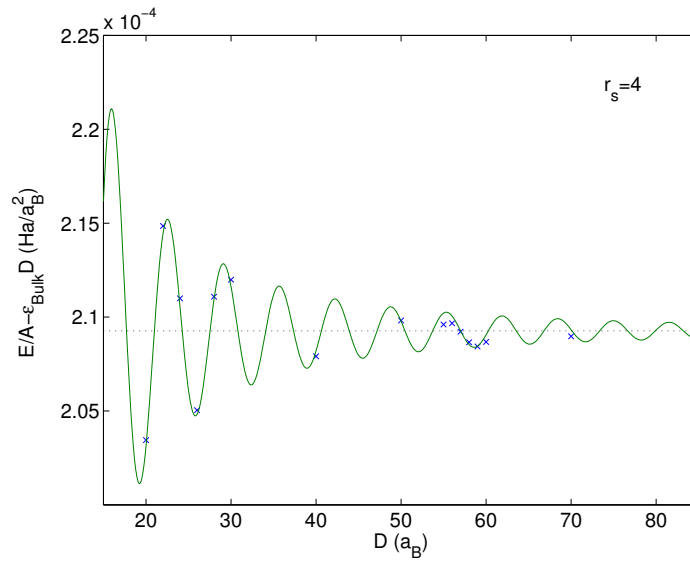
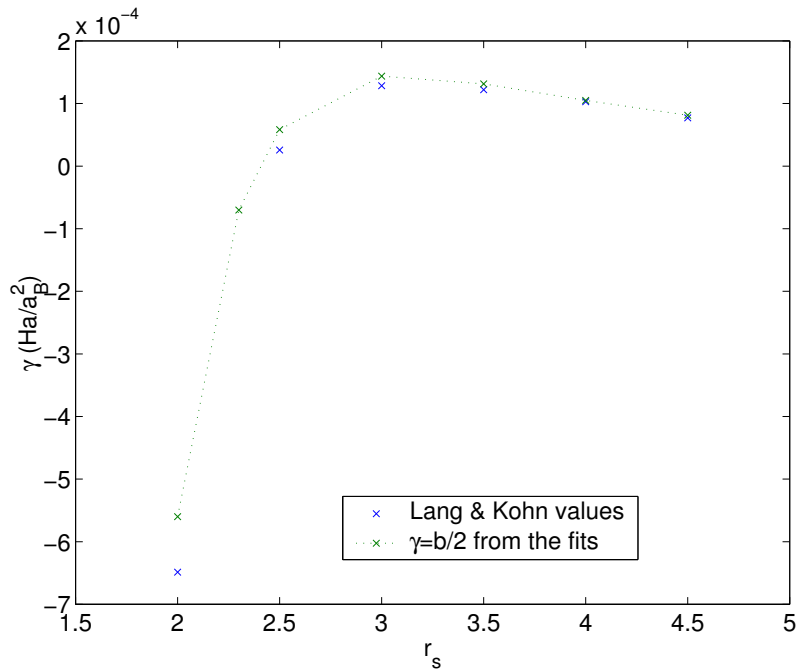


Figure 5.2: As fig. 5.1 with a different r_s .

Figure 5.3: As fig. 5.1 with a different r_s .Figure 5.4: Surface energy as function of the electron density represented by the parameter r_s .

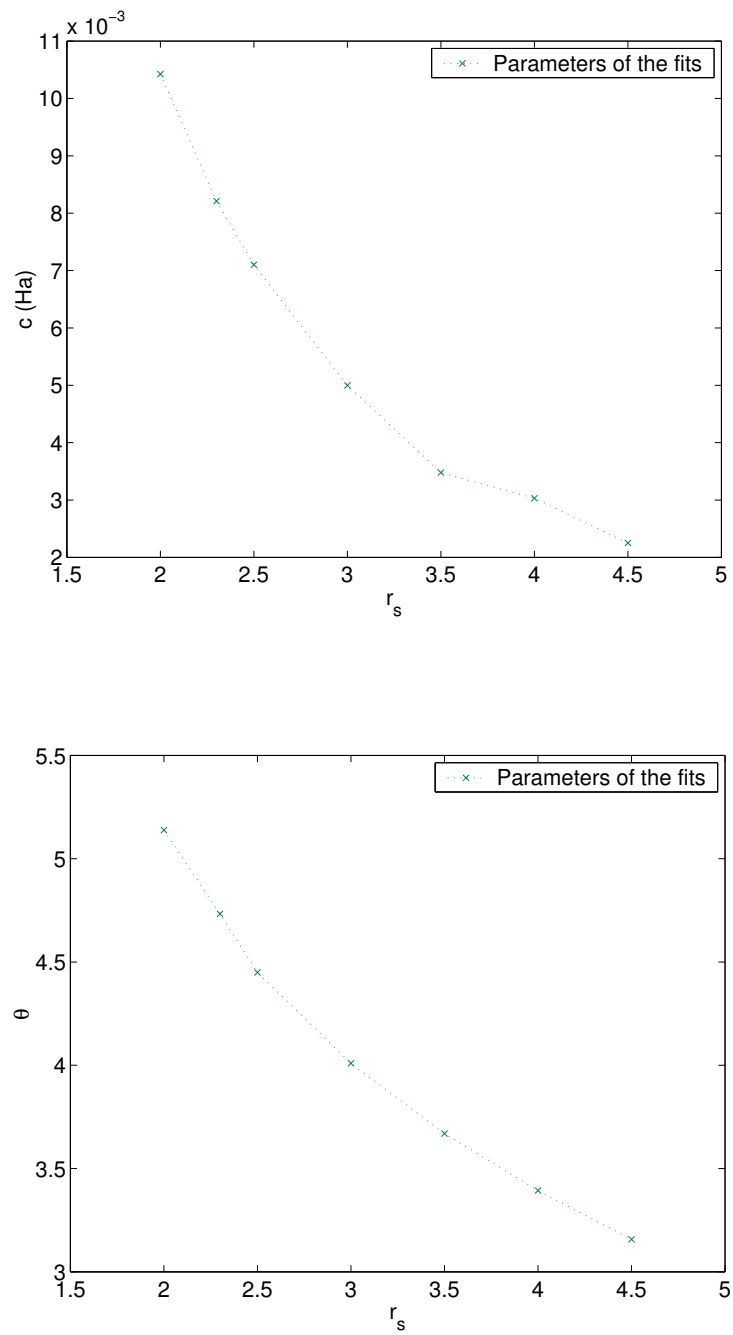


Figure 5.5: Amplitude and phase of oscillations.

5.1.3 The cusps

The function we use in this thesis to fit the oscillations of the QSE must be considered only a first phenomenological approximation of the real curve describing this effects. According to previous calculations [36], the total energy should show a sequence of cusps in correspondence of the minima of the oscillations. The stabilized jellium of ref. [36] is not the same as our model, but we expect to find qualitatively similar results here. However the finite \mathbf{k} -point sampling with the associated Fermi surface smearing does not permit to obtain these cusps since the smearing causes a smoothing of the total energy.

To illustrate in detail this point we perform a detailed study of the total energy as function of D along a single surface oscillation, for two different smearing temperatures (see fig. 5.6). In comparison we observe that for the lowest smearing temperature the minima becomes sharper emergenting that in the limit of null smearing temperature it would build up a cusps.

The distortion in the region of the maximum is probably due to the fact that the lower smearing temperature requires a finer mesh of \mathbf{k} -points since the mesh used (the same for both cases) may be too small for the smaller smearing, or it may be due to the fact that in that region the shift of some \mathbf{k} -points should be such that the occupations would be slightly different influencing the resulting total energy.

In fact the method used here is not the best solution to investigate the clean jellium surface with full invariance in two dimensions: the wavefunction dependence in these directions is better solved analytically and an *ad hoc* code to resolve a one dimensional problem could be used. We use a full three dimensional code with in mind the possibility to include surface adsorbates which would break the translational invariance in the planar directions.

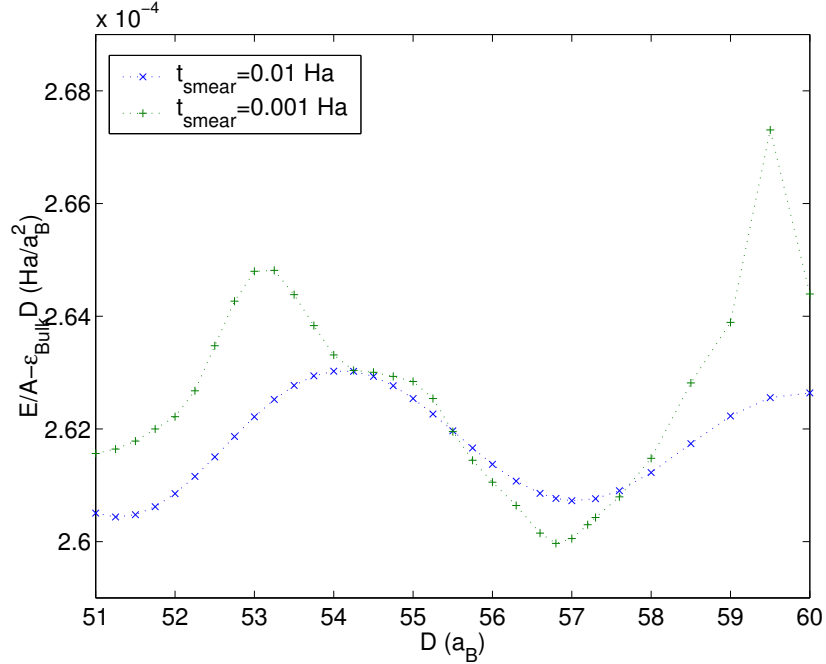
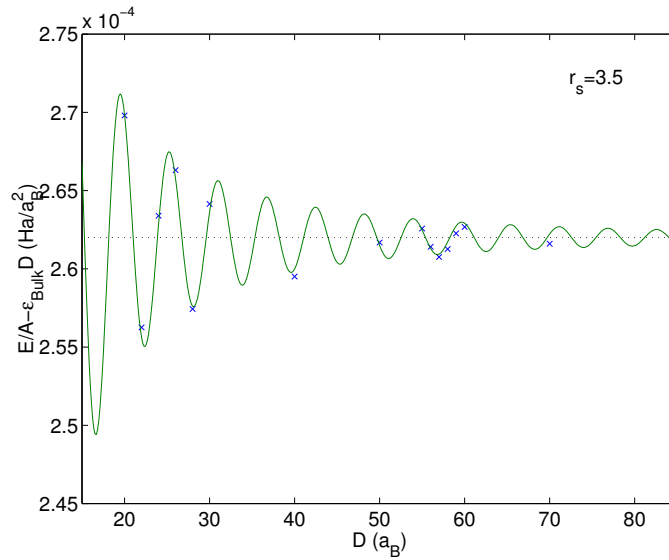


Figure 5.6: Total energy minus the bulk contribution for a jellium slab against the slab thickness, for two different smearing temperature ones, $r_s = 3.5$. The \mathbf{k} -point mesh is 30×30 with two shifts.

5.1.4 Analysis of the components of the total energy

In order to better describe the observed oscillations we have done a detailed analysis of the components of the total energy as in eq. (1.11) for $r_s = 3.5$. We then distinguish the kinetic term, the exchange and correlation one and the sum of the Hartree energy plus the contributions due to the background-background and electron-background interactions. Each of this terms per unit area shows the same behaviour as the total energy, with a bulk linear term, a constant surface term, plus the oscillatory contribution due to the interactions between the surfaces. We have therefore computed a fit in the same way as for the total energy (fig. 5.7). The following table reports the best fit parameters and fig. 5.8-5.10 represents the DFT-LDA values with the best fit to which the bulk contribution is subtracted like for the total energy.

	b $10^{-4}Ha/a_B^2$	c $10^{-3}Ha$	θ rad
E_{Total}/A	2.62002	3.50425	3.6552
K/A	3.89935	8.56727	5.0396
E_{XC}/A	5.54735	5.55007	2.3511
E_{Coul}/A	0.992707	1.94857	2.5914

Figure 5.7: Same as fig.5.1 for $r_s = 3.5$.

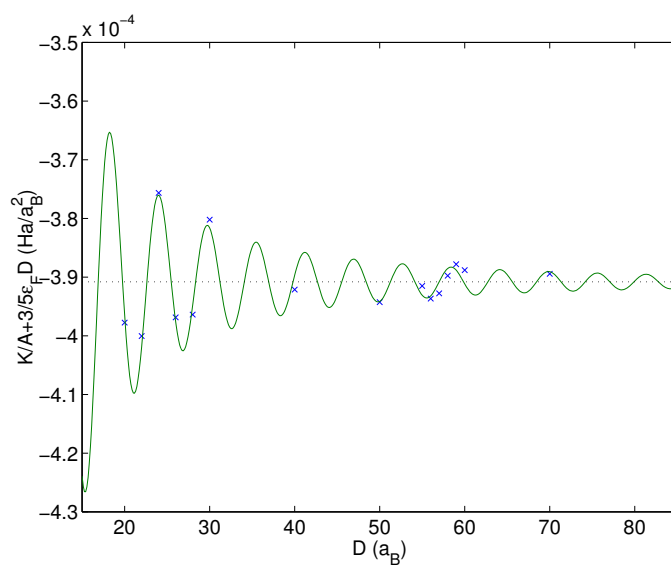


Figure 5.8: Fit of the single components of the total energy: the kinetic term.

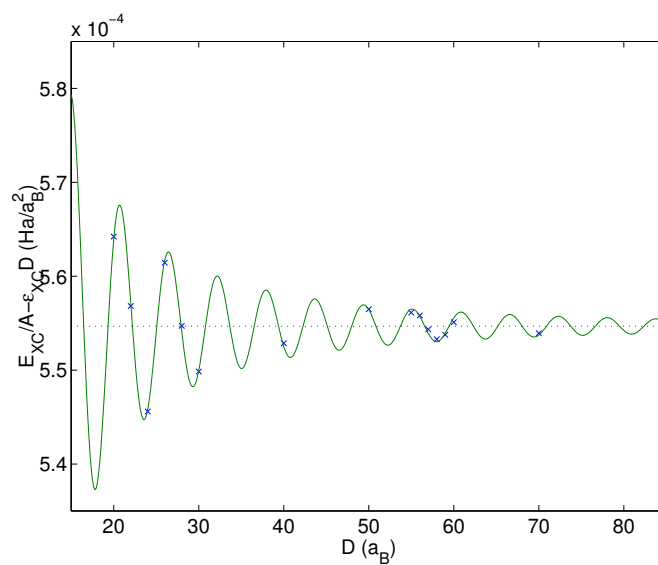


Figure 5.9: Fit of the single components of the total energy: the exchange and correlation term.

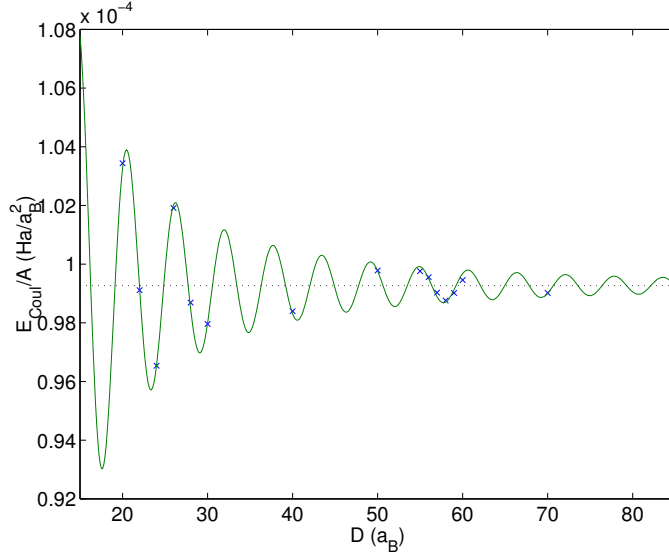


Figure 5.10: Fit of the single components of the total energy: the Coulombian term.

In fig. 5.11 we compare the fits of each term. Both the bulk term proportional to D and the surface constant contribution have been subtracted, in order to make possible a comparison between the amplitude and the phase of the oscillations that all three terms show. The Coulombic term has the oscillations of the least amplitude. Note the phase shift of the kinetic term with respect to the exchange and correlation and the Coulombic one, so that the resulting oscillations in the total energy are due to a nontrivial superposition of these oscillations. None of the terms can be neglected in the total energy.

Note that the total energy does not correspond exactly to the sum of the single components, as may be seen in fig. 5.12. This depends from the fact that the entropic term induced by the smearing must also be considered. To check that the smearing term does not affect radically the surface results for total energy we have run a computation with a smaller smearing temperature and after the same elaborations we found that there was no more that discrepancy (see fig. 5.12). This also indicates that, even though the total energy is well converged against the Fermi-surface thermal broadening, each individual term is not especially well converged.

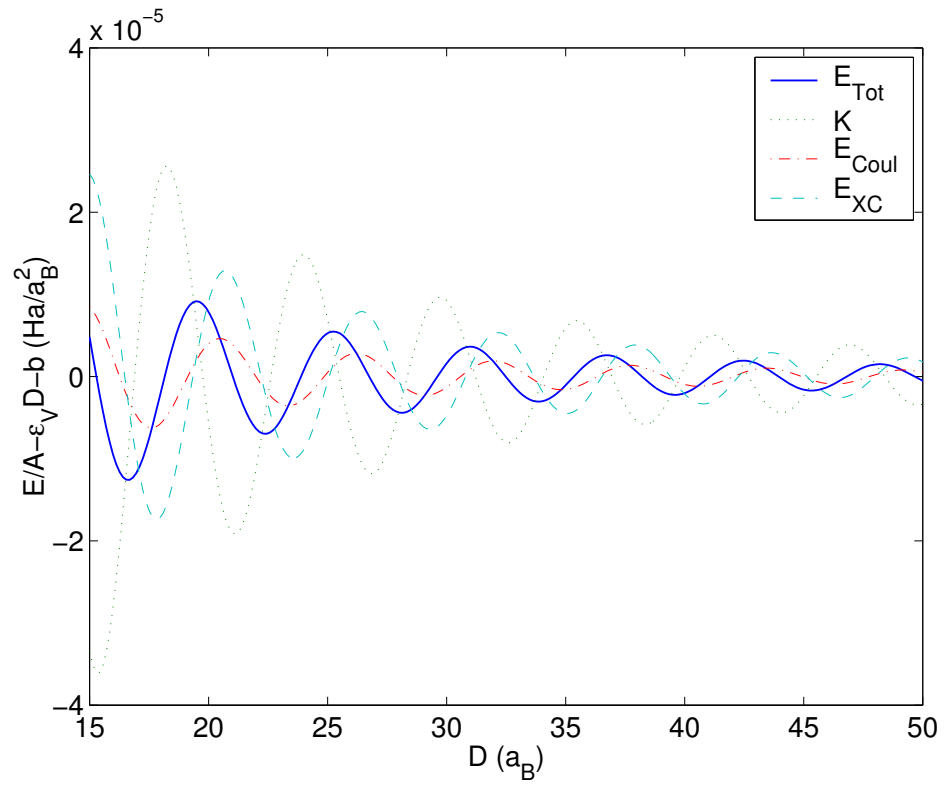


Figure 5.11: Fit curves for the different components of the total energy, to each curve has been subtracted the bulk contribution and the surface one (ϵ_V stands for the energy per unit volume of the plotted component).

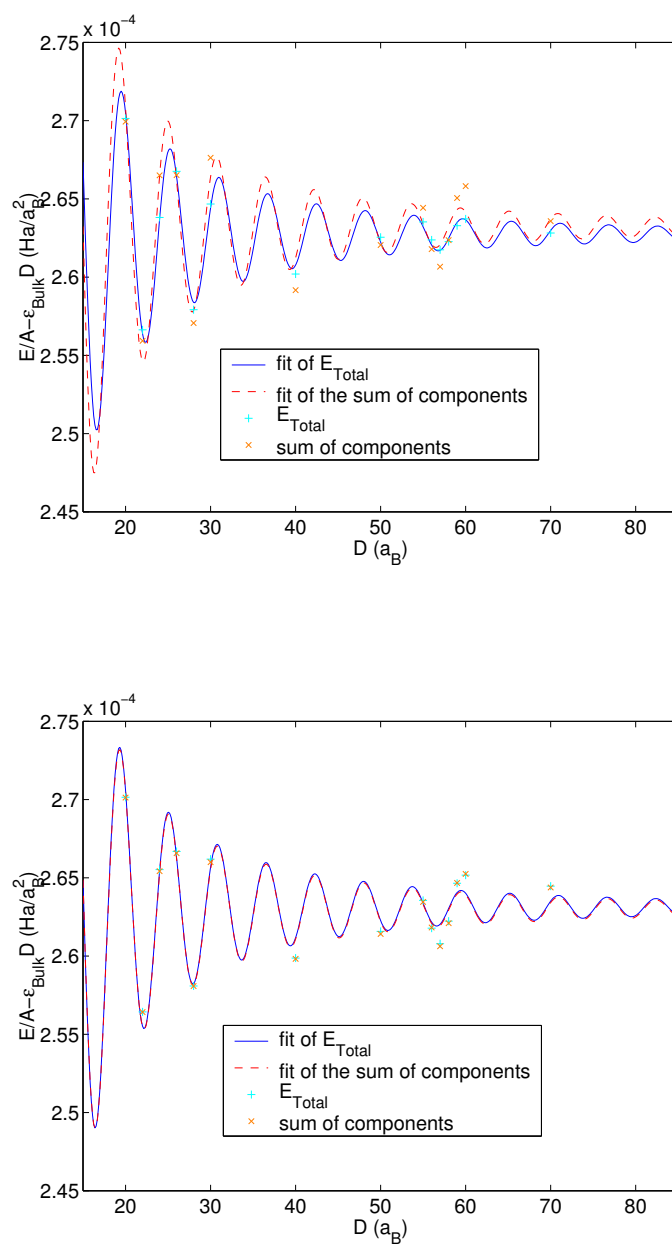


Figure 5.12: Comparison between the total energy and the sum of the components for a smearing temperature from the top of 0.01 Ha and of 0.001 Ha

5.2 The eigenfunctions

We expect that the reason of the energy oscillation is the oscillation in the surface dipole in analogy with what Shulte observed for the effective interaction and the work function [35]. For this reason we study the Kohn-Sham wavefunctions in particular along the direction perpendicular to the surfaces (since in the other directions they are plane waves) in order to analyze the different wavefunction spill-out that are the origin of the effects described by Shulte. For this calculation we choose a slab of thickness $30a_B$ with a vacuum of $30 a_B$, with $r_s = 3.5$. In fig. 5.13 a few low energy fully self-consistent Kohn-Sham wavefunction are represented along z . We represent only the real part since the imaginary one is practically zero. In addition the figure is restricted to a half of the vacuum region and of the slab thickness since they are either symmetric (as these in fig. 5.13) or antisymmetric. Note that the eigenfunctions, as expected, shows a larger and larger spill-out for higher quantum number i . Only the six lowest eigenfunctions are filled for the conditions of this calculations. This confirms that the vacuum chosen is wide enough since the less energetic wavefunctions vanishes before the half of the vacuum region, so that there is not superposition of the filled wavefunctions of neighboring slabs. Of course higher empty ones do not respect this condition, but are irrelevant for the interaction between two slabs in DFT-LDA.

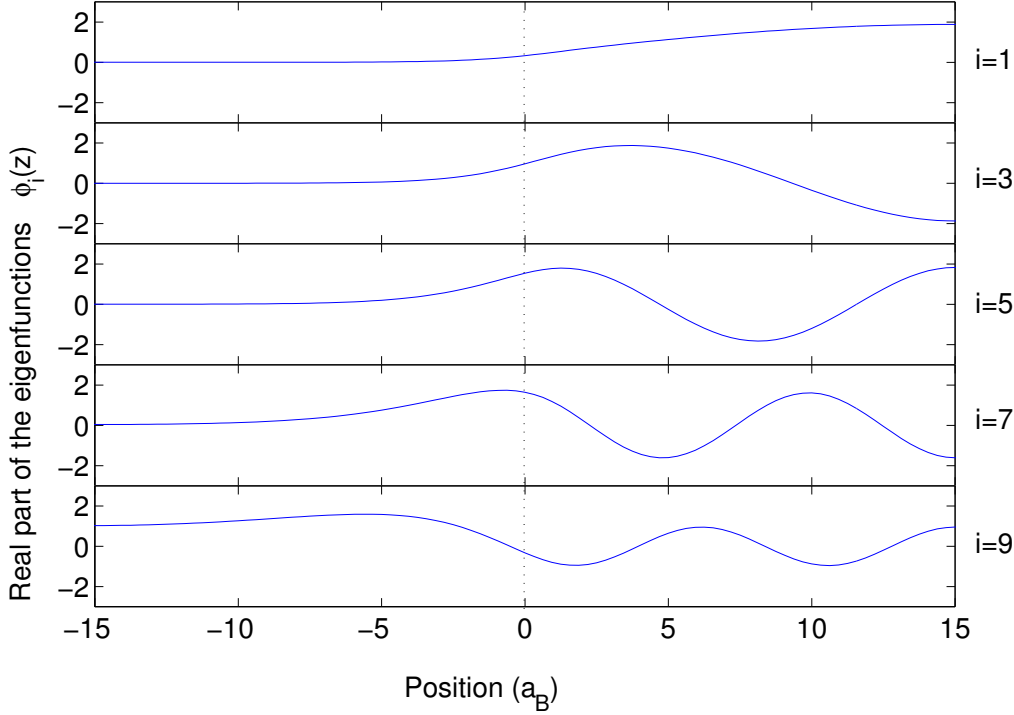


Figure 5.13: A few low energy wavefunctions for a jellium slab of $30 a_B$ with a vacuum of $30 a_B$ and $r_s = 3.5$ in the z direction. $z = -15$ is the center of the vacuum region, $z = 0$ marks the jellium slab and $z = 15$ is the center of the slab.

5.3 Study of the surface dipole

5.3.1 Interpolation of the dipole

In this section we test the role of the oscillation of the surface dipole for the total energy (and its components). In literature there are some works in which the authors give a description of the slab density with parameterized models, like in ref. [34]. In this We, too, are going to use a phenomenological model density in order to get informations on the effects due to the surface dipole. In order to study only the dipole effects (neglecting of interfering effects due to Friedel oscillations inside the slab) we use an interpolated density that only captures the correct surface dipole and does not oscillate inside the slab. As the actual DFT charge distribution decays exponentially in correspondence of the surface, we choose in this section a model charge density, that presents this behavior and tends asymptotically to the bulk density inside the slab. Imposing to the model density and to its derivate

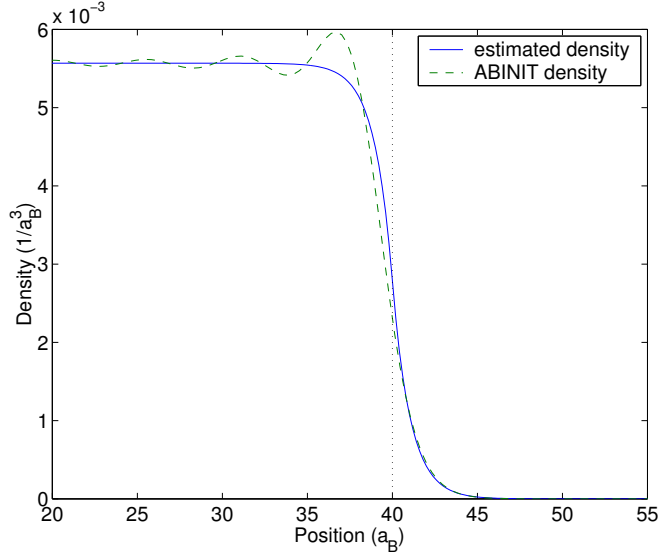


Figure 5.14: Comparison between the DFT-LDA electron density and the fit to its spill-out tail with the model density of eq. 5.3.

to be continue at the jellium surface and the condition of neutrality of the system, we get that the resulting density will be:

$$n(z) = \begin{cases} \frac{\rho}{2} e^{\beta z} & z \leq 0 \\ \rho - \frac{\rho}{2} e^{-\beta z} & 0 < z \leq \frac{D}{2} \\ \rho - \frac{\rho}{2} e^{\beta(z-D)} & \frac{D}{2} < z \leq D \\ \frac{\rho}{2} e^{-\beta(z-D)} & z > D \end{cases} \quad (5.3)$$

We neglect the derivate discontinuity in the middle of the slab, not eliminated by construction, since the density in that point is considered till at its asymptotic value and so almost equal to the bulk value in an interval around the center of the slab. The parameter β is than computed by a fit of the density obtained from the DFT-LDA computations. Since inside the slab there are the Friedel oscillation this fit has been computed only on the density outside. In fig. 5.14 we represent a typical example of such a fit. Note that outside the surface the fit is very good and the two curves are practically coincident, while the absence of the oscillations causes an over-estimation of the density at the jellium surface.

We repeat this fits for all the DFT-LDA densities for $r_s = 3.5$. We find that the parameter β oscillates as expected as a function of the slab thickness (see fig. 5.15). This oscillations infract measure the inverse surface spill-out of charge, thus the inverse surface dipole. The same has been observed for $r_s = 2.3$, value analyzed in order to get an indication on the r_s dependence

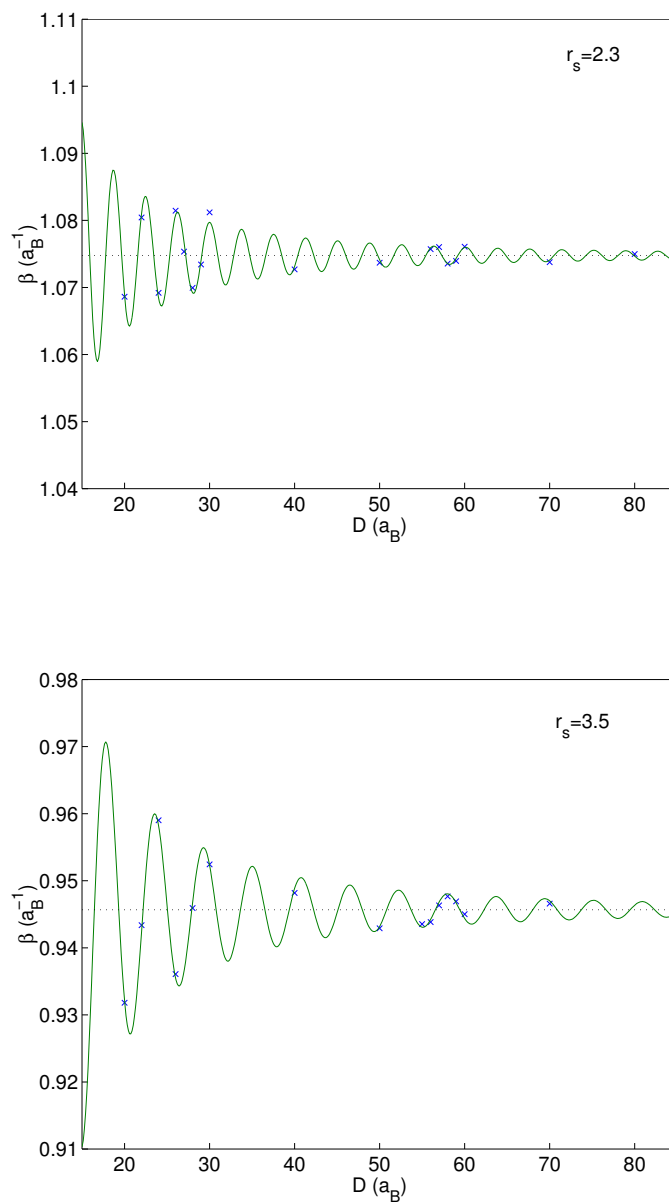


Figure 5.15: Fitted values of the parameter β as function of the slab thickness D (crosses). Best fit of the β values using $f(D)$, eq.(5.4) (solid line).

of the charge spill-out. The table below reports the values of the parameters of the fits for the D dependence of β ; the fitting function is the usual:

$$f(D) = b + c \frac{\cos(2k_F D + \theta)}{D^2}. \quad (5.4)$$

r_s	b a_B^{-1}	$1/\lambda_F b$	c a_B	θ rad
2.3	1.07399	0.12365	2.29981	-0.107321
3.5	0.945683	0.09228	7.96106	-0.766551

From this result we observe that the extension of the charge spill-out in correspondence to the surface related to the Fermi wave length is decreasing with respect to r_s (see ref [24]). Moreover we note that the value of the fitting parameter c increases with r_s . This is consistent with a decreasing amplitude of the oscillations as a function of r_s as we observed in sec. 5.1.2 (fig. 5.5).

5.3.2 Resulting energies

Based on the model density (5.3) we compute the total energy and its components. The exchange and correlation energy is:

$$\frac{E_{XC}[n(z)]}{A} = \int_{-\infty}^{+\infty} \epsilon_{XC}[n(z)]n(z)dz \quad (5.5)$$

where the integrations limits imply a single slab not periodically repeated and ϵ_{XC} is given from eq. (1.15).

In the Kohn-Sham formalism the kinetic term depends not just on the density of the system, but also on the wave functions of the auxiliary system. However, for the model calculations these are not available, so to compute this contribution we refers to Thomas-Fermi kinetic energy. The kinetic energy per unit of surface is:

$$\frac{K[n(z)]}{A} = \frac{3}{10}(3\pi^2)^{2/3} \int_{-\infty}^{+\infty} [n(z)]^{5/3} dz \quad (5.6)$$

In order to improve the accuracy we have attempted to compute the kinetics terms with the Thomas-Fermi functional plus the gradient corrections due to von Weizsäcker eq. (2.20). Pure Thomas-Fermi yields similar result.

The calculation of the Hartree term plus the interaction between the electrons with the background and the background with itself is more complex and will be explained in detail in appendix A. We report here only the result:

$$E_{Coul} = -\pi \int_{-\infty}^{\infty} dz \int_{-\infty}^{\infty} dz' n(z)n(z')|z - z'| - \pi\rho^2 \frac{D^3}{3} +$$

$$+2\pi\rho \left[\int_D^\infty dz' n(z') (2z'D - D^2) \int_0^D dz' n(z') \frac{z'^2}{2} \right] \quad (5.7)$$

The resulting components of the total energy are plotted in fig. 5.18, 5.16, 5.17. These results show that the oscillations gotten from this simplified model have comparable amplitude and phase to the corresponding DFT-LDA oscillations. We deduce that the dipole oscillations due to quantum finite-size effects is the most important cause of this oscillatory behavior in the energy. Likewise, the oscillations in the effective potential and in the work function computed for the first time by Shulte [35] have received a similar interpretation. Even though the model captures fairly well the oscillation amplitude and the phase, the surface contribution of the various terms, (the constant intercept) is incorrect by several percent, as expected for such a simple model. When the individual contribution are collected to obtain the total energy (fig. 5.19), the accord with the DFT-LDA calculations is not particularly good, as was for the single components. This is due to the strong cancellation of the oscillations of the individual term, which is not sufficiently accurate in this simple model.

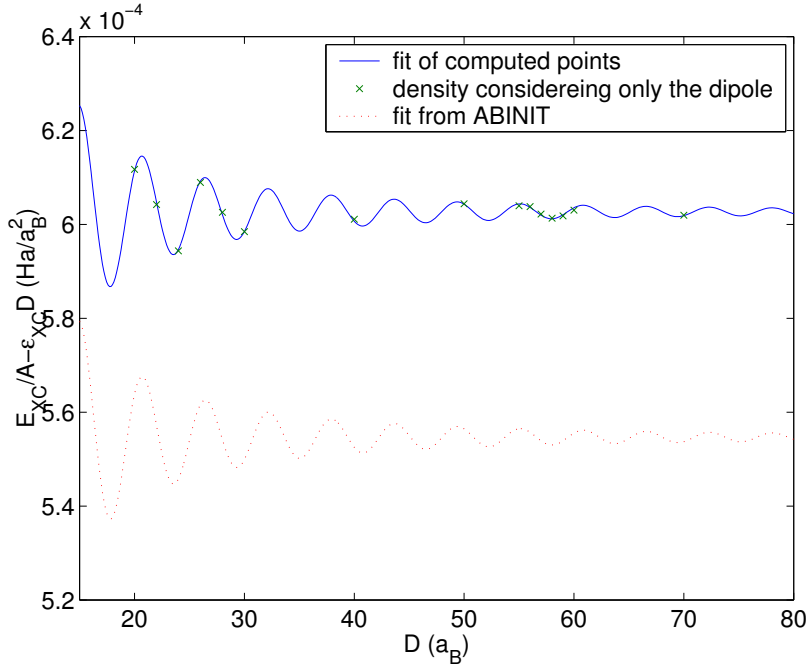


Figure 5.16: Exchange and correlation term.

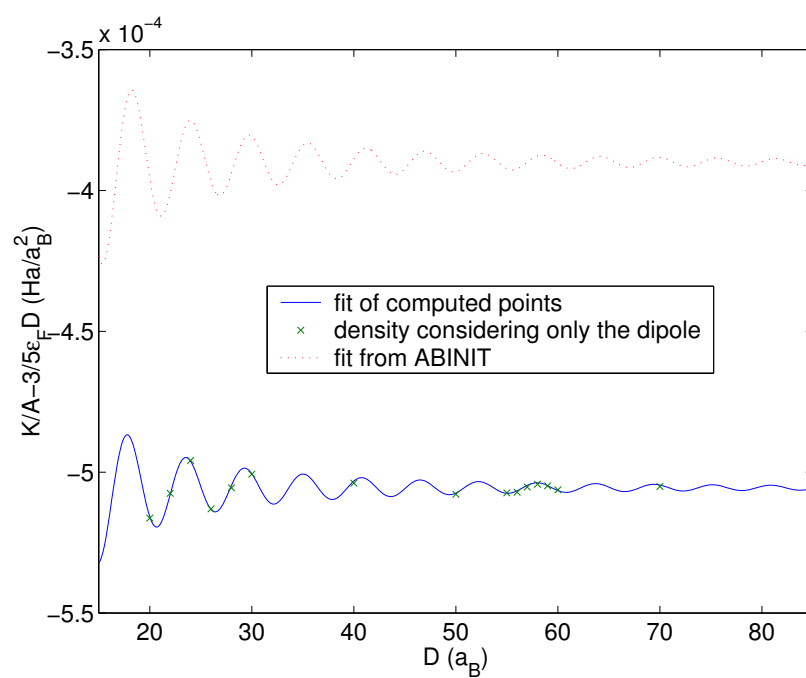


Figure 5.17: Kinetic term.

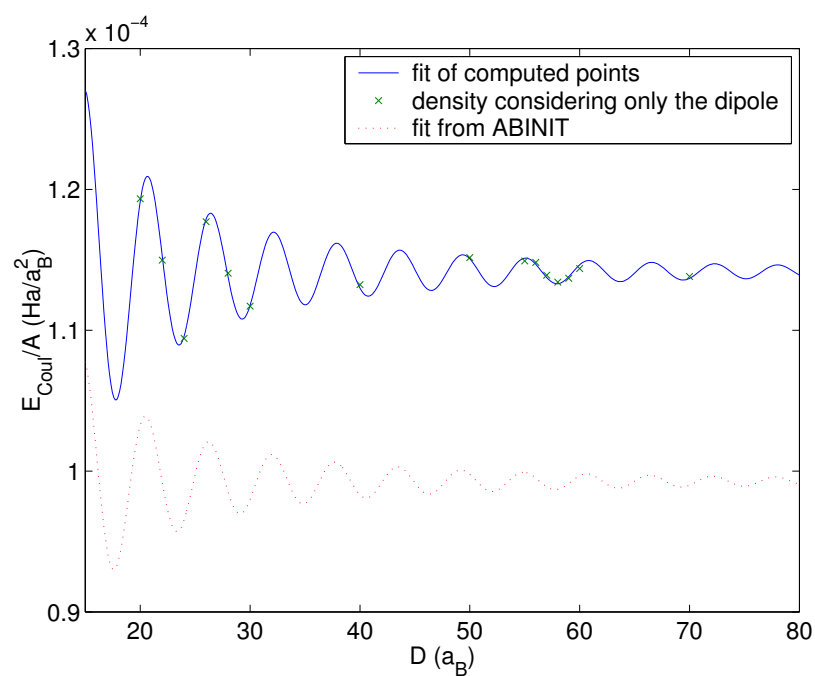


Figure 5.18: Coulombian term.

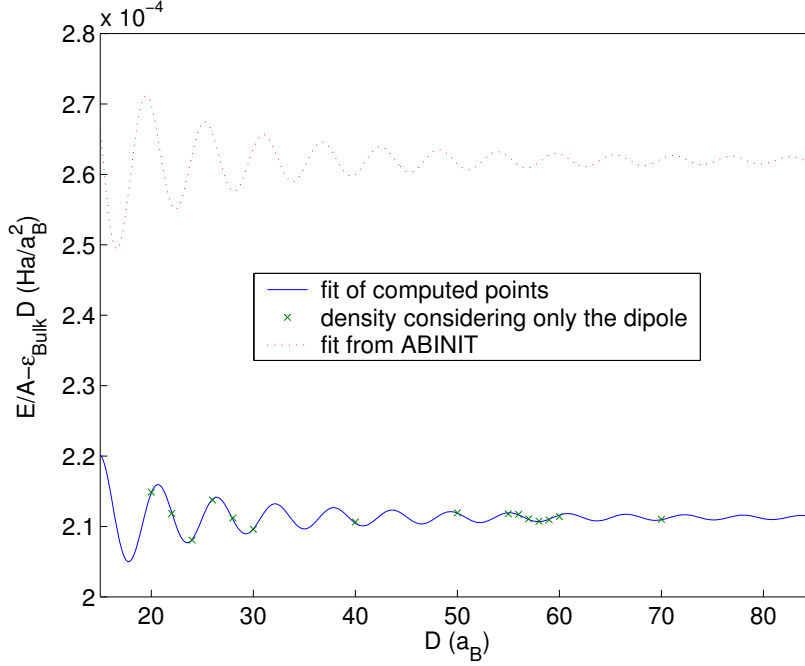


Figure 5.19: Total energy.

5.4 The "model density" method

What we described in the previous section is the most important reason for the oscillations in the total energy and in its components, while there may be, too, an effect due to the superposition of the charge density oscillations coming from the two surfaces.

5.4.1 The method

The idea of a simple model to check possible effects of the superposition of the different density oscillations consists in the computation of the single components of the total energy starting from their expressions as density functional, like what has been done with the surface dipole. The approximation done consists in a description of the density as composed of four terms as:

$$n(z) = \rho\theta(z)\theta(D - z) + \chi(z) + \chi(D - z) + \Delta\rho(z) \quad (5.8)$$

where the first term is the contribution of the homogeneous jellium, the second and the third are due to the behaviour induced by each surface as would be for a semi-infinite system and the last is the correction due to the interaction of the two surfaces which is neglected. Again we consider a single

slab placed between 0 and D . The expectation is that the non-linear terms in the functionals will give a contribution to the observed energy oscillations due to the interfering density oscillations.

The starting point for the computations is the density obtained through the simulations of a slab of $210 a_B$ of thickness so that one may suppose that the density in the first part of the thickness is not influenced by the effects due to the interactions between the two surfaces. From the density gotten from this computation has been selected the profile from a point in the middle of the vacuum region to a point placed at $45 a_B$ inside the slab, far enough from the center of the slab so that the effects of the other surface may be neglected. we than subtract the discontinuous background contribution to this density obtaining the function $\chi_0(z)$ (see fig. 5.20). The resulting slab density has been obtained from eq. (5.8) by summing the same density for the two surfaces plus the bulk contribution. Because the density of a single surface continues beyond the middle of the slab it can produce the desired effects of interference of the two densities in this region. However the oscillation continues undamped in the region of vacuum beyond the other surface. For this reason we need to damp the density in that region. To do this the density for a single surface $\chi_0(z)$ is multiplied by a function $f(z) = \frac{1}{\exp(\frac{z-z_0}{t})+1}$. In particular z_0 has been chosen at a fixed distance from the other surface $d = D - z_0$ where D is the slab thickness. Accordingly one can only produce charge densities almost up to $45 a_B + d + \frac{t}{2}$ and not smaller than $2d + t$.

For the computation of the contribute to the total energy we used the same functionals used for the study of the surface dipole (see sec. 5.3).

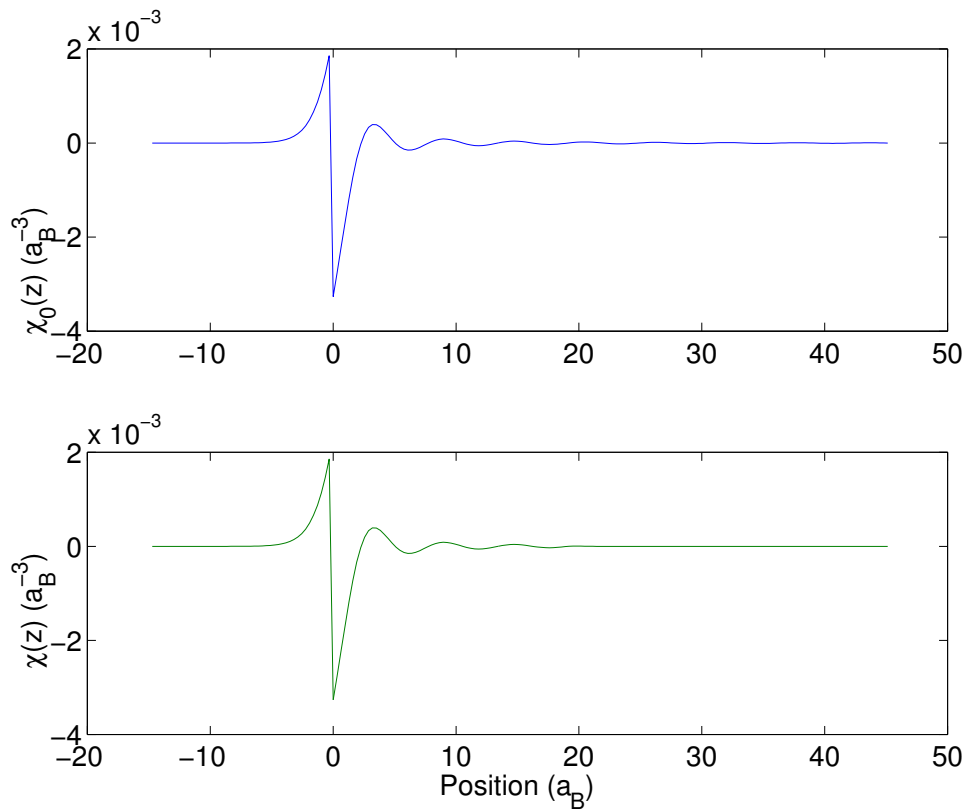


Figure 5.20: Contribute to the density due to a single surface $\chi_0(z)$ upper panel. Lower panel the density with the cut-off used for the calculations: for a slab of $20 a_B$ $d=0.5$ and $t=0.5$.

5.4.2 Study of the resulting energies as function of the damping parameters

We start this analysis from the exchange and correlation term since it is computed with the same functional eq. (5.5) as in the DFT-LDA, thus the results obtained with our code should be very similar to the ones gotten from ABINIT. We have checked the effect of the damping parameters $d = D - z_0$ and t . In figure 5.21 are plotted $\frac{E_{xc}}{A}$ oscillatory part computed with the model density (5.8) and compared to that fitted on the DFT-LDA results: to each term the bulk contribute to the energy has been subtracted. Notice that the surface exchange and correlation energy are substantially the same since the asymptotical value of the oscillations is the same. The oscillations in this component of the energy are strongly dependent from the damping parameters. In particular it is possible to notice how the phase of the oscillations is strongly influenced by the position of the damping point, and their amplitude from its width. A discrete accord occurs for position of the damping near the surface of the slab and a rapid decay.

We then compute the kinetic term. The computation is done with the Thomas-Fermi with the gradient corrections. Figure 5.22 represents the results from the computation of the kinetic energy. Note that the behaviour of the oscillations as function of the damping parameters is the same as in the exchange and correlation term, but the amplitude is by far underestimated. Also the surface term is different as the functional is different.

The last term is due to the Coulomb interaction between the two density of charge for which are valid the same consideration done for the other terms and is reported in fig. 5.23. The resulting surface contribution are not quite the same, as the surface dipole is incorrect anyway. Figure 5.24 shows the comparison of the total energy in the simplified model with that of the DFT-LDA, and shows very poor accord: in particular the oscillatory amplitude is much smaller in the model.

The fact that this model depends radically on the cut-off at the opposite surface points a large surface contribution, as confirmed by the calculation in the previous section. In fact, the present calculation estimate that the effect of the non-linearity of the functionals and consequent interference of the Friedel oscillation coming from the opposite surface accounts for at most 10% of the oscillations in the total energy.

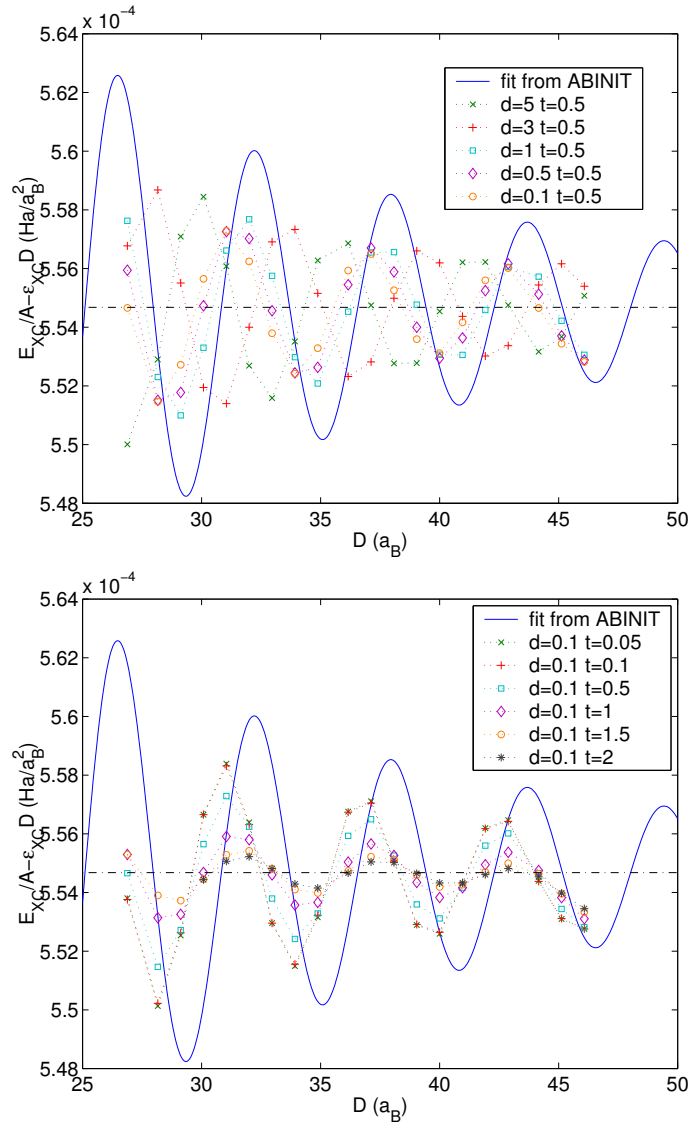


Figure 5.21: Study of the dependence of the exchange and correlation energy within the "model density" method with respect to the damping position d and width t .

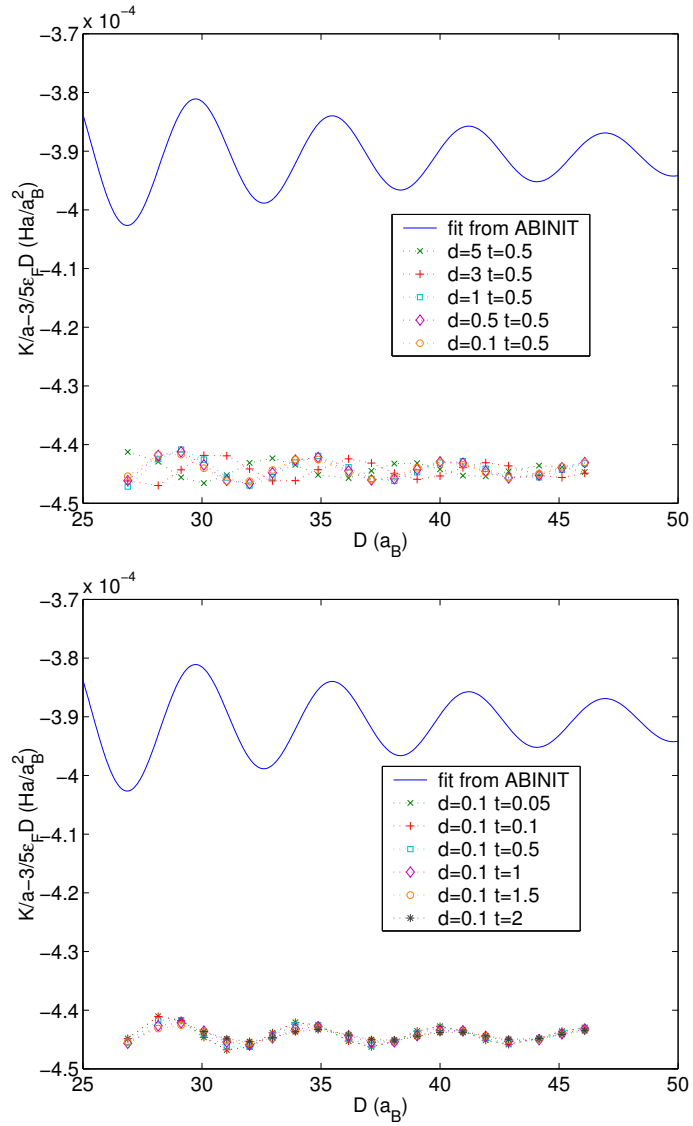


Figure 5.22: Study of the dependence of the kinetic energy within the "model density" method with respect to the damping position d and width t .

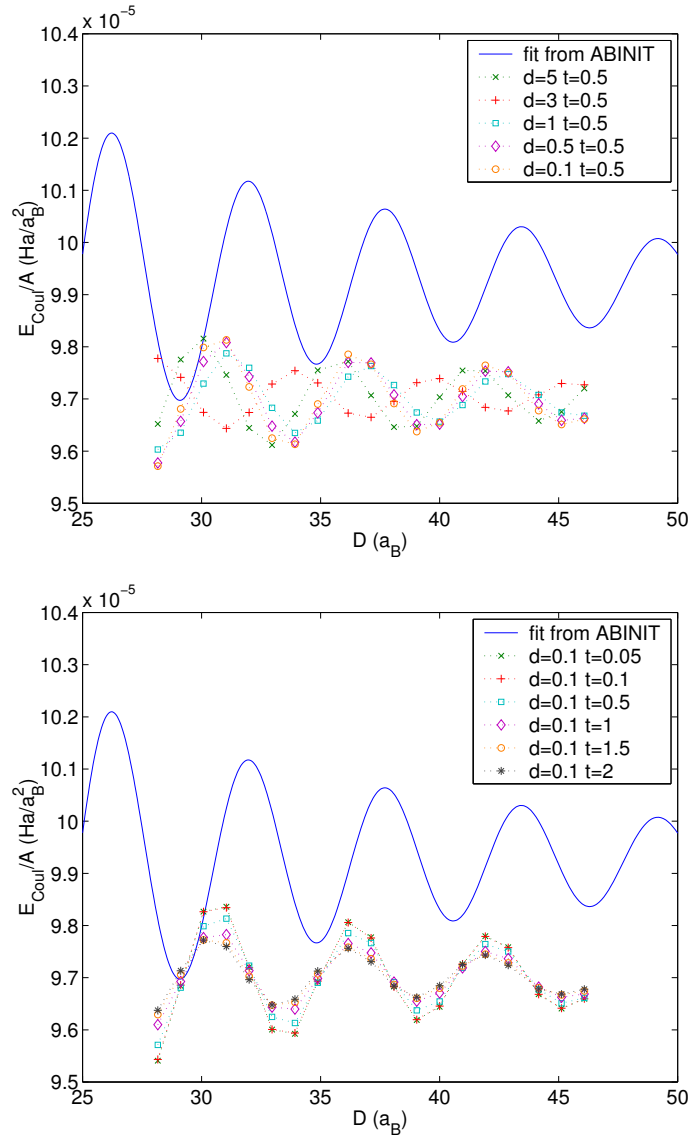


Figure 5.23: Study of the dependence of the Coulombian energy within the "model density" method with respect to the damping position d and width t .

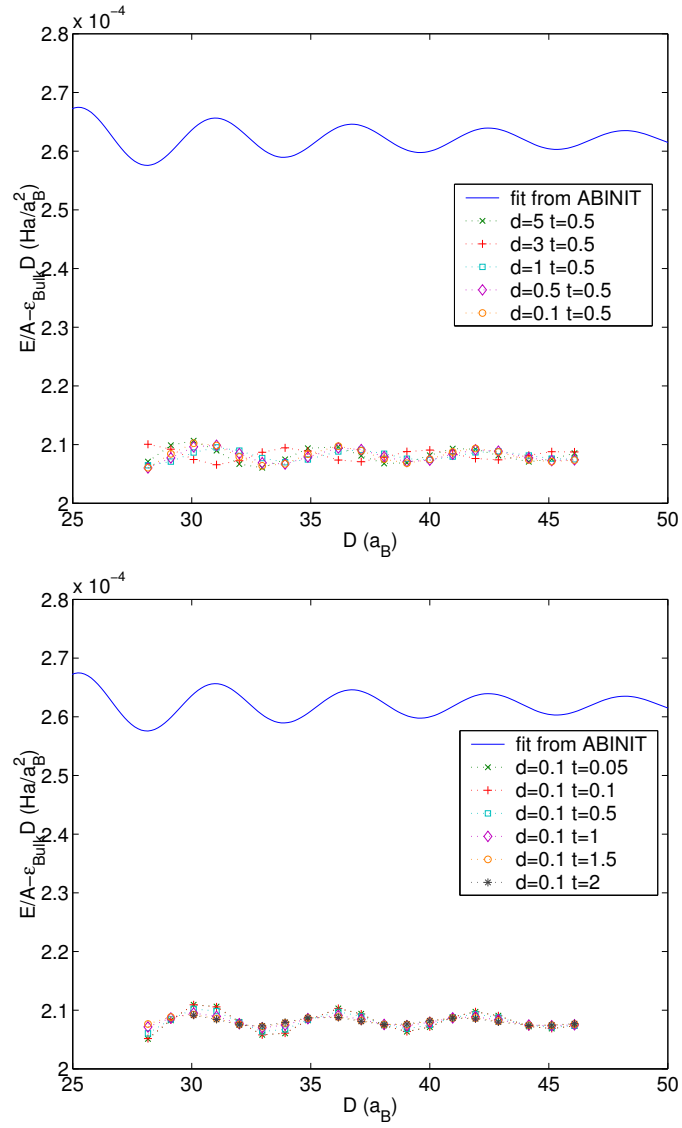


Figure 5.24: Study of the dependence of the total energy within the "model density" method with respect to the damping position d and width t .

Chapter 6

LDA and GW band structure

6.1 Procedure in a GW computation

Rather than starting from free-electron Green function as in section 1.4 and 1.5, the starting point for a GW calculation in a perturbative approach can be chosen to be the Hartree wavefunctions and eigenvalues. Alternatively, one can start from the Kohn-Sham orbitals and eigenvalues, if the perturbation is chosen as $\Sigma - V_{XC}$. The "non-interacting" Green function is then defined as:

$$G_{DFT}(\mathbf{x}, \mathbf{x}', \omega) = 2 \sum_i \frac{\phi_i(\mathbf{x}) \phi_i^*(\mathbf{x}')}{\omega - \epsilon_i + i\eta \text{sign}(|\mathbf{k}| - k_F)}, \quad (6.1)$$

where the index i stands for the set (n, \mathbf{k}) , the factor 2 comes from the spin summation, ϵ_i are the Kohn-Sham eigenvalues and $i\eta \text{sign}(|\mathbf{k}| - k_F)$ is chosen for the time ordered Green function. For the corresponding interacting function, the Dyson equation becomes:

$$G = G_{DFT} + G_{DFT} [\Sigma - V_{XC}] G, \quad (6.2)$$

where convolutions are implied and the self-energy is defined by the generalization of eq. (1.18). In brief the steps necessary to perform a GW computation are the following [4]:

- A self-consistent DFT simulation in order to produce the DFT Green function through eq. (6.1).
- From G_{DFT} the polarization is computed by means of the random phase approximation (RPA).
- The inverse dielectric response is computed ($\epsilon^{-1} = (1 - v\Pi)^{-1}$).

- ϵ^{-1} is used to generate the effective interaction $W_{RPA} = \epsilon^{-1}v$.
- The self energy appearing in eq. (6.2) is now generated as $\Sigma = iG_{DFT}W_{RPA}$.

At this point two different choices are possible. One is to update the Green function using eq. (6.2) and to repeat the procedure described in order to generate a self-consistent solution of Hedin equations. This kind of approach is used to compute properties like the total energy of a system using the Green function, but has well known difficulties [20], [33]. To compute the quasiparticles properties the self-consistency is avoided, and the first iteration is sufficient. Indeed computations for the homogeneous electron gas have shown that the spectral properties are better deduced by a single-iteration rather than by a self-consistent calculation [20]. This is the procedure used for the calculation of the present thesis.

Since the quasiparticle equation is similar to the Kohn-Sham equation, with the difference that the exchange and correlation potential is substituted with the self energy, the quasiparticle energy is conveniently computed by the first-order perturbation theory in $\Sigma - V_{XC}$. For this reason, the corrected energies are:

$$E_i = \epsilon_i + \langle \phi_i | \Sigma(E_i) - V_{XC} | \phi_i \rangle \quad (6.3)$$

where ϕ_i are the Kohn-Sham eigenfunctions and ϵ_i their eigenvalues. Since at this point E_i on the right side is not known, one substitutes to $\Sigma(E_i)$ its Taylor expansion at the first order in $E_i - \epsilon_i$. So the relation used to compute the GW correction is

$$E_i - \epsilon_i = \frac{\langle \Sigma(\epsilon_i) \rangle - \langle V_{XC} \rangle}{1 - \left\langle \frac{\partial \Sigma(\omega)}{\partial \omega} \Big|_{\omega=\epsilon_i} \right\rangle} = Z_i (\langle \Sigma(\epsilon_i) \rangle - \langle V_{XC} \rangle), \quad (6.4)$$

which defines implicitly the renormalization functions Z_i . At this point the problem is to compute the Green function from eq. (6.1) and the screened interaction W . Using the lattice periodicity and substituting the integration over the Brillouin zone with a finite sum, this can be written as:

$$W(\mathbf{x}, \mathbf{x}', \omega) = \frac{1}{V} \sum_{\mathbf{q}, \mathbf{G}, \mathbf{G}'} e^{i(\mathbf{q}+\mathbf{G})\cdot\mathbf{x}} \epsilon_{\mathbf{G}, \mathbf{G}'}^{-1}(\mathbf{q}, \omega) \frac{4\pi}{(\mathbf{q} + \mathbf{G}')^2} e^{i(\mathbf{q}+\mathbf{G}')\cdot\mathbf{x}'} \quad (6.5)$$

In order to simplify the numerical computations one redefines the dielectric matrix in order to get a symmetrized one for $\mathbf{G} \leftrightarrow \mathbf{G}'$ so that the effective interaction becomes

$$W_{\mathbf{G}, \mathbf{G}'}(\mathbf{q}, \omega) = \tilde{\epsilon}_{\mathbf{G}, \mathbf{G}'}^{-1}(\mathbf{q}, \omega) \frac{4\pi}{|\mathbf{q} + \mathbf{G}| |\mathbf{q} + \mathbf{G}'|}, \quad (6.6)$$

where $\tilde{\epsilon}_{\mathbf{G},\mathbf{G}'}^{-1}(\mathbf{q}, \omega) = \epsilon_{\mathbf{G},\mathbf{G}'}^{-1}(\mathbf{q}, \omega) \frac{|\mathbf{q}+\mathbf{G}'|}{|\mathbf{q}+\mathbf{G}|}$. Adopting the plasmon pole approximation (PPA) it is possible to parameterize the ω dependence of this matrix [21]. This is based on the fact that the imaginary part of the dielectric function is usually a peaked function of ω . For this reason it is parameterized as:

$$\tilde{\epsilon}_{\mathbf{G},\mathbf{G}'}^{-1}(\mathbf{q}, \omega) = \delta_{\mathbf{G},\mathbf{G}'} + \frac{\Omega_{\mathbf{G},\mathbf{G}'}^2(\mathbf{q})}{\omega^2 - \tilde{\omega}_{\mathbf{G},\mathbf{G}'}^2(\mathbf{q})}, \quad (6.7)$$

in term of the two parameters Ω and $\tilde{\omega}$ that are undetermined. The authors of ref. [21] choose to determine Ω and $\tilde{\omega}$ by the application of the sum rules for the dielectric matrix. The ABINIT implementation instead the parameters are determined by fitting numerical values of ϵ at $\omega = 0$ and at one point along the imaginary axis. Indeed if ω is purely imaginary one gets that the imaginary part of the inverse dielectric matrix is identically zero, while the real one is $1 + \frac{\Omega^2}{-\omega^2 - \tilde{\omega}^2}$; so from the knowledge of the dielectric matrix (from the RPA computation) for two values one can determine the parameters.

Now one can compute the self energy matrix element, that for simplicity is decomposed into two terms: one due to the mere exchange and another due to the correlation. The first term is derived from the constant part in the dielectric matrix. From the computation of the exchange self energy matrix elements we get:

$$\langle \phi_i | \Sigma_X | \phi_i \rangle = -\frac{4\pi}{V} \sum_{j, \mathbf{G}, \mathbf{q}} f_j \frac{1}{|\mathbf{q} + \mathbf{G}|^2} \langle \phi_i | e^{i(\mathbf{q}+\mathbf{G})\cdot\mathbf{r}} | \phi_j \rangle \langle \phi_j | e^{-i(\mathbf{q}+\mathbf{G})\cdot\mathbf{r}} | \phi_i \rangle, \quad (6.8)$$

where the matrix element vanishes unless $\mathbf{q} - \mathbf{k}_i + \mathbf{k}_j$ corresponds to a reciprocal lattice vector and f_i are the orbital occupation numbers. In the same way from the second addend in the dielectric matrix one gets the correlation contribution to the self energy whose matrix element are:

$$\langle \phi_i | \Sigma_C | \phi_i \rangle = \frac{2\pi}{V} \sum_{j, \mathbf{G}, \mathbf{G}', \mathbf{q}} \frac{1}{|\mathbf{q} + \mathbf{G}| |\mathbf{q} + \mathbf{G}'|} \langle \phi_i | e^{i(\mathbf{q}+\mathbf{G})\cdot\mathbf{r}} | \phi_j \rangle \langle \phi_j | e^{-i(\mathbf{q}+\mathbf{G}')\cdot\mathbf{r}} | \phi_i \rangle \cdot \left\{ \frac{\Omega_{\mathbf{G},\mathbf{G}'}^2(\mathbf{q})}{\tilde{\omega}_{\mathbf{G},\mathbf{G}'}(\mathbf{q})[\omega - \tilde{\omega}_{\mathbf{G},\mathbf{G}'}(\mathbf{q}) - \epsilon_j]} \frac{-2\Omega_{\mathbf{G},\mathbf{G}'}^2(\mathbf{q})}{(\omega - \epsilon_j)^2 - \omega^2 - \tilde{\omega}_{\mathbf{G},\mathbf{G}'}^2(\mathbf{q})} f_j \right\} \quad (6.9)$$

At this point eq. 6.4 require to compute also the self energy derivative with respect to ω : only the correlation term contributes, since the exchange one does not depend on frequency. Putting everything together, we compute the GW correction to the Kohn-Sham eigenvalues by means of eq. 6.4.

6.2 The Kohn-Sham band structure of the slab

Before analyzing the effect of the corrections of the GW approximation on the band structure, in this section we present a short description of the Kohn-Sham band structure of the jellium slab, in order to give an interpretation of the dispersion curves. The band structure is deduced in the DFT formalism, that give only a first approximation of the dispersion curves. They has been computed from a converged self-consistent calculation, whose results are the starting point for the computation of the energy at a hight number of \mathbf{k} -points in the more relevant directions in the Brillouin zone. We stress that the Kohn-Sham eigenvalues have not a direct interpretation as single-particle energies, since in this theory there is not a theorem like the Koopman one. However in the perturbative scheme illustrated before, the Kohn-Sham eigenvalues can be considered as zero-order quasiparticle energies, as in the customary use to take them as basic reference mean-field bands.

A homogeneous electron gas [3] presents a parabolic dispersion relation ($\epsilon_{\mathbf{k}} = \frac{|\mathbf{k}|^2}{2}$). When one studies this system by introducing an artificial periodicity, the parabolic bands fold inside the corresponding Brillouin zone. In the slab geometry the dispersion relation is exactly parabolic in the two directions parallel to the surface where translational invariance is preserved.

In the direction perpendicular to the surfaces we observe a sequence of discrete Kohn-Sham eigenvalues (see sec. 2.3.3). The band structure is then constituted by a sequence of parabolas as functions of \mathbf{k}_{\parallel} , shifted by the eigenvalues in the direction perpendicular to the surface. These parabolas are increasingly separated, with energies that grow almost with the square of the number of the band. This relation is similar to the relation of the eigenvalues of a particle moving in a square potential. This behaviour holds approximatively only for the low bands, until the energy gets close to the vacuum threshold, when it then ceases to apply and irregularly spaced levels are found.

Figure 6.2 represents the DFT-LDA bands computed by means of the ABINIT code. The dispersion in the surface Brillouin zone is reported along the path shown in fig. 6.1. The band energy at Γ represents the Kohn-Sham eigenvalue in the perpendicular direction. In the reported energy no band fold reach back the Γ point.

Bands are twice degenerate along the K-J direction, due to band folding in the fictitious Brillouin zone.

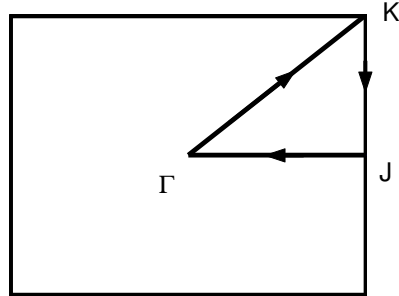


Figure 6.1: Schematic representation of the first Brillouin zone in the plane parallel to the surfaces, with the path used to describe the quasiparticle dispersion.

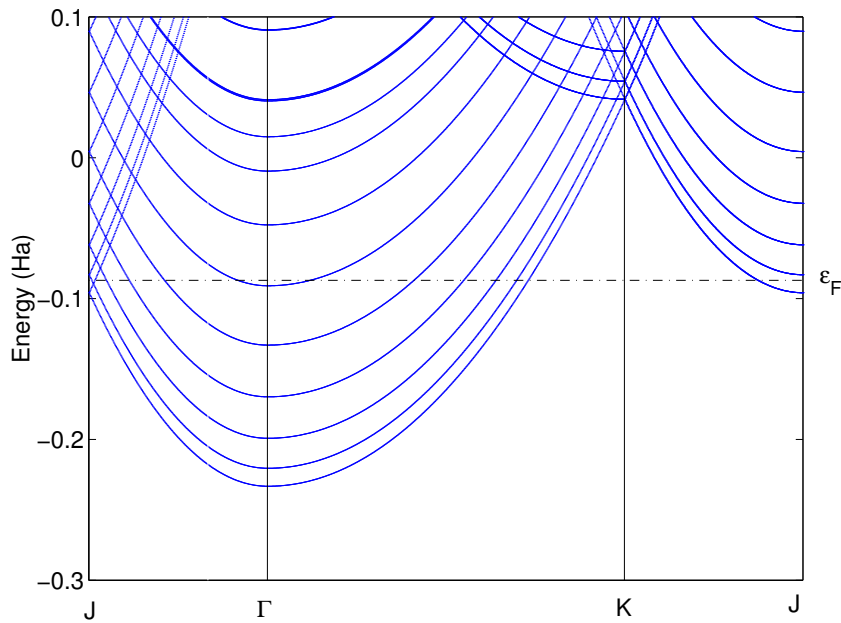


Figure 6.2: Band structure for a $30 a_B$ thick jellium slab (with $30 a_B$ of vacuum separating adjacent slabs), $r_s = 3.5$ and a fictitious (square) lattice in the plane directions parallel to the surfaces with lattice constant of $5.993 a_B$.

6.3 The surface LDOS and the resonance states

The DFT-LDA is more suitable where the density of the system under study varies slowly. This condition is not respected in the correspondence of a surface. Indeed LDA reveals itself inadequate in describing the effective potential at significant distance from the surface, since it produces an exponential behaviour rather than a power law. Connected with these difficulties is the problem of an inadequate description of the local density of state in the vicinity of the surface. The LDOS is defined as:

$$LDOS(E, \mathbf{x}) = \sum_i \delta(E - \epsilon_i) |\phi_i(\mathbf{x})|^2 \quad (6.10)$$

In a metal, without an energy gap, one should observe the resonances of surface states, but the DFT-LDA does not produce them, due to the incorrect behavior of the surface potential. This problem should be cured by the GW approximation. This approximation allows a correct description of the surface potential and therefore of the image resonances. In ref. [13] the authors performed some computations of the LDOS in correspondence of a jellium surface; in particular comparing of the results from the GW LDOS and that of the LDA, they found a surface resonance in correspondence of an energy of $\frac{1}{32}$ Ha under the vacuum energy (see fig. 6.3), as expected for a Coulomb surface resonant state.

6.4 The quasiparticle corrections

6.4.1 Procedure of computation

The GW computations are based on a well converged DFT-LDA simulation. We take $r_s = 3.5$, and a slab thickness $D = 30 a_B$. The vacuum thickness has been varied from $20 a_B$ to $50 a_B$ in steps of $10 a_B$, as in these computations we are mainly interested in the convergence of the GW corrections with respect to the vacuum thickness. Moreover, to reduce the complexity of the computational procedure, the number of \mathbf{k} -points was reduced to a grid of $37 \times 37 \times 1$ with suitable shift to compute the corrections at the Γ point and at the Brillouin zone boundary. For the same reason we reduced the cut-off energy to 1 Ha after checking that this is not altering the results substantially. These choices permit to largely reduce the computational requirement at the cost of accepting DFT-LDA results not so well converged as the ones used in the previous chapters (see sec. 3.3).

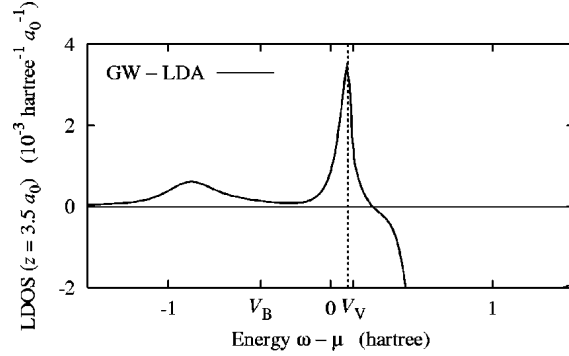


Figure 6.3: Difference in the GW minus DFT LDOS for a semi-infinite jellium with $r_s = 2.07$ at $3.5a_B$ from the surface (taken from ref. [13]). The peak indicated by V_v at $\frac{1}{32}$ Ha represents a surface resonant state.

For the calculation of the screening we use a cut-off for the plane waves slightly higher, in order to correctly read the Kohn-Sham eigenfunctions, in particular in correspondence of the boundary of the Brillouin zone. For the dielectric matrix and the self energy we applied a cut-off of 3 Ha. Finally, to fix the imaginary frequency where to compute the value of the dielectric matrix to fit the PPA eq. (6.7) we take the bulk plasma frequency $\omega_p = \sqrt{4\pi\rho} = 0.2645$ Ha for $r_s = 3.5$.

For each of the vacuum thickness we compute the correction for the eigenvalues in the Brillouin zone along the path illustrated in fig. 6.1. Since we can only compute the corrections for the \mathbf{k} -points in the DFT-LDA grid, for each thickness of vacuum we performed three computations with grids with three different shifts that are: $(0\ 0\ 0)$ for computing the correction at Γ point and most of points along the direction starting from it; $(0\ 0.5\ 0)$ for

the point J and part of the points along the boundary of the Brillouin zone and (0.5 0.5 0) for the K point and other points next to it.

The resulting band corrections are presented in the following section.

6.4.2 GW dispersion

In this section we present the resulting dispersion curves with the GW corrections performed as described in the previous sections: we refer to the values computed for 30 a_B vacuum thickness, as the results for the other thicknesses are qualitatively similar (see fig. 6.4, 6.5). From a comparison of the dispersion relations within the DFT-LDA and GW approximations we see a shift which raises all Kohn-Sham energies (i.e. the corrections are all positive)(see fig. 6.6). The general behaviour is similar: in the DFT-LDA the quasiparticles present a parabolic dispersion (see sec. 6.2), which is only slightly modified by the GW corrections. The most important differences in the dispersion curves is that the GW corrections show a step when the curves intersect the Fermi energy.

For a better understanding of these results we analyze the components of the correction, eq. (6.4), plotting one by one the correlation contribution to the self-energy, the exchange one and its derivative with respect to frequency (see fig. 6.7-6.9) in some points near Γ . We do not plot the mean of the DFT-LDA exchange and correlation potential since it is constant for each band. To demonstrate this we start from the expression of this term:

$$\langle \phi_i | V_{XC} | \phi_i \rangle = \langle \phi_i | \epsilon_{XC}[n(\mathbf{x})] + n(\mathbf{x}) \frac{d\epsilon_{XC}(\varrho)}{d\varrho} \Big|_{\varrho=n(\mathbf{x})} | \phi_i \rangle . \quad (6.11)$$

Because the eigenfunctions, in this case, are the product of a planar and perpendicular contribution, eq. (2.25), it is possible to perform the integral in the planar variables. Using the fact that the square moduli of the eigenfunctions, and therefore the total density, are constant in those directions, the expectation value is:

$$\langle \phi_i | V_{XC} | \phi_i \rangle = \int dz |\phi_i(z)|^2 \left[\epsilon_{XC}[n(z)] + n(\mathbf{x}) \frac{d\epsilon_{XC}(\varrho)}{d\varrho} \Big|_{\varrho=n(z)} \right], \quad (6.12)$$

where L is the lattice parameter in the planar directions. From this equation we deduce that this expectation value depends only on the eigenfunction in the z direction, so this contribution is indeed constant for the dispersion in the two other directions.

Note that both the exchange contribution to the self energy and its derivative are negative as expected. The correlation one takes both the signs. The

resulting corrections are positive because of the presence of the mean value of the DFT-LDA exchange and correlation potential. We can observe that all the curves are almost regular with the exception of the ones crossing ϵ_F ; in this case we find in the correlation self-energy and, principally, in the exchange one a rapid change of trend, which is the origin of the one in the dispersion relations.

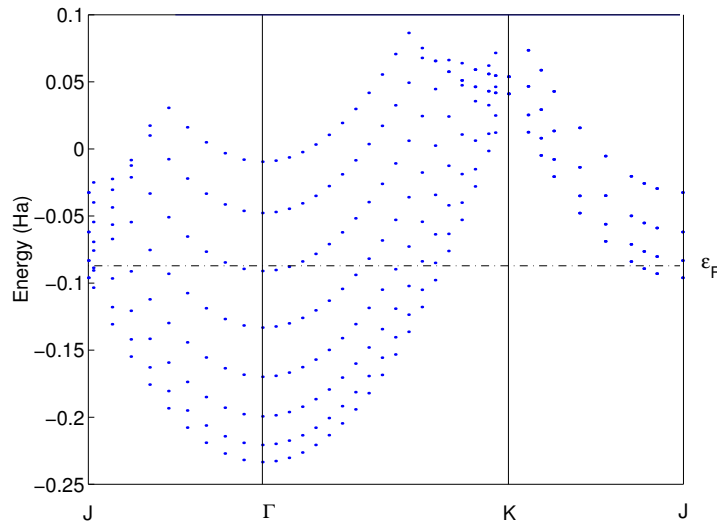


Figure 6.4: Kohn-Sham dispersion relation. The quasiparticle excitations is computed for a slab of $D = 30 a_B$ with $30 a_B$ of vacuum, $r_s = 3.5$ and lattice parameter in the surfaces plane of $5.99 a_B$.

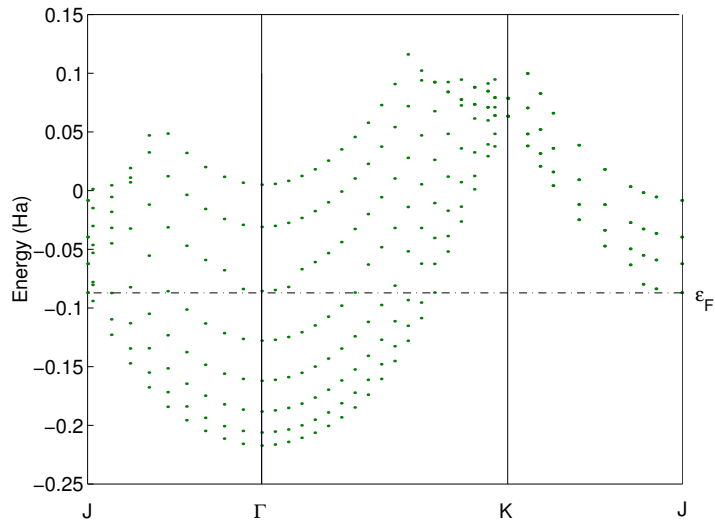


Figure 6.5: Dispersion relation with the GW corrections. Same physical conditions as fig. 6.4. The Fermi level is the Kohn-Sham one since it has not been recomputed, but the actual Fermi level is seen to raise with the bands.

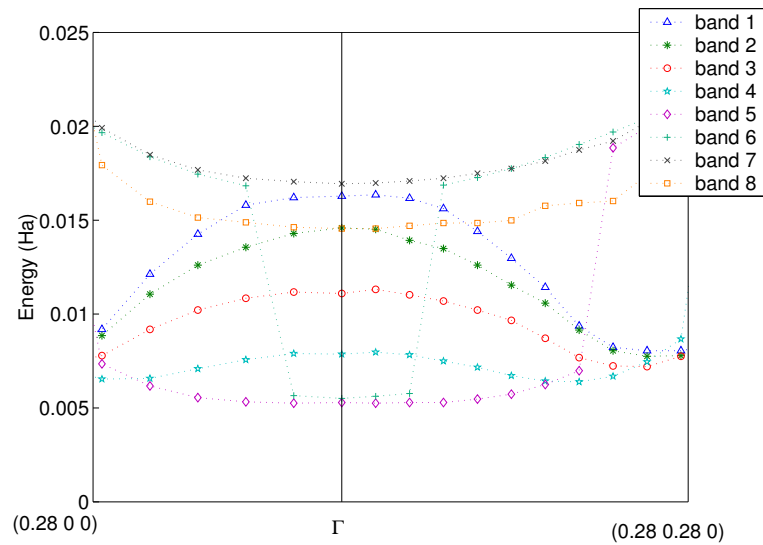


Figure 6.6: GW corrections to the Kohn-Sham eigenvalues in a neighboring of Γ . Same physical conditions as fig. 6.4.

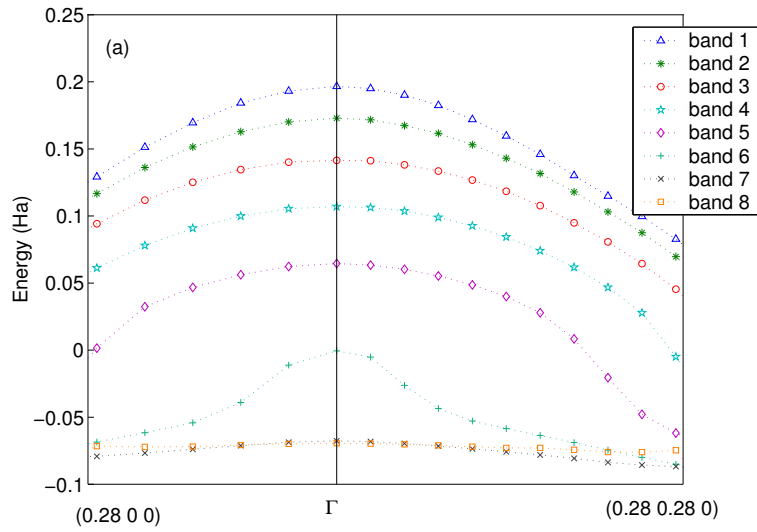


Figure 6.7: Components of the GW correction as in eq. (6.4). Expectation values of the correlation part of the self-energy. The bands are numerated from the deeper one up (see fig. 6.4 and 6.5).

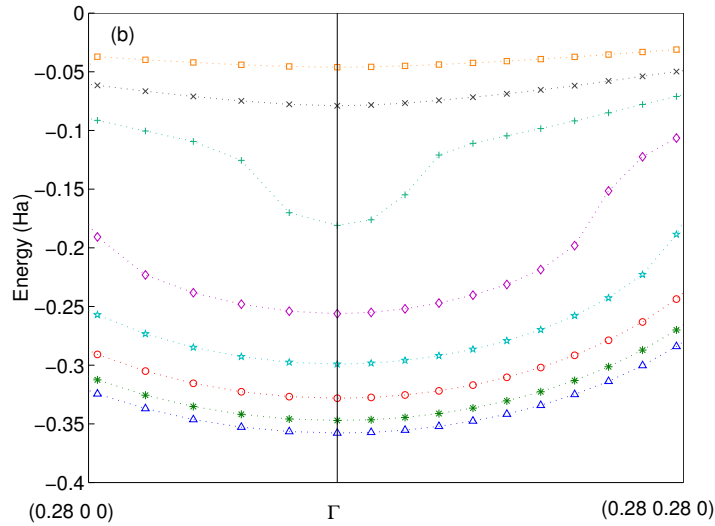


Figure 6.8: Components of the GW correction as in eq. (6.4). Expectation values of the exchange contribution of the self-energy. The legend is the same as fig 6.7.

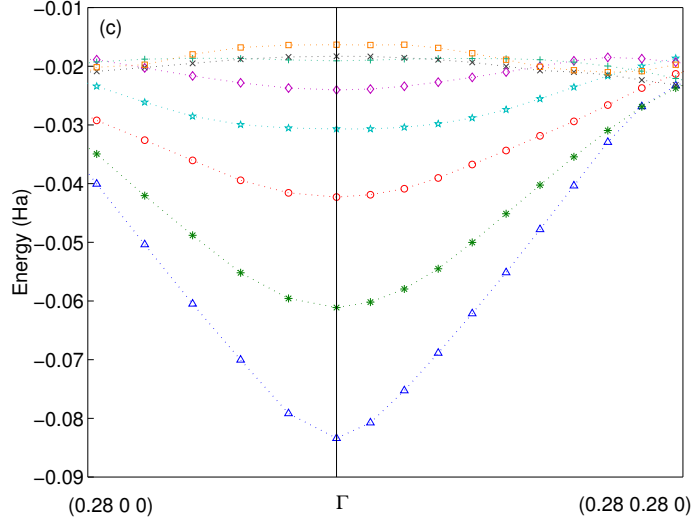


Figure 6.9: Components of the GW correction as in eq. (6.4). Expectation values of the self-energy derivative with respect to the frequency. The legend is the same as fig 6.7.

6.4.3 Convergence with the vacuum thickness

As the polarizability is an average cell property, in the repeated slab geometry it can be strongly influenced by the vacuum thickness. We check here this effect. In fig. 6.10 we compare the value of the computed correction (GW quasiparticles minus DFT-LDA eigenvalues) for the sixth band that is only partially filled (see fig. 6.5). The same considerations remain valid for the other bands. From the figure the already mentioned step emerges indifferently from the vacuum thickness.

The results show the slow convergence with the vacuum thickness. Indeed we can give a qualitative interpretation of their trend. With the increment of the vacuum thickness the mean value of the density in the unitary cell decrease even if the slab density remains the same. This corresponds to a decrement of average density with a correspondent decrease of the average dielectric constant (see the following table), towards its vacuum value $\epsilon_0 = 1$.

thickness of vacuum (a_B)	$\langle r_s \rangle$	ϵ
20	4.1497	1.0416
30	4.4097	1.0189
40	4.6422	1.0104
50	4.8535	1.0064

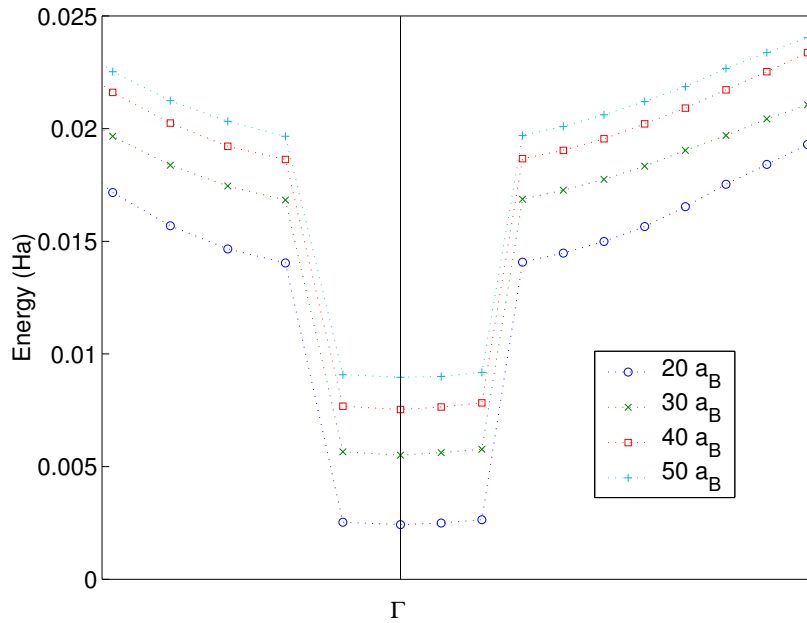


Figure 6.10: Convergence of the GW corrections against the vacuum thickness, $r_s = 3.5$ and slab thickness $30 a_B$. The figure represents the sixth band, that is partially filled (the step in the curves are between the occupied \mathbf{k} -points and the unoccupied ones).

Since we can write that $\Sigma = \frac{i}{\epsilon} G_{DFT} v$, we can say, in a first approximation, that its expectations values will be greater for higher vacuum thicknesses since the effective average dielectric constant is smaller.

Appendix A

Coulomb terms in the slab geometry

In this appendix we report the computation of the Coulombic contribution to the total energy for the special case of planar translations where some integrations can be done analytically. We refer to a slab in the $x - y$ plane, so that $n(\mathbf{x}) = n(x, y, z) = n(z)$ posed between 0 and D so that the density of particles $n(z)$ is expected to be symmetric with respect to the middle of the slab $\frac{D}{2}$.

The starting point is the usual expression:

$$E_{Coul} = \frac{1}{2} \int d^3x d^3x' \frac{n(z)n(z')}{|\mathbf{x} - \mathbf{x}'|} + \frac{1}{2} \rho^2 \int d^3x d^3x' \frac{1}{|\mathbf{x} - \mathbf{x}'|} - \rho \int d^3x d^3x' \frac{n(z')}{|\mathbf{x} - \mathbf{x}'|} \quad (\text{A.1})$$

The individual integrals present a divergence due to the slow decay of the interaction at great distance. In order to correct this inconvenience we recur to the usual method used for this kind of integrals [12]: the mere Coulombian interaction is changed to a Yukawa one by introducing a factor $e^{-\mu|\mathbf{x}-\mathbf{x}'|}$ in order to make the integrals become convergent. At the end of computation we shall take the limit $\mu \rightarrow 0$ to restore the correct Coulomb potential. In this way the functional becomes:

$$E_{Coul}[n(z)] = \frac{1}{2} \int d^3x d^3x' \frac{n(z)n(z')e^{-\mu|\mathbf{x}-\mathbf{x}'|}}{|\mathbf{x} - \mathbf{x}'|} + \frac{1}{2} \rho^2 \int d^3x d^3x' \frac{e^{-\mu|\mathbf{x}-\mathbf{x}'|}}{|\mathbf{x} - \mathbf{x}'|} + \\ - \rho \int d^3x d^3x' \frac{n(z')e^{-\mu|\mathbf{x}-\mathbf{x}'|}}{|\mathbf{x} - \mathbf{x}'|} \quad (\text{A.2})$$

The next step is the computation of the integrals in the directions perpendicular to the surfaces. The first integral evaluated is the interaction of

the background with itself, i.e.

$$E_{\rho\rho} = \frac{1}{2}\rho^2 \int d^3x d^3x' \frac{e^{-\mu|\mathbf{x}-\mathbf{x}'|}}{|\mathbf{x}-\mathbf{x}'|}. \quad (\text{A.3})$$

With a change of variable $a = x - x'$, $b = y - y'$, $c = x$, $d = y$ we obtain:

$$E_{\rho\rho} = \frac{1}{2}\rho^2 \int_0^D dz \int_0^D dz' \int_{-\frac{L}{2}}^{\frac{L}{2}} dc \int_{-\frac{L}{2}}^{\frac{L}{2}} dd \int da db \frac{e^{-\mu\sqrt{a^2+b^2+(z-z')^2}}}{\sqrt{a^2+b^2+(z-z')^2}} \quad (\text{A.4})$$

where the integrations on the variable z and z' are limited between the extremes of the slab and interactions between different periodic replicas are neglected. With a new change of variable to polar coordinates for a and b , the integration on the angular variable becomes trivial, like the ones in c and d . Performing this integrations one obtains:

$$E_{\rho\rho} = \frac{1}{2}L^2\rho^2 \int_0^D dz \int_0^D dz' \int_0^\infty dr 2\pi r \frac{e^{-\mu\sqrt{r^2+(z-z')^2}}}{\sqrt{r^2+(z-z')^2}} \quad (\text{A.5})$$

At this point it is possible to make another change of variable ($h = r^2$) to obtain an integral whose primitive is analytically known, i. e.:

$$\int \frac{e^{-\mu\sqrt{h+A}}}{\sqrt{h+A}} = -\frac{2}{\mu}e^{-\mu\sqrt{h+A}} \quad (\text{A.6})$$

Thanks to this $E_{\rho\rho}$ becomes:

$$E_{\rho\rho} = \frac{\pi}{\mu}L^2\rho^2 \int_0^D dz \int_0^D dz' e^{-\mu|(z-z')|} \quad (\text{A.7})$$

Proceeding for analogy for the remaining terms one deduces that:

$$E_{Ha} = \frac{1}{2} \int d^3x d^3x' \frac{n(z)n(z')}{|\mathbf{x}-\mathbf{x}'|} = \frac{\pi}{\mu}L^2 \int_{-\infty}^\infty dz \int_{-\infty}^\infty dz' n(z)n(z')e^{-\mu|(z-z')|} \quad (\text{A.8})$$

$$E_{\rho e^-} = -\rho \int d^3x d^3x' \frac{n(z')}{|\mathbf{x}-\mathbf{x}'|} = -\frac{2\pi}{\mu}L^2\rho \int_0^D dz \int_{-\infty}^\infty dz' n(z')e^{-\mu|(z-z')|} \quad (\text{A.9})$$

In this case the integrations are from $-\infty$ to ∞ because of the spill-out of charge, but again the interactions between repeated slabs is neglected. In the end the functional obtained is:

$$E_{Coul} = \frac{\pi}{\mu}L^2 \int_{-\infty}^\infty dz \int_{-\infty}^\infty dz' n(z)n(z')e^{-\mu|z-z'|} + \frac{\pi}{\mu}L^2\rho^2 \int_0^D dz \int_0^D dz' e^{-\mu|z-z'|} +$$

$$-\frac{2\pi}{\mu}L^2\rho \int_0^D dz \int_{-\infty}^{\infty} dz' n(z') e^{-\mu|z-z'|}. \quad (\text{A.10})$$

Because in this computations we are interested in the energy per unit surface, this functional is divided by L^2 and the problem of the convergence in the planar dimensions is solved. The limit for $\mu \rightarrow 0$ is obtained by Taylor expansion of the exponential at first order (we stop at this order because, as it will be clear, higher orders produce terms proportional to positive powers of μ that vanish in the limit). The Coulombic term of the total energy becomes:

$$\begin{aligned} \frac{E_{Coul}}{L^2} &= \frac{\pi}{\mu} \int_{-\infty}^{\infty} dz \int_{-\infty}^{\infty} dz' n(z)n(z')(1 - \mu|z - z'|) + \frac{\pi}{\mu}\rho^2 \int_0^D dz \int_0^D dz'. \\ &\cdot (1 - \mu|z - z'|) - \frac{2\pi}{\mu}\rho \int_0^D dz \int_{-\infty}^{\infty} dz' n(z')(1 - \mu|z - z'|). \end{aligned} \quad (\text{A.11})$$

It is now possible to perform the integrations of the terms of order 0. All terms of order μ^0 cancel exactly thanks to charge neutrality. The contribute of the Coulombic terms reduce itself to the effects due to the first order μ terms, so that the functional results:

$$\begin{aligned} \frac{E_{Coul}}{L^2} &= -\pi \int_{-\infty}^{\infty} dz \int_{-\infty}^{\infty} dz' n(z)n(z')|z - z'| - \pi\rho^2 \int_0^D dz \int_0^D dz' |z - z'| \\ &+ 2\pi\rho \int_0^D dz \int_{-\infty}^{\infty} dz' n(z')|z - z'| \end{aligned} \quad (\text{A.12})$$

At this point it is possible to perform the integrals involving the background. About the background-background interaction since the integrand and the domain are symmetric with respect to $x = y$ the integral to perform reduces to:

$$\frac{E_{\rho\rho}}{L^2} = -2\pi\rho^2 \int_0^D dz \int_0^z dz' (z - z') = -\pi\rho^2 \frac{D^3}{3} \quad (\text{A.13})$$

In a similar way it is possible to perform one integration for the term of interaction between the electrons and the background. Because of the presence of the modulo we separate the integration in four addends:

$$\begin{aligned} E_{\rho e^-} &= 2\pi\rho \left[\int_{-\infty}^0 dz' n(z') \int_0^D (z - z') + \int_0^D dz' n(z') \int_{z'}^D (z - z') + \right. \\ &\left. + \int_0^D dz' n(z') \int_0^{z'} (z' - z) + \int_D^{\infty} dz' n(z') \int_0^D (z' - z) \right]. \end{aligned} \quad (\text{A.14})$$

Now it is possible to observe that the first and the last term thanks to the symmetry of $n(z')$ are equal to the second and third ones. So the symmetrized form of this term is

$$E_{\rho e^-} = 2\pi\rho \left[\int_D^\infty dz' n(z')(2z'D - D^2) + \int_0^D dz' n(z') \frac{z'^2}{2} \right]. \quad (\text{A.15})$$

No simplification is possible for the $n(z)n(z')$ term. In total the functional of Coulomb interactions for a jellium slab results

$$\begin{aligned} E_{Coul} = & -\pi \int_{-\infty}^\infty dz \int_{-\infty}^\infty dz' n(z)n(z')|z - z'| - \pi\rho^2 \frac{D^3}{3} + \\ & + 2\pi\rho \left[\int_D^\infty dz' n(z')(2z'D - D^2) + \int_0^D dz' n(z') \frac{z'^2}{2} \right]. \quad (\text{A.16}) \end{aligned}$$

Conclusions

In this work we investigate the functionality and the limitations of the jellium model for the simulation of a metal surface, for both the ground and excited states. We perform numerical calculations by using and modifying the plane-wave ABINIT computer code (available under the GNU license). In principle, as long as translational invariance in the in-plane directions is retained, all \mathbf{k} -point integrations in these directions could be performed analytically, leaving an effectively one-dimensional problem to be solved. The use of a tridimensional code to perform the simulations in this thesis is justified by the fact that, in a following step, one would use this code to study the interaction of a jellium surface with an adsorbate, where the translational invariance would be broken.

The code has been tested with the successful comparison of numerical results with analytical ones, and with previous calculations. The results obtained during this work reveal which numerical effects of the standard approximations are the most relevant: these are mainly due to the discretization of the \mathbf{k} -point mesh, and the consequent introduction of the smearing of the occupancy numbers.

Employing a slab geometry in particular to compare the surface energy with the literature values, we observe the quantum size effects induced by the nanosized thickness of the slab, with oscillations in the surface tension (energy per unit area). These effects have been explained in term of oscillations in the surface dipole, induced by the discretization of the eigenfunction in the direction orthogonal to the surfaces. These oscillations are the origin of a modulated charge spill-out as the slab thickness increases and more and more wavefunction are filled. We have shown that the observed oscillations can be explained by means of a simple surface dipole model. In the final part of this work we performed a test on the GW correction to the Kohn-Sham eigenvalues, in particular concerning the convergence with respect to the vacuum thickness. results from these tests show a slow convergence. The GW calculations also show a step in the dispersion curves when the quasiparticle excitation crosses the Fermi surface.

Bibliography

- [1] <http://www.abinit.org>
- [2] P. H. Acioli, D. M. Ceperley, Phys. Rev. B **54**, 17199 (1996)
- [3] N. W. Ashcroft, N. D. Mermin, *Solid State Physics*, Harcourt, Orlando 1976
- [4] W. G. Aulbur, L. Jönsson, L. W. Wilkins, *Quasiparticles calculations in solids*, published in H. Ehrenreich, F. Spaepen, *Solid State Physics*, Academic press, San Diego 2000
- [5] J. Bardeen, Phys. Rev. **49**, 653 (1936)
- [6] J. C. Boettger, Phys. Rev. B **53**, 13133 (1996)
- [7] D. M. Ceperley, B. J. Adler, Phys. Rev. Lett. **45**,566 (1980)
- [8] M. C. Desjonquères, D. Spanjaard, *Concepts in Surface Physics*, Springer-Verlag, Berlin 1993
- [9] R. M. Dreizler, E. K. U. Gross, *Density Functional Theory*, Springer-Verlag, Berlin 1990
- [10] T. Endo, M. Horiuchi, Y. Takada, H. Yasuhara, Phys. Rev. B **59**, 7367 (1999)
- [11] R. A. Evarestov, V. P. Smirnov, Phys. Stat. Sol. (b) **119**, 9 (1983)
- [12] A. L. Fetter, J. D. Waletcka, *Quantum Theory of Many Particle Physics*, McGraw-Hill, New York 1971
- [13] G. Fratesi, G. P. Brivio, P. Rinke, R. W. Godby, Phys. Rev. B **68**, 195404 (2003)
- [14] R. W. Godby, M. Schlüter, L. J. Sham, Phys. Rev. B **37**, 10159 (1988)

- [15] S. Goedecker, M. Teter, J. Hutter, Phys. Rev. B **54**, 1703 (1996)
- [16] X. Gonze, J.-M. Beuken, R. Caracas, F. Detraux, M. Fuchs, G.-M. Rignanese, L. Sindic, M. Verstraete, G. Zerah, F. Jollet, M. Torrent, A. Roy, M. Mikami, Ph. Ghosez, J.-Y. Raty, D. C. Allan, Comput. Mat Sci. **25**, 478 (2002)
- [17] L. Hedin, Phys. Rev. **139**, A796 (1965)
- [18] L. Hedin, S. Lunnqvist, Solid State Phys. **23**, 1 (1969)
- [19] P. Hohenberg, W. Kohn, Phys. Rev. **136**, B864 (1964)
- [20] B. Holm, U. von Barth, Phys. Rev. B **57**, 2108 (1997)
- [21] M. S. Hybertsen, S. G. Louise, Phys. Rev. B **34**, 5390 (1986)
- [22] W. Kohn, A. E. Mattsson, Phys. Rev. Lett. **81**, 3487 (1998)
- [23] W. Kohn, L. J. Sham, Phys. Rev. **140**, A1133 (1965)
- [24] N. D. Lang, W. Kohn, Phys. Rev. B **1**, 4555 (1970)
- [25] A. Marini, G. Onida, R. Del Sole, Phys. Rev. Lett. **88**, 016403 (2002)
- [26] N. Marzari, PhD dissertation, U. of Cambridge (1996) (<http://nmm.mit.edu/phd>)
- [27] A. E. Mattsson, W. Kohn, J. Chem. Phys. **115**, 3441 (2001)
- [28] E. E. Mola, J. L. Vicente, J. Chem. Phys. **84**, 2876 (1986)
- [29] H. J. Monkhorst, J. D. Pack, Phys. Rev. B **13**, 5188 (1976)
- [30] M. C. Payne, M. P. Teter, D. C. Allan, T. A. Arias, J. D. Joannopoulos, Rev. Mod. Phys. **64**, 1045 (1992)
- [31] J. P. Perdew, A. Zunger, Phys. Rev B **23**, 5048 (1981)
- [32] V. Sahni, C. Q. Ma, Phys. Rev. B **22**, 5978 (1980)
- [33] A. Schindlmayr, T. J. Pdlehn, R. W. Godby, Phys. Rev. B **58**, 12684 (1998)
- [34] W. Schmickler, D. Henderson, Phys. Rev. B **30**, 3081 (1984)
- [35] F. K. Shulte, Surf. Sci. **55**, 427 (1976)

- [36] I. Sarria, C. Henriques, C. Fiolhais, J. M. Pitarke, Phys. Rev. B **62**, 1699 (2000)
- [37] C. A. Utreras-Diaz, Phys. Rev. B **36**, 1785 (1987)
- [38] J. Vannimetus, H. F. Budd, Phys. Rev. B **15**, 5302 (1977)
- [39] K. F. Wojciechowski, Phys. Rev. B **60**, 9202 (1999)
- [40] Z. Y. Zang, D. C. Langreth, J. P. Perdew, Phys. Rev. B **41**, 5674 (1990)

Ringraziamenti

Desidererei innanzitutto ringraziare il mio relatore Prof. Giovanni Onida per l'assiduità con cui mi ha seguito e per aver condiviso con me la curiosità verso gli argomenti oggetto di questo lavoro. Lo stesso dicasi per i miei correlatori Dott. Nicola Manini e Dott. Luca Guido Molinari.

Ringrazio anche tutte le altre persone che lavorano al progetto di ricerca al quale spero di aver contribuito con questa tesi. In primis ringrazio il Dott. Sebastiano Caravati le cui modifiche al codice di ABINIT hanno permesso lo svolgimento di questo lavoro. Vorrei anche citare il Prof. Gian Paolo Brivio e il Dott. Mario Italo Trioni. Ringrazio tutti costoro per le utili riunioni, nelle quali è stato possibile confrontare i nostri risultati e avere un interessante scambio di idee.

La mia gratitudine va anche a coloro che lavorano per il gruppo di ricerca nel quale mi sono inserito, con i quali ho avuto il piacere di collaborare. In particolare ringrazio il Dott. Andrea Bordoni, il Dott. Incze Andrei e la Dott.ssa Katalin Gaál-Nagy per avermi aiutato a risolvere una serie di problemi di svariata natura nei quali mi sono imbattuto.

Voglio ringraziare anche il mio amico Marco Monticelli per avermi dato una serie di utilissimi consigli tecnici a seguito delle non infrequenti sorprese riservatemi dai computers.

Passo quindi a ringraziare tutti gli amici che hanno trascorso con me questi anni di università. In particolare tre persone con le quali ho avuto modo di condividere più che con altri le preoccupazioni e le gioie della vita universitaria (oltre che gli interminabili pomeriggi in laboratorio): Chiara, Jacopo e Maria. È giunto il momento di ringraziare anche i miei amici teorici: Pietro, Andrea, Simone, Claudia, Fabio, Michele, Federica e Gea. Sono stato veramente contento di aver trascorso con voi delle piacevoli pause pranzo, protrattesi ben oltre il dovuto, giocando a carte in aula A. Infine ringrazio anche (in ordine casuale) Emanuele, Elisabetta, Giacomo (entrambi), Francesca, Alessio e tutti gli altri che non ho citato.

Per ultimo vorrei ringraziare anche i miei nonni Carla e Pietro che mi hanno sempre fatto trovare un pasto caldo di ritorno dall'università.